A Microwave Powered

DNA Extraction Module

Solstice Wilson-Garner

School of Pharmacy

Cardiff University

This dissertation is submitted for the degree of

Doctor of Philosophy

December 2023

Declaration

I hereby declare that except where specific reference is made to the work of others, the contents of this dissertation are original and have not been submitted in whole or in part for consideration for any other degree or qualification in this, or any other university. This dissertation is my own work and contains nothing which is the outcome of work done in collaboration with others, except as specified in the text and Acknowledgements. This dissertation contains fewer than 80,000 words including appendices, bibliography, footnotes, tables and equations and has fewer than 150 figures.

Solstice Wilson-Garner

December 2023

Summary

Mycobacterium tuberculosis is a multidrug resistant pathogen commonly isolated from patients with TB. Currently, there is no rapid diagnostic tool to detect the presence of *M.tuberculosis*. The rapid diagnosis and prompt subsequent treatment remains the best curative approach to reduce disease burden and interrupt transmission. A major concern in developing a rapid diagnostic assay is DNA extraction. Mycobacterial cells are very difficult to lyse; the existing methods are time consuming, resulting in long process time to detect the pathogen.

The aim of this project was to improve upon an existing method of DNA extraction and verification by creating a 10ml cartridge capable of promoting microwave interaction with entire TB patient samples (as opposed to 250μl samples used in the past) in a single excitation stage, thereby vastly improving the sensitivity of the assay reducing the risk of false negative results.

The microwave applicator parameters were optimised to obtain the maximum possible DNA release from the target pathogen. This DNA was then collected by means of DNA-specific probes attached to magnetic nanoparticles, allowing the target DNA to be separated and concentrated before it was detected with a lower limit of $10^4 CFU/ml$.

Finally, the project explored the possibility of integration of each stage of the diagnostic process (microwave application, magnetic nanoparticle collection, diagnosis) into a single portable device.

In conclusion, a 10ml cartridge has been designed and microwave application parameters have been optimised to yield a rapid diagnostic assay. Initial exploration is underway to transfer this assay from the laboratory to real-world application.

Publications and Communications

Published Work:

S. Wilson-Garner, L. Baillie, A.Porch, "Increasing Sample Volume for Microwave-Assisted Rapid DNA Release", 2022 Asia-Pacific Microwave Conference (APMC2022)

Submitted for Publication:

S. Wilson-Garner,S. Abdullah A Alzeer, L. Baillie, A.Porch, "High Volume Biological Sample Processing using Microwaves", Journal of Applied Physics, 2023

Conferences/Presentations:

Oral Presentation: "Increasing Sample Volume for Microwave-Assisted Rapid DNA Release", 2022 Asia-Pacific Microwave Conference (APMC2022), 2^{nd} December 2022, Yokohama, Japan

Oral Presentation: "Microwaves and Nanoparticles for Real-Time Detection of Human Pathogens", Ukrainian Conference with International Participation Chemistry, Physics, and Technology of Surface, National Academy of Sciences of Ukraine Chuiko Institute of Surface Chemistry, 20^{th} October 2022, Kyiv, Ukraine, (Remote)

Table of contents

List of figures

List of tables

Chapter 1

Introduction

The aim of this project is to build on a body of work undertaken to improve the idea of rapid pathogen diagnosis via confirmation of the presence of the pathogen specific DNA using microwave power application as the method of DNA release. The work aims to increase the volume of sample that can be processed to real world volumes.

1.1 Microwave Extraction

Since the 18th century scientists have been intrigued by the interaction of electromagnetic fields (EMFs) and various life processes [1]. In recent years, microwaves have performed well in the treatment of tumors and so have become a relatively novel and popular tumor treatment method [2] [3]. However, their ability to eliminate bacterial infections has not received much attention [4]. Various studies have shown that both thermal and non-thermal effects of microwaves are able to inactivate various species of bacteria. A great number of studies of the thermal versus non-thermal bio-effects of low-power MW were performed with various cellular functions, including gene expression [5] and mutation [6], enzyme activity [7], unfolding of proteins [8], biochemical cell systems [9], cell wall [10], cell morphology [11], and cell proliferation [12][13][14][15].

The overall principle of DNA extraction using microwaves has been extensively explored (whereas the direct mechanism has not) and has been used for a variety of applications such as forensic analysis [16] and the preparation of genomic DNA for PCR [17][18]. There are many different methods of applying a microwave field to a sample, the efficiency of which is affected by a number of factors including sample size, geometry (very important when dealing with electromagnetic wave interaction) and the concentration of target DNA carrier, to name a few. The following section follows the journey of research, leading to the inception of this project.

1.1.1 MAMEF

In 2007, Aslan and colleagues used a method of rapid DNA detection denoted Microwave Accelerated Metal Enhanced Fluorescence (MAMEF) to detect anthrax DNA concentration of 1ng/µl within 30 seconds [19]. Standard MEF measures the enhanced fluorescent interaction between metallic surfaces and fluorophores. This process was accelerated by using microwaves to increase the rate at which the DNA hybridizes [19]. This process was further developed to focus the microwaves into the sample using triangular aluminium electrodes, in a "bow tie" configuration (shown in fig. 1.1 [20]) .

The triangles focus the electric field into a small space between them in which the sample is placed. In 2014, Joshi and colleagues demonstrated that this system could be used to detect as low as 10 *Clostridium difficile* spores in 500µl of untreated human faeces within 40 seconds [21]. Using this technique, the DNA was extracted from the spores within 20 seconds and detected, using an MAMEF stage, in a further 30 seconds. The sensitivity of the approach is limited, however, by the sample size. The space between the triangles is only large enough to hold a 50µl sample. The triangles are also ineffective at focusing the microwave field. The 700W microwave oven used in these studies should be able to boil

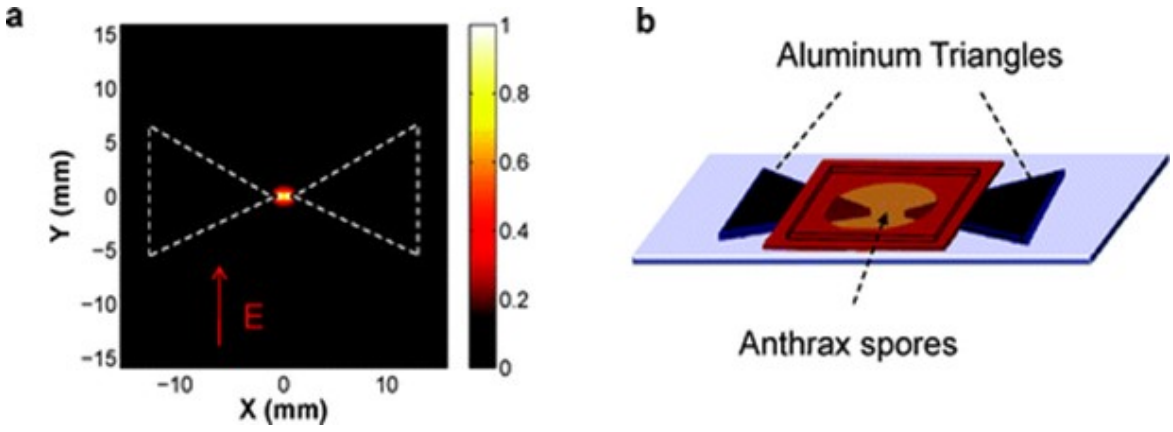

Fig. 1.1 The bow-tie setup used for MAMEF. The aluminium triangles are used to focus the microwave electric field between the two tips. The electric field outside the area becomes minimal. The setup with spore sample on top of the triangles. The overall heating of the sample was reported to be from 23° C to 28°C [21]. Figure taken from: *"Extraction and sensitive detection of toxins a and b from the human pathogen clostridium difficile in 40 seconds using microwave-accelerated metal-enhanced fluorescence."*, Joshi L.T. et al

water in much less than a second (assuming the power transfer efficiency is 1%). If we take the standard equation for initial heating rate:

$$\frac{dT}{dt} = \frac{P}{mc} \tag{1.1}$$

substituting the values for the example:

$$\frac{dT}{dt} = \frac{7}{0.05 \times 4.2} = 33.3^{o}C/s \tag{1.2}$$

where:

- ***P*** is the power of the microwave oven multiplied by the efficiency (1% of 700W gives 7W)

- ***m*** is the mass of the sample (50µl = 0.05g)

- ***c*** is the specific heat capacity of water (4.2J/g)

- ***dT/dt*** is the rate of change of temperature.

At this rate of change (dT) the sample should boil within 3 seconds. Given that the samples were heated for up to 20 seconds with no visible boiling effect then the efficiency of energy transfer for this system must be 0.1% or lower.

To improve on this, a new system of microwave excitation was designed (shown in fig. 1.11). This utilizes a cylindrical TM_{010} cavity to transfer up to 30W of power into a 250µl sample with >99% efficiency [21].

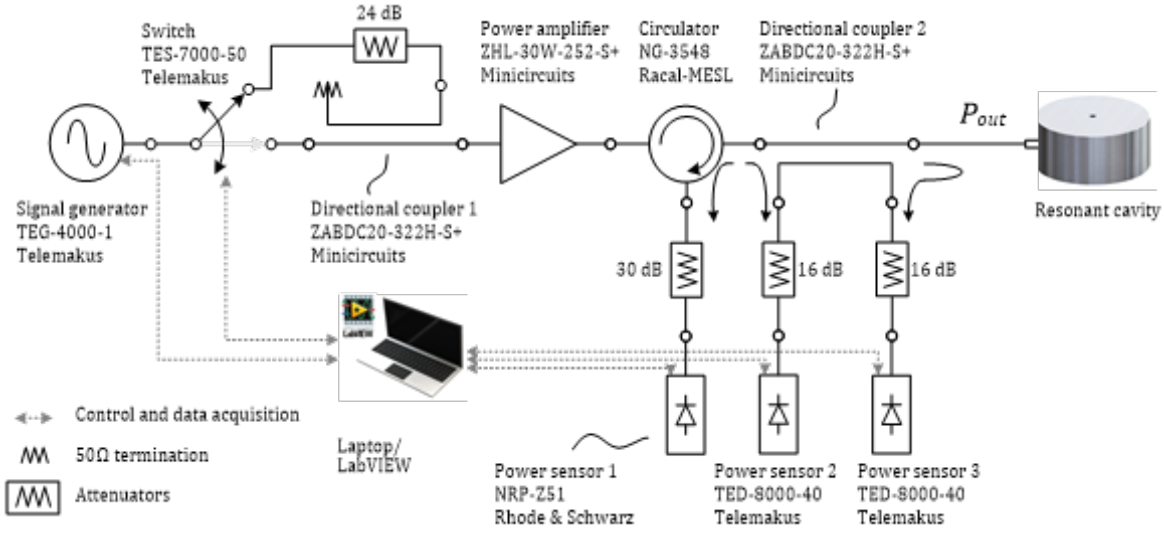

Fig. 1.2 Microwave Excitation System circuit diagram Figure taken from: *"The biological effect of 2.45GHz microwaves on the viability and permeability of bacterial and yeast cells."*, Ahortor E.K. et al [22]

Using this system, it was found that the DNA releasing effects of the microwaves were due to the electric field as opposed to the magnetic field within the cavity [22]. This was shown by exciting sample tubes containing bacterial and yeast cells in areas of quasi-exclusive electric field and quasi-exclusive magnetic field as (shown in fig 1.3).

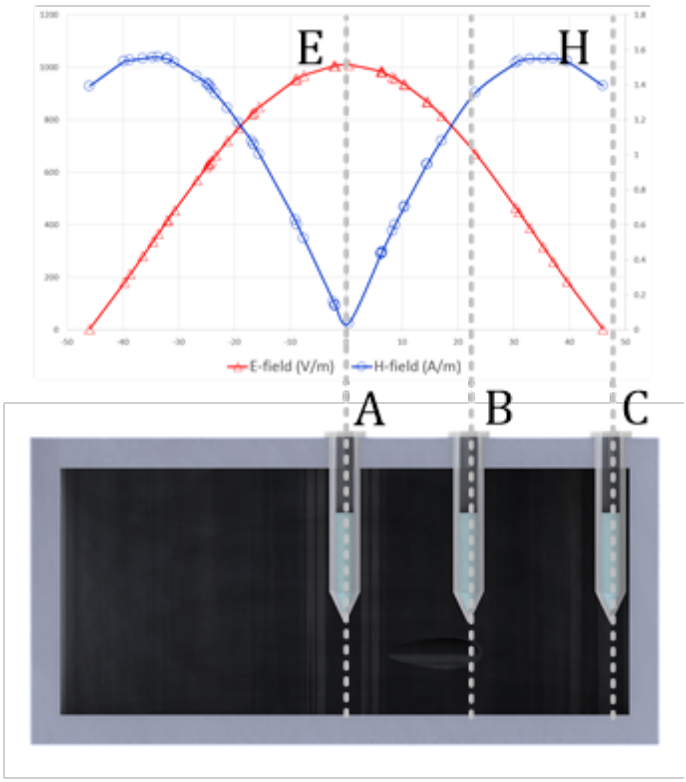

Fig. 1.3 Sample tubes positioned within the cavity to isolate the electric (sample A) and magnetic (sample C) fields. Sample B was also included to demonstrate the effect of both fields on DNA release Figure taken from: *"The Rapid Detection of Drug Resistant Mycobacteria"*, Ahortor E.K. et al [23].The magnitude of the power here can be calculated as the cross product of the E and H field.

The results of this study show that DNA was detected following E field exposure of *M. smegmatis*. In contrast, there was no increase of DNA following H field exposure suggesting that they had no effect on membrane structure. The study also looked at the transfer of dextran particles over the cell wall during exposure to both E and H fields. The study showed

that there was high transfer during E field exposure but none during H field exposure. It concluded that microwave generated E fields can temporarily disrupt membrane integrity without detrimentally impacting on cell viability, but H field have little to no affect on the membrane [22]. To enhance the recovery of DNA released as a consequence of microwave mediated disruption, the laboratory recently developed an approach which made use of DNA probe labelled magnetic nanoparticles [23]. Magnetic beads (Dynabeads) have been used to capture DNA from tissue samples containing *M. tuberculosis* embedded in paraffin wax with the presence of pathogen specific sequences being confirmed using Polymerase Chain Reaction (PCR). This project will attempt to tailor the magnetic beads by the addition of target specific DNA probes with specificity for TB specific DNA sequences, to promote greater sensitivity. The process steps are demonstrated in fig 1.4 below.

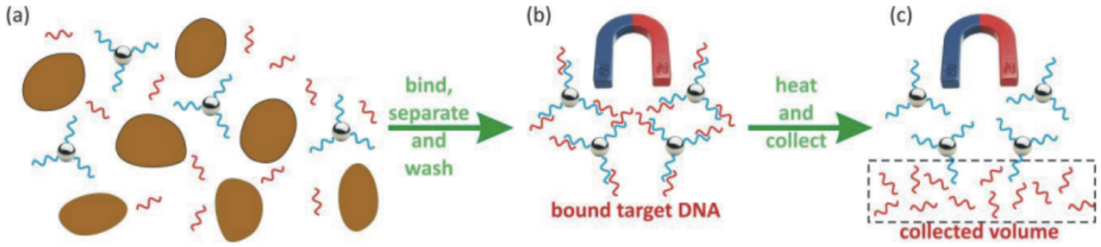

Fig. 1.4 The concepts of extraction and concentration of the target DNA (red). (a) The biological sample (containing target bacteria) is homogenized ultrasonically and irradiated by pulsed microwaves, after which the target DNA is released into solution and is captured by the functionalized magnetite particles labelled with pathogen specific DNA; (b) the bound DNA is captured by an electromagnet, is washed, and (c) is then released for the detection cartridge by heating to 60°C. (Biorender supplied by Prof Les Baillie).

1.2 Limitations of current approach

The current microwave set up can only process relatively small samples with a maximum volume of 250µl. The larger the volume of samples that can be processed, the higher the likelihood of detecting the pathogen. When it is present in small numbers it is unlikely to be distributed through the sample in a homogeneous manner (fig 1.5). Thus, the volume of sample which can be processed in a single step needs to increase greatly.

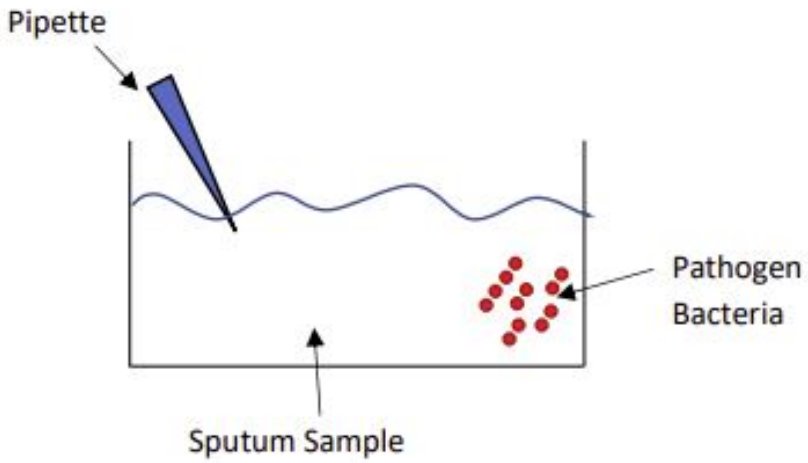

Fig. 1.5 Demonstration of the necessity to use an entire patient sample to give the most precise diagnosis result.

This requires the design a sample processing cartridge in which all of the major steps, from bacterial disruption to target DNA capture and recovery of DNA carrying magnetic nanoparticles, are undertaken in a single container which is cheap to produce and protects the operator from the risk of exposure. It is therefore also necessary to design an external system to mix and capture the DNA-coated magnetic nanoparticles within the cartridge.

1.3 Project Aims

The project has the following major aims (these are the novel aims within the work):

1. Creation of a sample processing cartridge capable of handling sample volumes of 5-10ml.
2. Optimize the cartridge geometry to promote strong/uniform microwave interaction with the sample.
3. Optimize DNA release from bacteria in the sample via microwave excitation.
4. Design a system by which the DNA can be extracted from the cartridge without contaminating the microwave cavity.

Chapter 2

Literature Review

2.1 The History of Tuberculosis

The disease we now know as Tuberculosis has existed for millennia [24]. It is known to have been present in humans at least as far back as Ancient Egyptian culture (3,000-2,400 BC) based on tubercular decay found in the spines of mummies [25]. However, it is proven to have been present in bovines much earlier, having been discovered in the remains of a bison dating from 17,000 BC [26]. Due to its widely varying symptoms, it was not shown to be a single disease until the 1820s by Schönlein, who also came up with the name 'tuberculosis' in 1839 [27]. The main form of tuberculosis in humans is caused by a bacterium called *Mycobacterium tuberculosis (M. tb)* and was first identified in 1882 by Robert Koch [28]. Its general symptoms include lack of appetite and weight loss; a high temperature; night sweats and extreme tiredness or fatigue.

tuberculosis (TB) mainly affects the lungs, a condition known as pulmonary tuberculosis. Its symptoms include increasingly severe breathlessness as well as a persistent, possibly bloody, cough. Less commonly, TB can affect other areas of the body outside the lungs, such as the small glands that form part of the immune system (the lymph nodes), the bones and joints, the digestive system, the bladder and reproductive system, and the brain and nerves [29].

There is also a form of latent infection which does not present with any symptoms but can be carried for decades and transform into active tuberculosis later (often due to the presence of immunosuppressant conditions within the patient). Around 1.7 billion people (around 1/5th of the world's population) are estimated to be infected with this latent form [30].

Human immuno-deficiency virus (HIV) plays a large part in the severity of TB and is the largest susceptibility factor worldwide. HIV weakens the immune system, thus worsening the effects of TB and creating a higher risk that the latent form will develop into the active disease. This is particularly problematic in areas where rates of HIV are high, such as in sub-Saharan Africa [31]. In 2005, Gibson and colleagues reported that in these areas people without HIV have a 5-10% chance of developing the active disease, whereas those with HIV had a 30% chance [32]. The problem is exacerbated by the fact that the main strategy for effective treatment of TB is based on early diagnosis and treatment [33], but this is not easily manageable in situations where resources are low, and hospitals are sparse.

2.2 What is *Mycobacterium tuberculosis*

Mycobacterium tuberculosis is a member of the mycobacteria genus. *Mycobacterium tuberculosis* is defined as slow-growing, rod-shaped bacteria 2-4μm in length with a width of 0.2-0.5μm [34]. They have a waxy cell wall of high lipid content, meaning they can appear as both Gram positive and Gram negative, rendering a stain test inconclusive [35]. The presence of a lipid called mycolic acid in the cell wall means that the bacterium is acid-fast under certain staining conditions; this attribute is used to support microscopic diagnosis. The contrast in cell wall composition (between mycobacteria and Gram positive/negative bacteria) is shown in fig. 2.1 ([36], [37]) & 2.2([38],[39]).

The wider group of TB bacteria is called the *Mycobacterium tuberculosis* complex (MTBC). This complex contains 5 other members: *Mycobacterium africanum*, *Mycobacterium bovis*, *Mycobacterium canettii*, *Mycobacterium pinnipedii*, *Mycobacterium leprae*

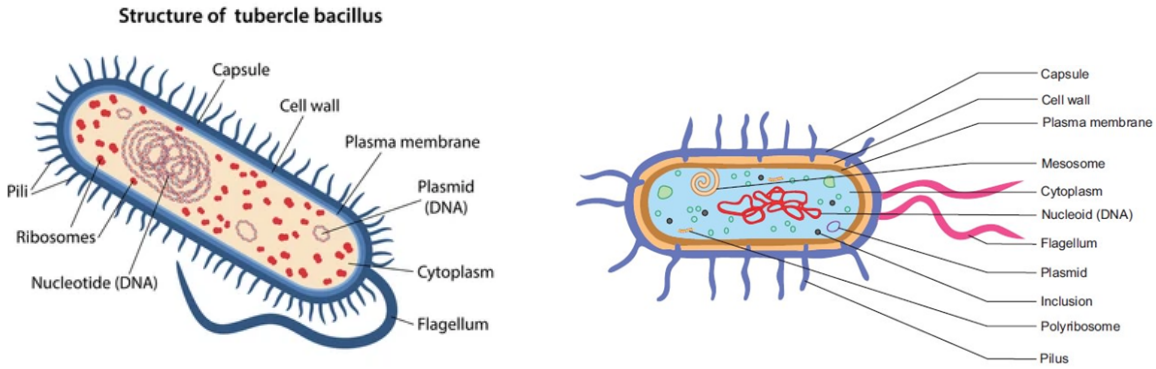

Fig. 2.1 Structure of *Mycobacterium tuberculosis* cell (left) shown alongside a non mycobacteria prokaryotic cell, *Escherichia coli* (right). The two structures are effectively identical, the main difference between them being the presence of mycolic acid in the cell wall Figure reproduced from *"Ultrastructure of a bacterial cell"*, Kart B. [37][38].

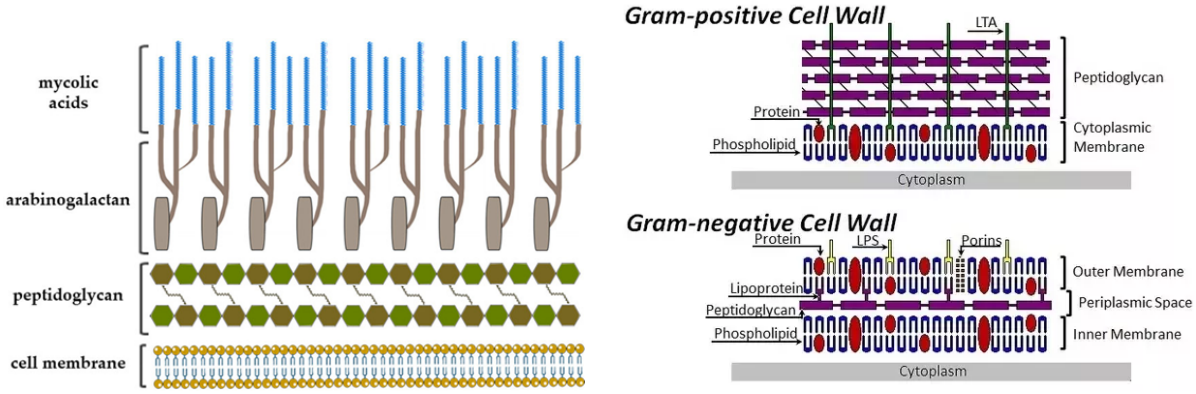

Fig. 2.2 Structure of *Mycobacterium tuberculosis* cell wall (left) compared with Gram positive and Gram negative non-mycobacteria cell walls (right) Figure taken from: *"Bacterial cell structure cell wall gram-positive bacteria gram-negative bacteria", Jawad* [39][40].

(the causative pathogen for leprosy) and *Mycobacterium microti*. The pathological effects on their respective host organisms are fairly similar; *Mycobacterium microti* affects small rodents such as voles, shrews and mice [40]; *Mycobacterium africanum* affects only humans and is limited to the West Africa, although occasional cases have been documented in other parts of the world [41]; *Mycobacterium pinnipedii* mainly affects seals [42]; *Mycobacterium*

canetti is a newly emerging strain of TB developing in Africa, its hosts and transmission modes are currently unknown [43]. There are also rapidly growing mycobacteria strains, including *Mycobacterium fortuitum, Mycobacterium chelonae, Mycobacterium smegmatis (M. smegmatis), Mycobacterium abscessus (M. abscessus), Mycobacterium mucogenicum, Mycobacterium peregrinum*.

Mycobacterium bovis (M.bovis), which causes bovine tuberculosis (b.Tb), is predominantly found in both domestic and wild animals. It is, however, possible for it to transfer from animals and humans [44][45][46]. This transmission occurs predominantly due to unpasteurised cow milk or meat which contains the bacteria [47][48]. There is significant evidence of active badger involvement in transmission of *M.bovis* to cattle [49] and human to human transmission of *M.bovis* has also been documented [50]. It remains a major health concern in the UK as well as in other developed and developing nations. In 2008 and 2009, £100 million was spent on the control of b.Tb in the UK [46]. Usually control takes the form of slaughter of entire herds if the presence of *M.bovis* is suspected. In 2018 alone, 44,656 animals were slaughtered due to b.Tb [51], causing huge financial losses for farmers.

The defining characteristic of mycobacteria is the presence of a thick, waxy, lipid-rich outer layer that contains high concentrations of mycolic acid (shown in fig 2.2) [52]. The structure of this wall and its relatively low permeability gives this family of bacteria a high degree of protection from external threats such as antibiotics and chemotherapeutic agents [53][54]. The wide variety of mycobacterial strains differ in a plethora of ways. The colony morphology varies, with some species growing as rough or smooth colonies. Colony colour ranges from white to orange or pink [55]. Most mycobacteria are aerobic organisms, although some species are microaerophilic [56]. The main physiological difference between strains is their growth rate. Most strains of mycobacteria are able to grow on blood agar [57], but some (such as *M. tuberculosis*) cannot, and require the use of enriched, egg-based media such as Löwenstein–Jensen medium [58] (consisting of malachite green, glycerol, asparagine,

potato starch, coagulated eggs, potassium dihydrogen phosphate, magnesium sulfate, sodium citrate [59], although this is occasionally altered). Growth rates, however, can differ greatly between strains with "slow" and "fast" growing species. Slow growing species such as *M. tuberculosis, M. bovis, M. leprae, M. microti, and M. pinnipedii* can take up to 3-4 weeks to form colonies [60]. Fast growing species such as *M. fortuitum, M. chelonae, M. abscessus, M. smegmatis,* and *M. mucogenicum* can form mature colonies in 7 days [61].

M. smegmatis is often employed as a model for laboratory research as it renders the acquisition of large data sets much simpler. It is also non-pathogenic (except in very rare cases [62]) and so requires only bio-safety level 2 for use [63].

2.2.1 Infection and Transmission

TB infection commences when viable *M. tb* bacilli enter the lungs. This commonly occurs through the inhalation of a respiratory droplet containing between 1 and 10 (viable) bacilli [64]. The bacilli then enter the alveoli and are usually engulfed and destroyed by alveolar macrophages, forming granulomas (tiny clusters of white blood cells and other tissue that can be found in the lungs, head, skin or other parts of the body in some people; they form as a reaction to infections, inflammation, irritants or foreign objects). However, if this mechanism fails, the bacteria will begin to reproduce and infect the lungs (the full process is described in fig 2.3 [65]). From there the infection can spread to the lymph nodes, pleura, skin, joints, central nervous system (CNS), gastrointestinal tract and abdomen (extrapulmonary TB). Miliary TB is a form of TB characterized by tiny lesions on multiple organs involving the lungs, spleen, CNS and liver [66].

The transmission of TB can be linked to a number of factors. As mentioned previously, the bacteria are spread through the inhalation of bacilli containing droplets. These droplets are created when people speak, laugh, sing, cough etc, and are then inhaled by people in the near vicinity. It is therefore most likely that people will become infected by someone

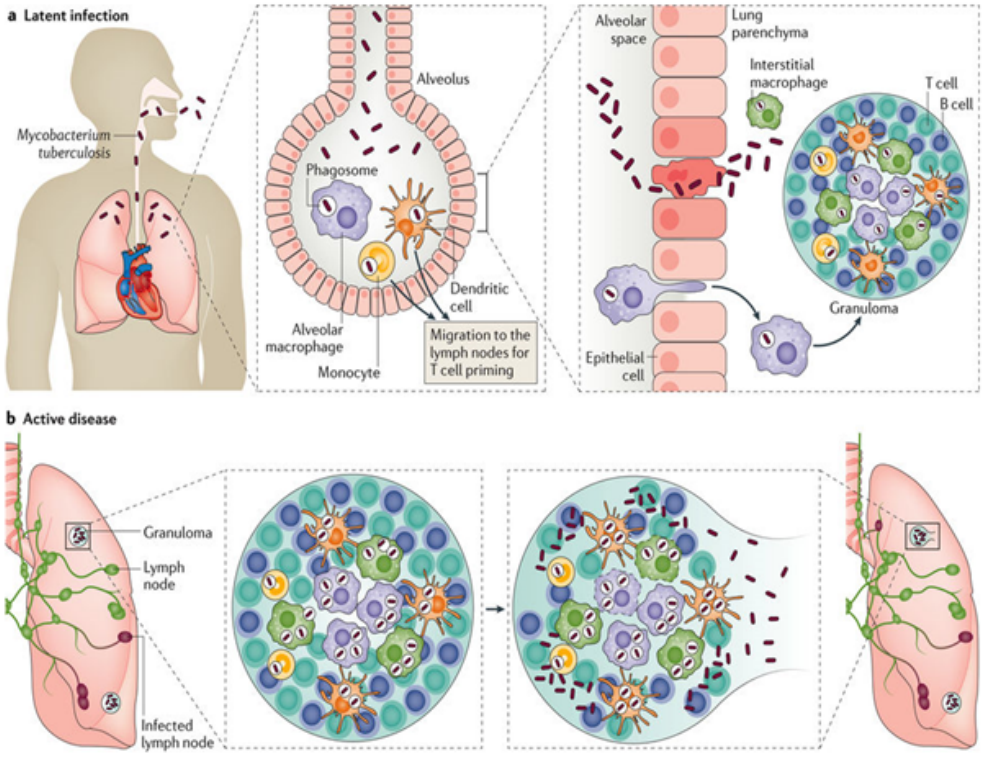

Fig. 2.3 **(a)** Infection begins when *Mycobacterium tuberculosis* enters the lungs via inhalation, reaches the alveolar space and encounters the resident alveolar macrophages. If this first line of defence fails to eliminate the bacteria, *M. tuberculosis* invades the lung interstitial tissue, either by the bacteria directly infecting the alveolar epithelium or the infected alveolar macrophages migrating to the lung parenchyma. Subsequently, either dendritic cells or inflammatory monocytes transport *M. tuberculosis* to pulmonary lymph nodes for T cell priming. This event leads to the recruitment of immune cells, including T cells and B cells, to the lung parenchyma to form a granuloma. **(b)** The bacteria replicate within the growing granuloma. If the bacterial load becomes too great, the granuloma will fail to contain the infection and bacteria will disseminate eventually to other organs, including the brain. At this phase, the bacteria can enter the bloodstream or re-enter the respiratory tract to be released — the infected host is now infectious, symptomatic and is said to have active TB disease [66].

they spend most time with, friends, family, colleagues etc. Contrary to popular belief, TB is not spread by: shaking someone's hand; sharing food or drink; touching bed linens or toilet seats; sharing toothbrushes or kissing [67]. TB transmission from animals to humans can occur, particularly through the presence of *M. bovis* (discussed in greater detail in section 1.6) in contaminated dairy products from infected cattle. The infection caused by *M. bovis* results in only 0.5-1.5% of TB cases in the UK [68] and 2% in the US [69]. This is usually combated via the pasteurisation of milk for direct consumption or the production of other dairy products (cheese, yoghurt, butter etc.). It can also be combated by ensuring the health of the cattle through various pasture management systems [70] and incorporating strict hygiene in industrial practices [71].

2.2.2 Treatment

There are a variety of drugs used to treat TB, of which rifampicin (RIF), ethambutol (ETMB), pyrazinamide (PZ) and isoniazid (INH) are considered the first line of treatment. Drug resistant strains of TB are becoming more and more of a challenge for treatment, rendering monotherapy ineffective. Many variations of drug resistance have been detected which are broadly grouped in the following categories; multidrug resistance (MDR), extensive drug resistance (XDR) and total drug resistance (TDR). MDR refers to high level resistance to rifampicin and isoniazid [72]. An MDR strain that has additional resistance to any of the fluoroquinolone antibiotics (ofloxacin, levofloxacin and moxifloxacin) and to any second line injectable antibiotics (amikacin, kanamycin, and capreomycin) is considered an XDR [73]. XDR TB has been detected in 92 countries and 9.6% of MDR-TB cases progress to XDR-TB [74] [75]. TDR refers to *M. tb* that is insensitive to all forms of anti-TB drugs. TDR *M. tb* have been identified in India, Italy and Iran [76] [77]. Multitherapy is often employed as a more effective treatment method but the absence of rapid diagnostic tools for TB, especially those able to monitor for drug resistance, results in long and ineffective treatment courses

leading to increased rates of transmission and fatality. Furthermore, patients that are unable to stick to treatment regimes for their full length increase the opportunity for creating more resistant strains.

2.3 Surrogate model for TB

There are several challenges when working with M.tb, the greatest of which are its slow growth rate (6-8 weeks) and the requirement for level 3 biosafety facilities to safely handle the bacteria. To address this issue, researchers use other species of mycobacteria such as *M. smegmatis* and *M. abscessus* [78], which are structurally similar but much faster growing and less virulent. These species are classified as Non-Tuberculous Mycobacteria (NTM).

2.3.1 Non-Tuberculous Mycobacteria (NTM)

The NTM grouping refers to all other mycobacteria apart from MTBC (mycobacterium tuberculosis complex) and *Mycobacterium leprae* (which causes leprosy)[79]. There are currently around 200 species of NTM [80]. These can be categorised roughly based on their growth rate into fast-growing (e.g. *M. abscessus*, *M. smegmatis*, *M. chelonae*) and slow-growing (e.g. *M. kansasii*, *M. avium*) varieties. The fast-growing species require 2-3 days to grow on artificial media, with the slow-growing species taking 7 days or more [81]. They are common causative agents for a wide variety of diseases, particularly in immunosuppressed individuals [82][83]. As with M.tb, there is a higher mortality rate associated with patients infected with HIV/AIDS due to their weakened immune system. This can be seen in areas with higher prevalence of HIV/AIDS (shown in fig 2.4 [84]). Treatment can be a major problem in HIV/TB patients as the complex interaction between various anti-retroviral and anti-mycobacterial pharmaceuticals are not always fully understood and can cause harm to the patient [85][86]. The most frequent cause of clinical infection is *M.abscessus*.

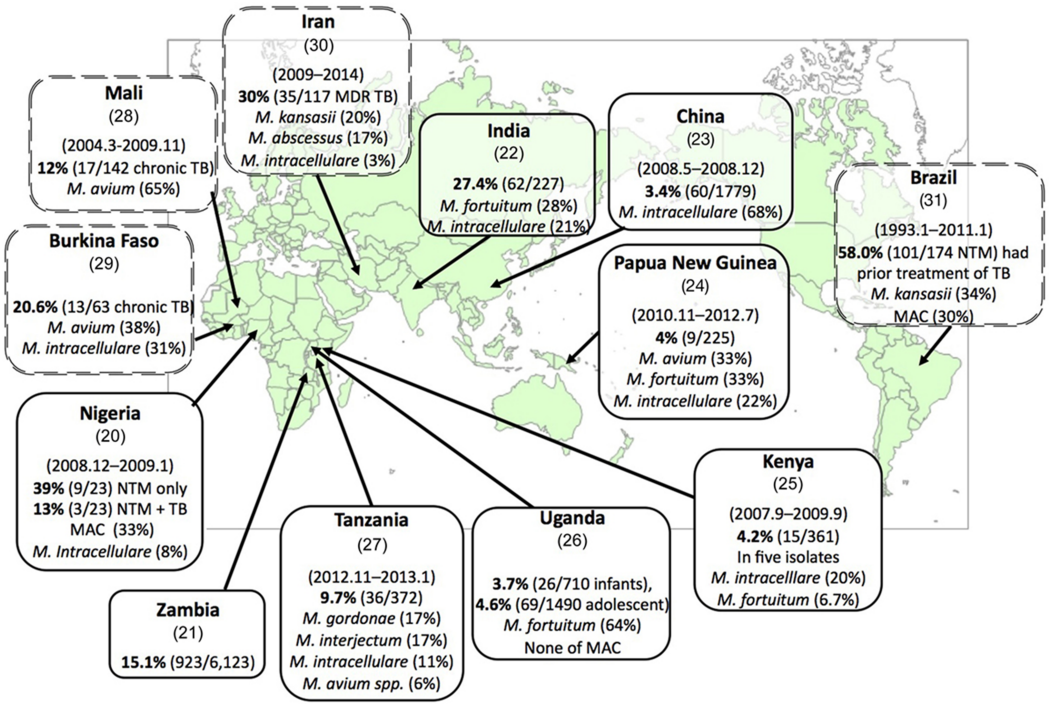

Fig. 2.4 Prevalence and distribution of NTM as monitored in HIV/TB patients across the globe [85].

2.3.2 *Mycobacterium abscessus*

M. abscessus is a fast growing species of nontuberculous mycobacteria first isolated from a knee wound in 1952 [87]. The strain, however, was not recognised as a different species until 1992 [88]. *M. abscessus* causes diseases in numerous organs in the body (including the lungs, skin, eyes etc.) and can cause infection in the bloodstream in compromised individuals [79]. The manifestation of lung infections is particularly prevalent in hosts with prior lung problems such as patients with cystic fibrosis [89], bronchitis [90], or having had tuberculosis in the past [91]. The bacterium is fast growing [92] like *M. smegmatis* and can also be handled in a bio-safety level 2 facility.

M. abscessus has similarly been used as a surrogate for TB in many studies [93], although its use is not as prevalnt as *M. smegmatis*.

While it is a useful surrogate for TB, *M. abscessus* is a pathogen in its own right. Despite being classified as NTM, it is becoming particularly problematic among patients with cystic fibrosis. The presence of *M. abscessus* accelerates the decline in lung function by exacerbating the infection the cystic fibrosis causes [94]. *M. abscessus* has also been shown to have multi-drug resistance similar to TB; drug therapy can take up to 2 years and its failure causes an accelerated lung function decline [95]. The development of a rapid diagnostic for *M. abscessus* would be extremely useful clinically and offers another potential application for the technology proposed in this project.

2.3.3 *Mycobacterium smegmatis*

M. smegmatis is an aerobic fast-growing bacterium, commonly used as a surrogate in TB research [96] and was first isolated in 1885. It is considered non-pathogenic and incapable of causing an immune response, even in immuno-compromised individuals [97]. *M. smegmatis* has a generation time of between 3-4 hours as compared to *M. tb* of 24 hours. The short generation time and ability to be handled at bio-safety level 2 (allowing for safe working) makes it a good choice as a surrogate bacterium.

M. smegmatis has been used in a wide array of studies as a TB surrogate to conduct research for topics like rifampicin resistance [98] [99], as a means of studying DNA repair mechanisms within mycobacteria [100], and much more.

2.4 *Mycobacterium bovis Bacillus Calmette–Guérin (BCG)*

Mycobacterium bovis BCG (sometimes just BCG) is an attenuated form of *M. bovis*. It was first isolated in 1902 [101] and was predominantly used as a vaccine against tuberculosis owing to the structural similarity of the bacteria [102] and its incredibly low toxicity (although there have been reported complications with its use as a vaccine [103][101]). Despite it

being a slow growing mycobacteria, this similarity of structure makes it a gold standard for comparison of techniques to gauge efficacy with tuberculosis.

2.5 Tuberculosis Detection Methods

The emergence of drug resistant TB [104] means that the correct treatment needs to start as quickly as possible to reduce morbidity. Rapid and specific diagnosis methods for TB are thus essential for effective treatment. The common detection methods are summarised below.

2.5.1 Microscopy

This is currently the fastest and least expensive method of *M.tb* detection. *M. tb* is identifiable through an acid-fast staining technique called the Ziehl-Neelsen stain (application and order described in table 2.1 [105]). This process involves adding a stain to a slide containing a small amount of the bacteria, washing it off and then adding a less potent stain. The reagents and relevant colours are shown below.

Application of...	Reagent	Cell Colour	
		Acid Fast	Non-acid Fast
Primary Dye	Carbol Fuchsin 1%	Red	Red
Decolourizer	Acid Alcohol 3%	Red	Colourless
Counter Stain	Methylene Blue 5g/l	Red	Blue

Table 2.1 Dyes, order of application and relevant outcomes of a Ziehl-Neelsen test

When observed at 100x magnification using a light microscope, the bacterium appears red since it is an acid-fast bacterium (as shown in fig 2.5 [105], non acid-fast bacteria would appear blue). Unfortunately, this test can only detect *M. tb* at concentrations above 5000 bacteria per ml of original sample (in sputum), demonstrating low sensitivity and meaning

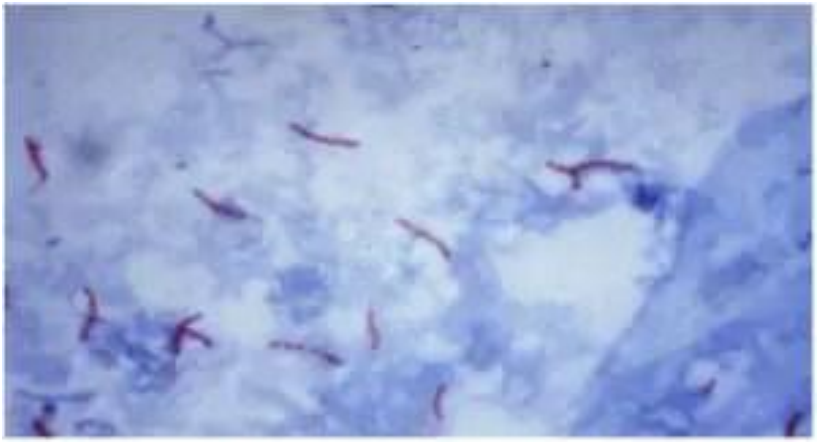

Fig. 2.5 Acid-Fast Stain, Mycobacterium tuberculosis [107]

it will potentially miss low level infections (as few as 10-100 bacilli can cause a positive culture) [106] [107]. This method also requires expensive equipment (microscopes, slides etc) and well-trained staff to perform. It can also not distinguish between pathogenic and non-pathogenic acid-fast bacteria. There are also several alternative methods using fluorescent microscopy, involving an initial staining with auramine O, which increases the sensitivity of the test. However, these require an expensive mercury lamp, which tends to break easily. They also require a continuous power source as well as a dark room. The use of LED lamps has also been explored to perform fluorescent microscopy. Marais and colleagues compared the sensitivity and specificity of microscopy using standard light, mercury and LED lamps [108]. While the level of specificity was similar (99% for all methods), sensitivity increased from 61.1% (for standard light) to 73.6% (for mercury lamps) and then to 84.7% for LED sources. LED sources showing a vast improvement over standard light and even mercury lamps.

2.5.2 Chest X-Ray

Chest x-rays (shown in fig 2.6 [109]) have been used in the diagnosis of TB for over a century. However, alone it is insufficient for a complete diagnosis as other diseases such as neoplasma

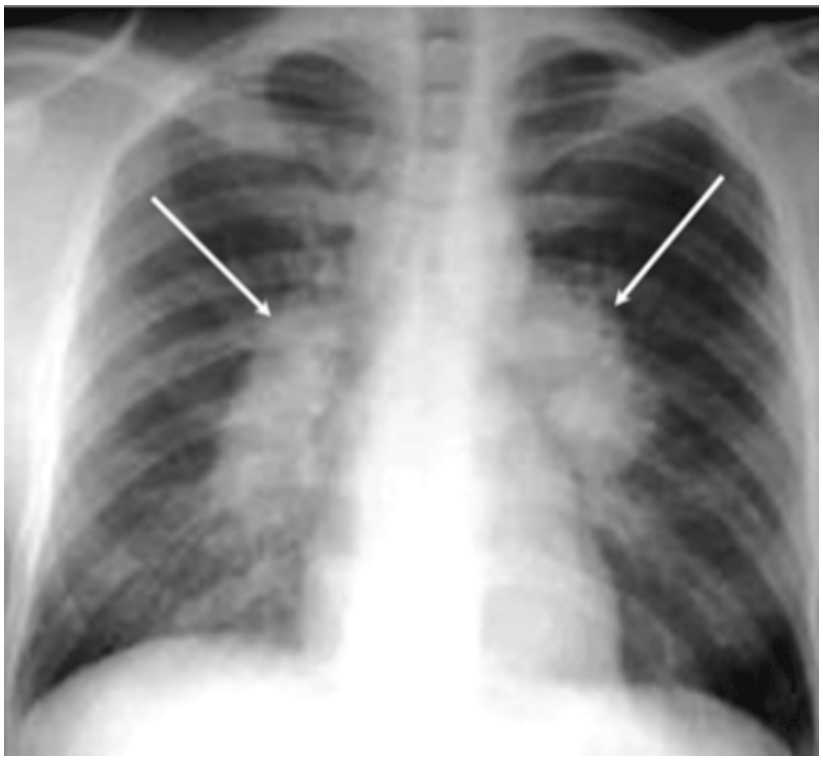

Fig. 2.6 Chest x-ray showing bilateral hilar adenopathy of primary pulmonary TB [111]

and sarcoidosis present with similar evidence [110]. It needs to be used in conjunction with other methods to provide a TB diagnosis.

The reliability of a chest x-ray is highly dependent on the observer's ability to interpret the image (shown in fig 2.6). It has been reported to have a sensitivity of between 73-79% and a specificity of between 60-63% [111]. A Computerised Tomography (CT) scan (a more powerful and sensitive imaging tool) can also be used as a diagnostic method with a sensitivity twice as high as a chest x-ray [112]. The use of a chest x-ray has several major limitations, mainly the necessity for a confirmation test following the x-ray. Additionally, x-ray machines are costly, as is the need for a trained radiologist to operate them. There are also minor health hazard concerns due to exposure to radiation.

2.5.3 Mycobacterial Culture

Culture is the most reliable method of detecting the presence of the pathogen in a sample. It is a simple test, requiring a sample of sputum (exceeding 5ml [113]) to be added to a suitable growth medium; if the bacteria grow then the test is positive, if not, it is negative. Sheen and colleagues compared two such cultures, Microagar 7H11 and Löwenstein–Jensen medium, along with several other methods [114]. These contain casein enzymic hydrolysate, ammonium sulphate, monopotassium phosphate, disodium phosphate, sodium citrate, magnesium sulphate, L-glutamic acid, ferric ammonium citrate, pyridoxine, biotin, malachite green, agar, and potassium dihydrogen phosphate anhydrous, magnesium sulphate anhydrous, magnesium citrate, asparagine, glycerol, distilled water, malachite green dye, homogenised whole eggs, respectively. The test has a high specificity of 98%, however, it has low sensitivity of 26-42% [115] when compared to culture positive TB cases.

The recovery of the bacteria requires a first step in which the number of contaminating, non-tuberculosis bacteria is reduced (using decontamination kits, such as BD BBL MycoPrep) to make it easier to identify the presence of the pathogen. Unfortunately, in addition to reducing the number of bacteria derived from the normal flora of the upper respiratory tract, this decontamination step can also reduce the number of *M.tb* which are present, thus decreasing the sensitivity of the test [115]. This can be countered in part by increasing the volume of sputum to be cultured. The major limitations of this method are that it can take 4-8 weeks to generate a result and to do so requires highly trained lab technicians, as well as access to bio-safety facilities to protect the laboratory staff. The identification of bacteria in this method is presumptive and requires confirmation using an additional diagnostic method. It also does not yield any information about any antibiotic resistance present in the isolate.

2.5.4 Immunological Methods

It can be challenging to perform direct detection of *M.tb* bacilli from patients unable to provide suitable sputum samples (young children and HIV infected patients are examples of this) [116]. A bronchoscopy can be employed when a sputum smear is negative but is often not used as it is an invasive and expensive procedure [117]. Serological methods can be useful in these cases as the collection of blood and urine samples should cause few problems for the patient. Immunological assays can be categorised as either indirect assays (which detect the patient's immune response to the pathogen) or direct assays (which target the bacterium itself).

2.5.5 Tuberculin Skin Test (TST)

Another example of *M. tb* diagnosis is the tuberculin skin test (TST). TST has been used for diagnosing TB and latent forms of TB in the clinic and in most screening centres [118]. TST is based on the injection of mycobacterial proteins prepared from cultures of *M. tb* [118]. The purified protein derivative (PPD) induces a delayed-type hypersensitivity reaction as a result of the release of interferon gamma (INF-γ) at the site of injection [119]. This causes the skin to harden (known as induration) which is then observed to ascertain whether a person is infected with TB (various outcomes shown in fig. 2.7 [120]). One of the major problems with TST is its specificity. It is also not specific to *M. tb*, as the proteins used are found in other species of mycobacteria such as *M. bovis* and other nontuberculous mycobacteria. Also, after the injection of PPD proteins, it takes 2-3 days for an induration to form in the skin [121]. The need to follow-up on patients may not be successful in some cases as active TB patients may be missed/uncontactable.

Fig. 2.7 Demonstration of different results of a tuberculin skin test and likely contributory factors. Figure reproduced from: *"Interferon gamma release assays for latent tuberculosis: What are the sources of variability?"*, Banaei N. et al [122]

2.5.6 Interferon Gamma Release Assays

Interferon gamma release assays (IGRAs) are blood-based tests intended for diagnosis of latent tuberculosis infection (LTBI). IGRAs are ex vivo assays that measure T-cell response after overnight stimulation with antigens that are relatively specific for *M. tb*. As such they are slightly faster than TSTs as results can be available within 24 hours [122]. The two most widely used IGRAs include the QuantiFERON-TB Gold In-Tube (QFT-GIT) assay (Cellestis/Qiagen, Carnegie, Australia) and the T-SPOT.TB (T-SPOT) assay (Oxford Immunotec, Abingdon, United Kingdom). IGRAs are limited by the necessity for a lab and expensive equipment, as well as the need for trained staff to perform.

2.5.7 Antigen Based Detection

M.tb growth in the body produces antigenic substances which are released into various body fluids such as urine, blood, cerebrospinal fluid, and pleural fluid. These substances can be detected by using the enzyme-linked immunosorbent assay (ELISA) technique [118]. This method looks for the most prominent of these antigens, called Lipoarabinomannan [123], which is present in the urine of active TB patients. The testing kits have a reported sensitivity and specificity of 89.0% and 98.1%, respectively, compared to culture confirmed TB [124]. This technique, however, does not give information about the antibiotic sensitivity of the target pathogen and it is expensive and requires extensive training to perform.

2.5.8 High Performance Liquid Chromatography (HPLC)

HPLC is predominantly used to analyse different components of small liquid samples (of μl volume). Samples are injected into a stream of liquid which then passes through a column (defined as the mobile and stationary phases, respectively). The assay is equipped with detectors which identify the different components within the sample, thereby generating a distinct chromatograph unique to the sample added (as shown in fig 2.8) [125]. The efficiency of separation is dependent on the degree of sample retention within the column [126]. These chromatographs must then be compared with an appropriate standard to yield a diagnostic result. For mycobacteria, HPLC presents the distribution of mycolic acids, which are unique to species [127].

The mycolic acids must first be extracted from pure cultures of the bacterium before they can be analysed. The specificity can be improved by growing the cultures on solid media as opposed to liquid media, as the liquid media is more likely to contain contaminants [127]. The HPLC method itself takes around 2 hours to complete (but also requires the time taken to grow the bacteria and the time taken to extract the mycolic acid) and has 100% sensitivity [128]. The method is highly sophisticated and requires costly reagents and high

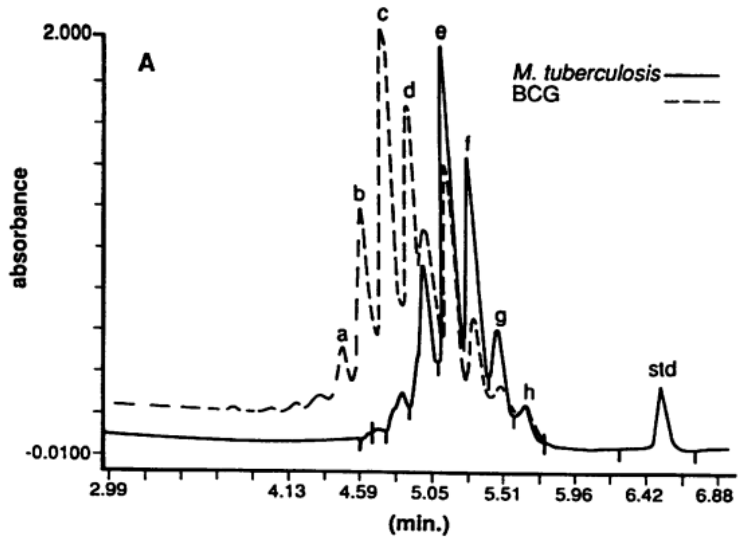

Fig. 2.8 Chromatographs of M.tuberculosis and M.bovis (BCG) created using HPLC [127]

level training. Frequency-pulsed electron-capture gas-liquid chromatography has been used to demonstrate the presence of tuberculostearic acid in the cerebrospinal fluid of patients with lymphocytic meningitis patients, strongly suggesting the presence of *M. tuberculosis*. Results from 41 coded cases and 75 clinical cases showed that the frequency-pulsed electron-capture gas-liquid chromatography test had a specificity of 91% and a sensitivity of 95% [129].

2.5.9 DNA Based Methods

DNA methods have proved very effective in the identification of bacteria, as well as ascertaining any antibiotic resistance within, comparatively, a very short time (when comparing to bacterial culture) [130]. However, they are all similarly limited by the necessity for the DNA to be extracted before the detection can take place, which is often a lengthy additional step (1-3hrs). They also require a purification stage to ensure the DNA can be amplified to a level at which it can be detected. These stages require expensive equipment and well-trained personnel, which are not always available. There are 2 main types of DNA detection; detection using probes, which requires no amplification of the target DNA but the sensitivity

is limited greatly by the number of pathogens in a given sample (if the number is too small then the DNA will not be detected), the second involves an amplification stage to amplify exponentially the amount of target DNA by creating copies (using PCR).

2.5.10 PCR and LAMP Methods

Polymerase Chain Reaction (PCR) is a method of rapid DNA amplification by the copying of an initial nucleic acid strand via multiple stages of heating and cooling (thermocycling). Common PCR methods are able to replicate DNA sequences between 0.1 and 10 kilo base pairs (kbp) in length, but they can go up to 40 kbp [131]. Generally, PCR involves 3 steps (demonstrated in fig 2.9 [132]) which are repeated 20-40 times. These three steps are:

Denaturation:

- The target DNA is heated up to 94-98°C, which breaks down the bonds between the strands yielding two single stranded fragments of DNA; this takes 20-30 seconds.

Annealing:

- This occurs at 50-65°C and allows PCR primers (complimentary fragments which attach to specific sequences at each end of the DNA singles strands, time to bind to the target DNA; this takes 20-40 seconds).

Extension:

- DNA polymerase is added which, at 72°C (60°C for qPCR), adds complimentary nucleotides to each growing DNA strand ([133]; [134]); this commonly occurs at a rate of 1000 base pairs per minute so can take up to 10 minutes with a large target fragment.

In total PCR can take 45 min to an hour to complete 40 cycles [135].

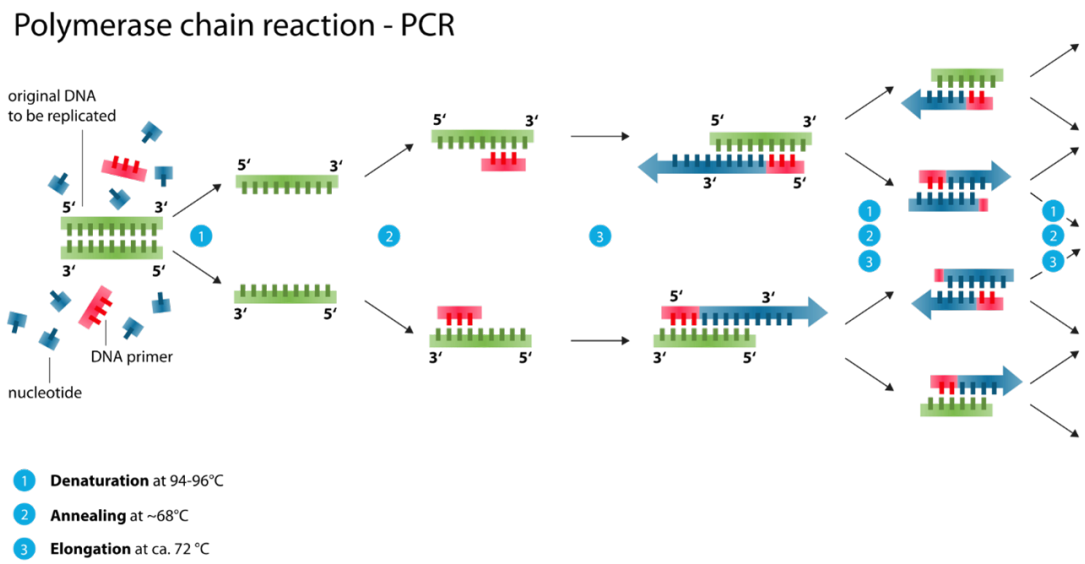

Fig. 2.9 Diagram depicting the different stages of PCR, this denotes a single cycle [134]

The production of target DNA is exponential so after 40 cycles of amplification the PCR can produce ∼1 trillion copies (amplicons) of the starting DNA sequence. The size of these amplicons is then verified using agarose gel electrophoresis (requiring additional specialised equipment, qPCR does not require this stage). PCR is sensitive to contamination, biological material derived from the host or the environment which can inhibit the reaction. For this reason, the target DNA must be as pure as possible, thus requiring an additional purification step (∼2 hours [136]). The PCR itself also requires very expensive equipment and highly trained personnel to perform.

In contrast to PCR, isothermal amplification relies on the generation of DNA amplicons by autocycling and strand displacement process at a constant temperature [137], the process being mediated by a special polymerase (*Bst*). This process is faster than traditional PCR and does not require electrophoresis as the amplicons are observed by a colour change in the assay. Loop mediated isothermal amplification (LAMP) [137][138] and transcription mediated amplification [139] are examples of isothermal detection. The performance of the LAMP assays has been evaluated targeting two different *M. tb* gene sequences (*rrs* and *gyrB*).

The former demonstrated a sensitivity of 100% and specificity of 94.2% [140] whereas the latter demonstrated a sensitivity of 97% in smear-positive, culture positive specimens and 48.8% in smear negative but culture positive specimens, respectively [141]. Despite their improvements over standard PCR, these assays still require a lengthy initial DNA purification stage [73]. They also require expensive cold storage to guarantee reproducibility, reducing feasibility in low resource environments.

2.5.11 GeneXpert MTB/RIF assay

This is a real time commercial DNA detection assay based on the PCR reaction which has been developed to detect *M.tb* in sputum samples [142]. The maximum sensitivity and specificity of this test were both demonstrated as 98% [143]. The assay requires 15 minutes of preparatory work beforehand and then 120 mins for detection of the target DNA. It is also able to detect mutations within the gene which confers resistance to the antibiotic rifampicin, at a sensitivity and specificity of 94 and 97%, respectively, when compared to smear positive and smear negative TB [143]. The result from the assay allows effective decisions to be made in the time frame of a patient consultation as to the most appropriate antibiotics to prescribe. The widespread use of this system in low income economies is limited by the relatively high cost of the assay ($10) and the fact that it can only detect resistance to rifampicin [144]. It also requires relatively expensive equipment, a source of mains power and trained individuals. Several other similar assays (MTBDRplus, MTBDRsI and INNO-LiPA) have been developed to detect for the presence of gene sequences encoding resistance to rifampicin, isoniazid, and fluoroquinolone ([128], [145], [146], [147], [148]). These assays have similar limitations being expensive, requiring high level training and resistance detection to only one specific TB drug.

2.6 Limitations of current methods

There are several limitations of the previously mentioned methods which make them less than ideal for low resource environments. While bacterial culture is the current gold standard test, it can take up to 8 weeks for a result and requires expensive equipment, as well as highly trained practitioners. Microscopy cuts down on diagnosis time but also requires expensive and highly perishable equipment (mercury lamp). Both of these methods also suffer from low sensitivity. Alternative methods such as Antigen based, PCR, LAMP and GeneXpert assays commonly obtain results within 1-2 hours with high specificity when provided with samples of purified target DNA; however, they require expensive equipment and staff training to perform. The time taken to generating target DNA of a suitable level of purity to support DNA based assays can lengthen considerably the time taken to generate a result.

2.7 DNA Extraction Methods

As mentioned previously, the first stage in current DNA based detection methods is the extraction and purification of the DNA from the target pathogen. Boiling is a very simple method of extracting DNA from a pathogen, but, it is often difficult to optimise this method as temperature within an aqueous sample is often non-homogeneous and can cause destruction of the target DNA if left too long. It is also non-specific to any particular pathogen. Sonication can also be used as a method for DNA extraction. It is a rapid method, producing results in under 30 mins from multiple tissue types in various media [149] but it is non-specific to any particular pathogen and can cause damage to released DNA if over exposed to the heat generated, both methods can cause aerosolization of the target pathogen causing spreading/contamination through the air.

Many multipurpose kits exist to extract DNA using chemical methods, an example of which is the DNeasy Blood and Tissue Kit [150]. The cells are initially lysed using

a proteinase then the resulting sample is passed through a DNA retaining mesh using a centrifuge. The unwanted components are then washed away to give a highly purified sample of DNA. This method yields between 6-30µg of DNA for a sample volume of 100µl, with a process time of under 1 hour [150]. DNAzol is a low-cost reagent for isolating DNA. The sample is lysed using the DNAzol then the DNA can be removed and washed using ethanol. The method takes up to 30 minutes and can extract up to 100% of the DNA from a maximum of $3 \times 10^7 CFU/ml$ (far more than present in any clinical sample) [151].

Bead beating is another common method of extracting DNA from bacterial samples. This simply involves adding beads to a sample then agitating the sample in a bead beater. This shakes the vessel and causes the beads to pulverise the sample, so releasing the DNA. One advantage it has over chemical methods is that the type of microorganism involved is irrelevant if care is taken with microorganisms with thin walls, as the method can destroy the DNA [152]. A study by de Boer and colleagues compared two types of beads, one made from silica and measuring 0.1mm, the other ceramic and measuring 1.4mm. They demonstrated the amplifying effect of each of these bead beating methods when used in combination with the MagNA Pure DNA III extraction kit on 4 different bacteria *E. coli*, *S. aureus*, *S. cerevisiae* and *M. marinum*. The results show that the 0.1mm beads have the most positive effect on the percentage of DNA extraction, and one of the best results reported occurred with *M. marinum*, which gives an average of 10% increase in DNA yield compared to just the kit itself [153].

This chapter has reviewed the literature surrounding *M. tb*, the disease TB, and detection methods used for its diagnosis including their respective benefits and limitations. Various DNA extraction methods have been discussed and their limitations analysed for the aim of the project. The following chapter discusses the background of microwave theory and the design of a cartridge model to promote microwave interactions with a 10ml sample volume.

Chapter 3

Optimization of Cartridge Geometry to Promote Microwave Interactions

3.1 Introduction - What are Microwaves?

Microwaves form part of the electromagnetic wave spectrum with free space wavelengths of between 1 to 30 cm, corresponding to frequencies of 30GHz and 1GHz, respectively. They have been used to heat food since the end of the Second World War [154]. They provide a heating effect by causing polar molecules (such as water) to rotate. This kinetic energy is transferred to heat by the frictional dissipation associated with the making and breaking of hydrogen bonds, since liquid water molecules are kept in intimate contact by their hydrogen bonding network. As the purpose of this research is to release ssDNA from bacteria within sputum samples (mostly consisting of water), microwaves act as a convenient and efficient way of transferring thermal energy into the sample.

3.2 Microwave Cavity Theory

The microwave applicator in this work is a microwave cavity, an example of which is the domestic microwave oven. These can be designed with precise resonant frequencies and have precise positions within the cavity space where samples can be exposed to either electric or magnetic fields, and also a mixture of both. They are also easily matched to the microwave power electronics so that the microwave exposure can be precisely described, both in terms of power and microwave field strength. A microwave cavity is an enclosed metallic structure filled with a dielectric material (often air) which traps microwaves by reflecting them back and forth between its boundaries, creating standing waves of electric and magnetic fields. Standing waves are produced in a cavity owing to the almost perfect reflection of a microwave from a metallic surface (as with all EM waves of frequencies up to blue light).

The origin of reflection lies in the so-called field boundary conditions, where electric fields parallel to any metal surfaces are reduced to zero on reflection as the free electrons within the metal structure flow to cancel out this E field. This movement of electrons within the surface of the material in turn creates an electromagnetic wave which propagates perpendicular to the metallic surface but in the opposite direction to the incoming wave. By suitable cavity design, these two waves are made to constructively interfere and create a standing wave (in 1D, by having two such reflectors, separated by a multiple of half wavelengths apart). This then sets up the resonant frequency. Each cavity has a set (or spectrum) of discrete resonant frequencies, related to its geometry. The cavities are able to support electromagnetic waves of a fundamental frequency, as well as higher harmonics of this frequency. Cavities act as a bandpass filters by attenuating all other frequencies that pass into it. This is beneficial as it allows very specific frequencies to be maintained. There are two main types of cavity that are used with any regularity; these are rectangular and cylindrical cavities.

3.2.1 Cavity Modes

Cavity resonances are called modes, each with their own unique pattern of electric and magnetic fields. There are two major types of mode within these cavities, TM_{mnl} and TE_{mnl}. These describe the behaviour of the electric and magnetic fields inside the cavities, based on the direction of propagation of the travelling waves that form the standing wave resonances.

A TE mode exists when there is no electric field in the direction of propagation.
A TM mode exists when there is no magnetic field in the direction of propagation.

For cylindrical modes, the direction of propagation is always in the direction of the cylinder's axis. Therefore, these modes are clearly defined. However, with rectangular cavities the two modes become slightly more intertwined, as there is no unique direction of propagation. TE modes can be changed into TM modes (and vice versa) by simply switching the lengths of its sides, i.e. by rotating the field patterns by 90 degrees. For this reason, all rectangular modes can be thought of as TE modes to simplify their description.

The electric field amplitude distribution between a single pair of metal plates (which act as "mirrors") is shown in fig 3.1 below [155], where frequencies of the harmonics are simply integer multiples of the fundamental frequency.

In 3D, the integers m,n,l link to the harmonic number for each dimension of the cavity. For a rectangular cavity, the standing waves are created between three pairs of orthogonal, parallel metal surfaces (forming an enclosed box, i.e. "cavity"). The integers m,n or l give the number of half wavelengths across three pairs of parallel surfaces. This is analogous to the principal quantum numbers of a "particle in a box", as both are based on solutions to the wave equation with the same boundary conditions.

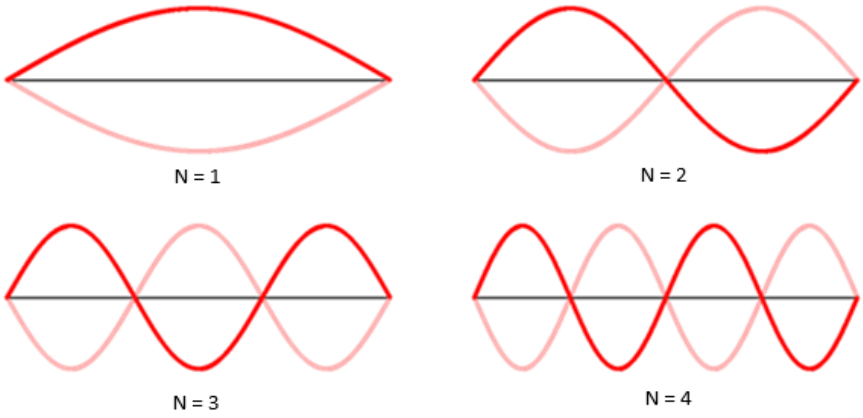

Fig. 3.1 Wave Harmonics [158]

3.2.2 Rectangular Cavities

A rectangular cavity is cuboid shaped with a resonant frequency that can be defined through its physical dimensions (namely length, width, and height).

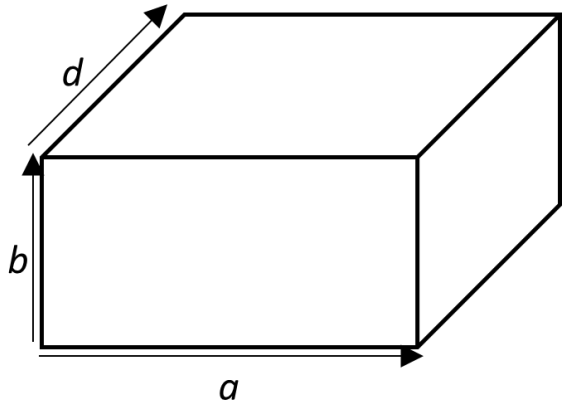

Fig. 3.2 Rectangular Cavity

The resonant frequency of this can be found using with the equation:

$$f_{mnl} = \frac{c}{2\sqrt{\mu_r \varepsilon_r}} \sqrt{\left(\frac{m}{a}\right)^2 + \left(\frac{n}{b}\right)^2 + \left(\frac{l}{d}\right)^2} \tag{3.1}$$

where:

- ***mnl*** describes the mode of the cavity (each denotes an integer, one of which can be zero)

- ***c*** is the speed of light in a vacuum

- μ_r is the relative permeability of any material filling the cavity (≈ 1 for air)

- ε_r is the relative permittivity of any material filling the cavity (≈ 1 for air)

- ***a,b*** and ***d*** link to the width, height and length of the cavity, respectively.

3.2.3 Cylindrical Cavities

The geometrical basis for cylindrical resonators are easier to define than rectangular cavities as a cylinder can be described using only 2 parameters, the radius, a, of is cross sectional circle and its height, d. It also has a unique axial direction, allowing distinct TE and TM modes to be defined.

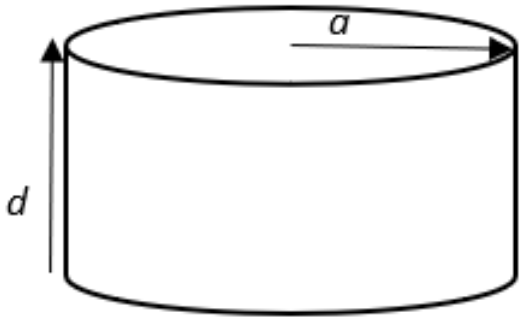

Fig. 3.3 Cylindrical Cavity

Here the resonant frequency can be defined based on these two parameters:

$$f_{mnl} = \frac{c}{2\sqrt{\mu_r \varepsilon_r}} \sqrt{\left(\frac{p_{mn}}{a}\right)^2 + \left(\frac{\pi l}{d}\right)^2}, \; for\ TM\ cavities \tag{3.2}$$

$$f_{mnl} = \frac{c}{2\sqrt{\mu_r \varepsilon_r}} \sqrt{\left(\frac{p'_{mn}}{a}\right)^2 + \left(\frac{\pi l}{d}\right)^2}, \; for\; TE\; cavities \tag{3.3}$$

where:

- ***mnl*** describes the mode of the cavity
- ***c*** is the speed of light
- μ_r is the relative permeability of any material filling the cavity
- ε_r is the relative permittivity of any material filling the cavity

p_{mn} is the n-th zero of the m-th Bessel function. The standing waves in a cylinder follow the shape of a Bessel function rather than sinusoidal functions in rectangular cavities. Here, p'_{mn} are the zero values of the derivative of the Bessel function.

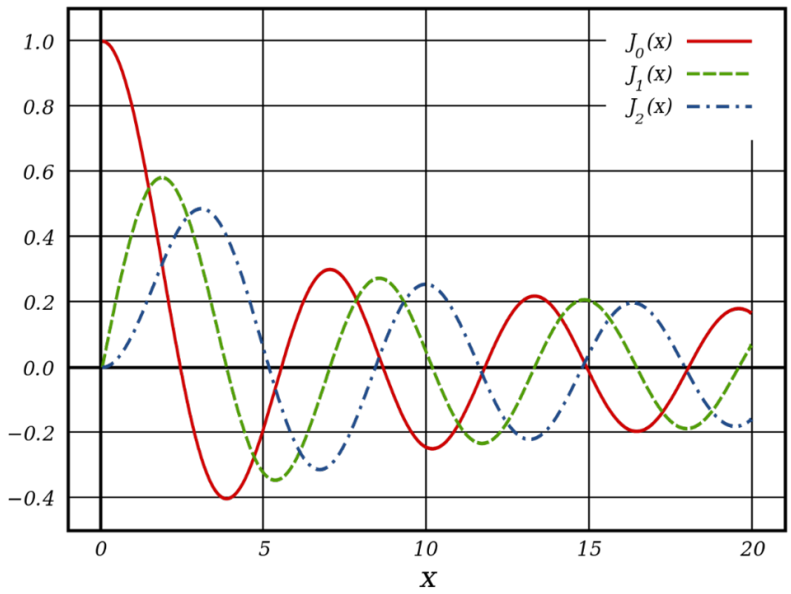

Fig. 3.4 Bessel Functions, 0th ,1st and 2nd order.

If designing a TM_{010} cavity the p_{mn} term is taken as p_{01}. The 0-th Bessel function ($J_0(x)$) is shown in red above and the 1-st zero is at 2.405, hence p_{01} = 2.405. This mode has an electric field along the cylinder axis, where the sample is placed.

3.2.4 Field Distributions in a Cylindrical Cavity

Using a standard TM_{010} cylindrical cavity, the electric field in the cavity can be modelled using a standard wave equation with the Bessel function relationship added:

$$E_z = E_0 J_0(2.405\frac{r}{a})e^{j\omega t} \tag{3.4}$$

The magnetic field using Faraday's Law:

$$\nabla \times \underline{E} = -\frac{\partial \underline{B}}{\partial t} = -j\omega\mu_0 \underline{H} \tag{3.5}$$

$$\nabla \times \underline{E} = \begin{vmatrix} \underline{\hat{a}}_r & \underline{\hat{a}}_\theta & \underline{\hat{a}}_z \\ \frac{\partial}{\partial r} & \frac{1}{r}\frac{\partial}{\partial \theta} & \frac{\partial}{\partial} z \\ 0 & 0 & E_z \end{vmatrix} = -\frac{\partial E_z}{\partial r}\underline{\hat{a}}_\theta \tag{3.6}$$

$$-\frac{\partial E_z}{\partial r} = -j\omega\mu_0 H_\theta \tag{3.7}$$

$$H_\theta = \frac{1}{j\omega\mu_0}\frac{\partial E_z}{\partial r} \tag{3.8}$$

$$H_\theta = \frac{1}{j\omega\mu_0}\frac{\partial}{\partial r}E_0 J_0(2.405\frac{r}{a})e^{j\omega t} = \frac{1}{j\omega\mu_0}\frac{-2.405}{a}E_0 J_1(2.405\frac{r}{a})e^{j\omega t} \tag{3.9}$$

When l = 0, the TM frequncy equation reduces to:

$$f = 2.405\frac{c}{2\pi a}, \quad \omega = 2\pi f = 2.405\frac{c}{a} \tag{3.10}$$

This can then be substituted back into the previous equation to give:

$$H_\theta = \frac{j}{c\mu_0}E_0 J_1(2.405\frac{r}{a})e^{j\omega t} \tag{3.11}$$

$$c = \frac{1}{\sqrt{\varepsilon_0\mu_0}}, \quad c\mu_0 = \sqrt{\frac{\mu_0}{\varepsilon_0}} = \eta_0 \tag{3.12}$$

where η_0 is the impedance of free space, approximately 377Ω.

This leaves:

$$H_\theta = j\frac{E_0}{\eta_0}E_0 J_1(2.405\frac{r}{a})e^{j\omega t} \tag{3.13}$$

$$E_z = E_0 J_0(2.405\frac{r}{a})e^{j\omega t} \tag{3.14}$$

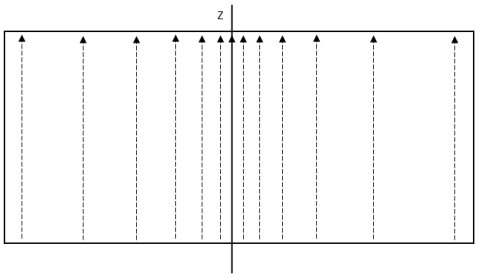

(a) Electric Field in TM_{010} Cylindrical cavity

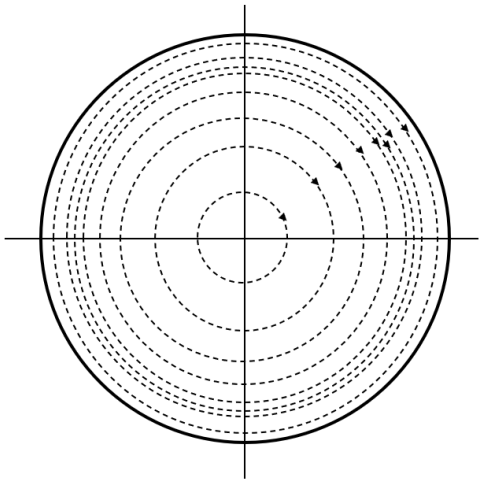

(b) Magnetic Field in TM_{010} Cylindrical cavity

Fig. 3.5 Demonstration of the distribution of Electric and Magnetic fields inside a TM_{010} Cylindical Cavity. The proximity of the dotted lines demonstrates the area of highest field strength respectively. The e-field is strongest at the centre whereas the m-field is strongest at a point just in from the inner edge of the cavity.

3.2.5 Q-Factor

The Q-factor quantifies the losses in the cavity and is defined via the ratio of stored energy and energy lost per cycle (i.e. high Q when losses are small). The Q-factor is usually separated into two different values; Q_c, which is the loss from the limited conductivity in the cavity material, and Q_d which is related to the loss in the dielectric filling the cavity. From its fundamental definition we can write:

$$Q = \frac{\omega \langle \text{Energy Stored} \rangle}{\langle \text{Power Dissipated} \rangle} \tag{3.15}$$

Since losses are additive:

$$Q = \left(\frac{1}{Q_c} + \frac{1}{Q_d}\right)^{-1}, \quad Q_c = \frac{Gf_0}{R_s}, \quad Q_d = \frac{1}{\tan\delta} \tag{3.16}$$

- $tan\delta$ is the loss tangent of the dielectric filling the cavity
- R_s is the surface resistance of the metal walls of the cavity.
- G is a geometrical factor for the mode being studied, which can be calculated from the EM field distribution.

Any electrically lossy sample added to a cavity will cause the power dissipation within the cavity to increase, hence the Q-factor will decrease. This can be used to gauge how well a certain sample couples to the electric field within the cavity when placed in an anti-node of an electric field.

3.2.6 Two Port Networks

Two Port Network theory offers an accurate way of measuring the properties of a system without having to directly measure inside the system. This is done by measuring the signals entering and leaving the system and calculating several parameters, the S-Parameters. A standard two port network is shown in fig 3.6.

The S-Parameters describe the relationships between the input and output voltages at each port in a given network. For two-port network the S-Parameters are defined as shown in fig. 3.7.

The microwave cavities used in this project are set-up as either a two-port or single-port system. The two-port set-up is used for characterization of the cavity as it becomes

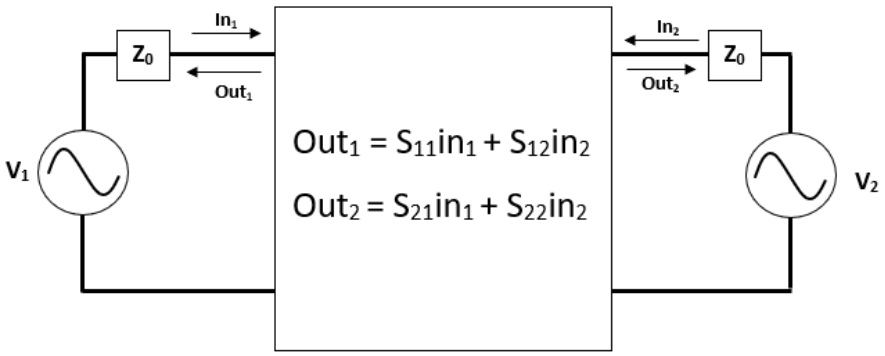

Fig. 3.6 A simple two-port network with S-Parameters

$$S_{11} = \left.\frac{V_{out_1}}{V_{in_1}}\right|_{V_{in_2}=0} \qquad S_{12} = \left.\frac{V_{out_1}}{V_{in_2}}\right|_{V_{in_1}=0}$$

$$S_{21} = \left.\frac{V_{out_2}}{V_{in_1}}\right|_{V_{in_2}=0} \qquad S_{22} = \left.\frac{V_{out_2}}{V_{in_2}}\right|_{V_{in_1}=0}$$

Fig. 3.7 Definitions of S-Parameters in the two-port network

significantly easier to measure the bandwidth and Q-factor using S21 measurements. This is implemented using two SMA connectors with permanent metallic loops inserted into the cavity directly opposite each other.

The single-port set-up is used for excitation as the secondary port becomes obsolete and can cause sparking in higher power experiments. This uses a single open N connector with a larger metallic loop. The loop is adjustable and can be both moved in and out of the cavity as well as rotated to find the best coupling angle. S parameters for characterisation are measured at low power (0dBm) using a vector network analyser.

3.2.7 Microwave Resonator Analysis

A standard LRC circuit to model and analyse the behaviour of our microwave resonator. As the cavity is coupled to inductively (using metallic loops), we use the following model. This relates to the two-port-setup using SMA connector as described above.

The loops are modelled as a pair of mutual inductances at port 1 and 2, m_1 and m_2 respectively. As the loops used for characterisation are identical it can be assumed that $m_1 = m_2 = m$ (i.e. "symmetric coupling").

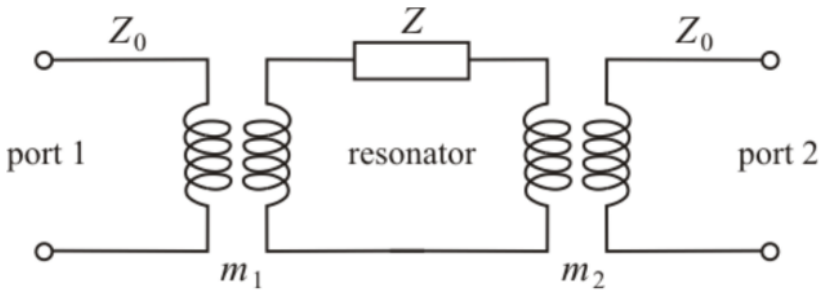

Fig. 3.8 The equivalent circuit of a two port, loop-coupled resonator. The resonator is modelled as a series LRC circuit, of impedance Z

The frequency, impedance and unloaded quality factor are given as:

$$\omega_0 = \frac{1}{\sqrt{LC}}, \qquad Z = R + j\omega L + \frac{1}{j\omega C}, \qquad Q = \frac{\omega_0 L}{R} \tag{3.17}$$

The transfer matrix for each coupling loop is that of a transformer:

$$\begin{pmatrix} 0 & -j\omega m \\ \frac{1}{j\omega m} & 0 \end{pmatrix} \tag{3.18}$$

The full transfer matrix for the entire resonator circuit is found by calculating the following:

$$\begin{pmatrix} a & b \\ c & d \end{pmatrix} = \pm \begin{pmatrix} 0 & -j\omega m_1 \\ \frac{1}{j\omega m_1} & 0 \end{pmatrix} \begin{pmatrix} 1 & Z \\ 0 & 1 \end{pmatrix} \begin{pmatrix} 0 & -j\omega m_2 \\ \frac{1}{j\omega m_2} & 0 \end{pmatrix} = \pm \begin{pmatrix} \frac{m_1}{m_2} & 0 \\ \frac{Z}{\omega^2 m_1 m_2} & \frac{m_2}{m_1} \end{pmatrix} \tag{3.19}$$

The impedance (Z) can be redefined as:

$$Z = R + j\omega L \left(\frac{\omega}{\omega_0} - \frac{\omega_0}{\omega} \right) \tag{3.20}$$

$\Delta\omega = \omega - \omega_0$ can be substituted in for frequencies close to resonance to yield:

$$Z \approx R + 2jL\Delta\omega = R \left(1 + 2j \frac{\omega_0 L}{R} \frac{\omega - \omega_0}{\omega} \right) = R \left(1 + 2jQ_0 \frac{\omega - \omega_0}{\omega} \right) \tag{3.21}$$

The four elements of the transfer matrix then become:

$$a = \pm \frac{m_1}{m_2}, \quad b = 0, \quad c = \frac{R}{\omega^2 m_1 m_2} \left(1 + 2jQ_0 \frac{\omega - \omega_0}{\omega} \right), \quad d = \pm \frac{m_2}{m_1} \tag{3.22}$$

The S_{21} parameter is defined as:

$$S_{21} = \frac{2}{a + \frac{b}{Z_0} + cZ_0 + d} \tag{3.23}$$

This becomes:

$$S_{21} = \pm \frac{2\sqrt{g_1 g_2}}{g_1 + g_2 + 1 + 2jQ_0 \frac{\omega - \omega_0}{\omega}} \rightarrow |S_{21}|^2 = \frac{4g_1 g_2}{(g_1 + g_2 + 1)^2 + 4{Q_0}^2 \left(\frac{\omega - \omega_0}{\omega} \right)^2} = P(f) \tag{3.24}$$

where g_1 and g_2 are the coupling coefficients of each port and are defined as:

$$g_1 = \frac{\omega_0 {m_1}^2 Q_0}{L}, \qquad g_2 = \frac{\omega_0 {m_2}^2 Q_0}{L} \tag{3.25}$$

By writing:

$$P_0 = \left(\frac{2g}{1+2g}\right)^2 \quad \textit{and} \quad Q_L = Q_0(1-\sqrt{P_0}) \tag{3.26}$$

The S_{21} parameter can be related to both the loaded quality factor (Q_L) and the peak power (P_0) in one equation.

$$|S_{21}|^2 = P(f) = \frac{P_0}{1+4{Q_L}^2\left(\frac{f-f_0}{f_0}\right)^2} \tag{3.27}$$

The S_{11} and S_{21} parameters can be directly measured and plotted using a Vector Network Analyser (as shown in figs 2.9 and 2.10 respectively, these show the S-parameters plotted in the frequency domain). The S_{11} (fig 2.9) is also known as the voltage reflection coefficient and denotes the strength of the coupling (at the resonant frequency) with the system by comparing the input and output. The largest dip possible is desired when exciting samples as this will result in the highest transfer of power. The aim is to attain $|S_{11}|$ -> -∞ at resonance, having the cavity and sample impedance matched to the source circuit.

The aim is to attain an S_{11} measurement for the cavity at resonance of between -20 to -40dB when adding a sample. In this way we can be certain we are transferring the most power possible into our sample. This measurement is also useful when there is only 1 port into our cavity, which is used to tune the coupling loop prior to excitation of a sample.

S_{21} measurement, or voltage transmission coefficient, measures the ratio between the magnitudes of the output and input voltage. For example, there is an explected decrease in S_{21} value with a sample added compared to an empty cavity as the sample will absorb some of the input power.

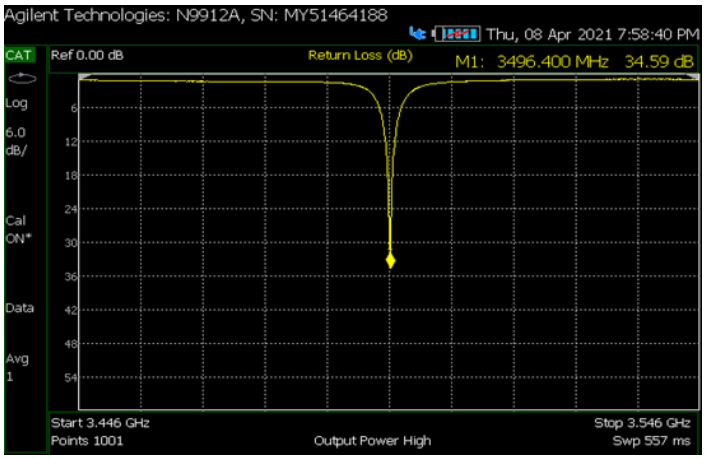

Fig. 3.9 Plot showing S_{11} magnitude in the frequency domain for an empty TM_{010} Cylindrical Cavity. The power dissipation occurs in the metal walls of the cavity, the surface currents that are induce to create the standing electric field cause slight heating, which is then dissipated through the bulk material.

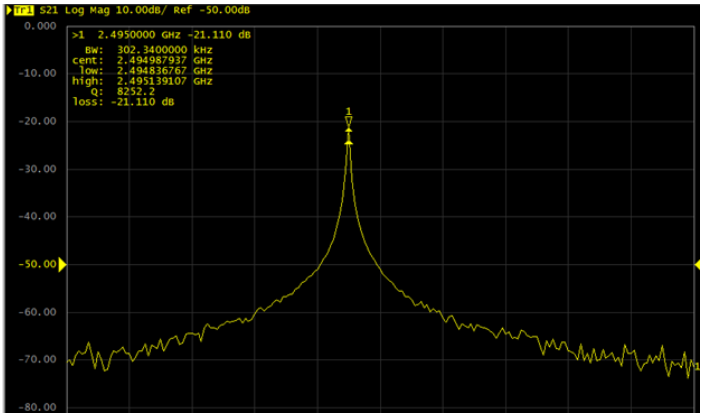

Fig. 3.10 S_{21} measurement for our TM_{010} empty cavity, the 3dB bandwidth values are the differences in the "low" and "high" values in the plot and are shown by the markers just below the maximum value. The Q factor is listed and is the resonant frequency divided by the 3dB bandwidth. The S21 was obtained using two SMA connectors with small loops attached from the inner to outer connector, these were inserted into the cavity through small holes placed diametrically opposite each other either side of the cavity.

3.3 Increasing Sample Volume

In previous experiments, the sample used had a volume of around 200μl. This is problematic for real world application as a standard sputum sample from a patient has a volume of approximately 5-10ml. When taking a 200μl sample from the whole, there is no guarantee that the part taken will contain any pathogen bacteria. Testing this would then yield a negative result, where it should really yield a positive one.

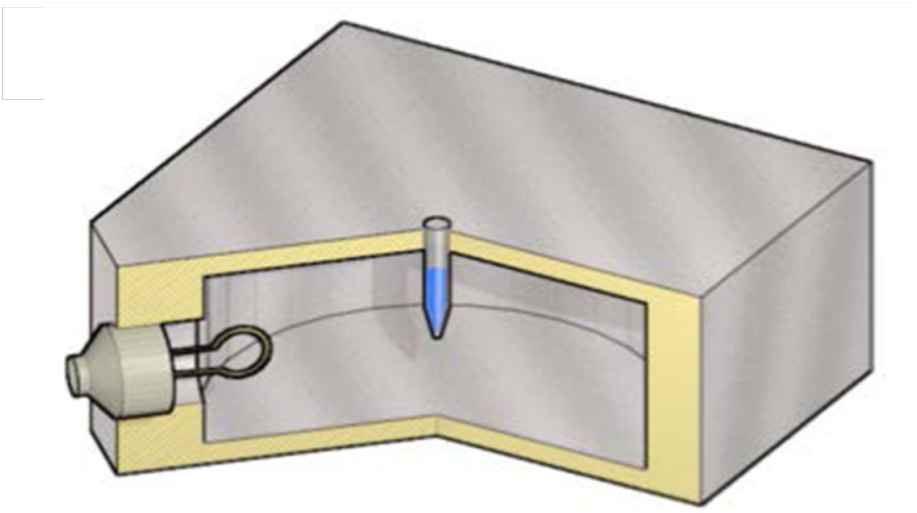

Fig. 3.11 Sample in Eppendorf Tube placed through hole in cavity [160]

Taking multiple 200μl samples would be impractical as with a 10ml sputum sample the process would need to be done 50 times. It is therefore imperative that the volume of sample inside the cavity is increased, if possible, to encompass the entire volume of sputum sample. Another problem with the current setup is the fact that a 10 second exposure using the current power level is sufficient to boil the sample. Whilst this demonstrates an excellent efficiency of energy transfer it is detrimental to our aim. To bind to the magnetic nanoparticles, the DNA needs to be single stranded. This means a medium needs to be found in which the largest amount of double stranded DNA is broken down, but the single stranded DNA is kept. If the heating effect is too rapid, then it is more difficult to maximise this outcome as a

balance between DNA released and DNA denatured (not usable) would occur in a shorter window of time. This is not necessarily a problem, as using a larger sample size will decrease the temperature change during exposure and, if the temperature change becomes too low to promote any DNA release, the exposure time can easily be increased to counter this.

3.3.1 Modelling Electric field inside eppendorf tube excitation method using COMSOL

To increase the volume of the sample inside the cavity it is important to first understand how the sample interacts with the electric field. In previous experiments, the sample was placed in a 200µl Eppendorf tube (shown in the centre of the cavity in fig 3.11), this holds the sample in a long thin geometry which sits within the high e-field portion of the cavity. It is inserted through a small hole into the top of the cavity (this hole has very little effect on the losses of the cavity as the diameter of the hole is much less than the wavelength of the microwave, so microwaves get reflected back into the cavity)[23].

The sample is made to be long and thin so that the electric field can permeate without being reduced by the effects of depolarisation. COMSOL multi-physics is a finite element modelling software that can be used to simulate (among many other things) electric and magnetic field distributions within a system. When simulating microwave cavities, the software gives a field distribution and resonant frequency based on the geometry of the cavity. As no power is being transferred into the cavity there is no set value for the electric field, however, the software creates a normalised value which can be used to measure the change when items are added. All simulations were created using COMSOL v5.0.

Fig 3.12a shows a cross section of the electric field inside the cavity when empty, whereas fig 3.12b also shows a long thin sample (in this case simulated as water, $\varepsilon_r = 80$). In both cases the cavities are simulated as being filled with air. By taking the maximum values of electric field for both simulations (440V/m and 436V/m respectively) it can be seen that

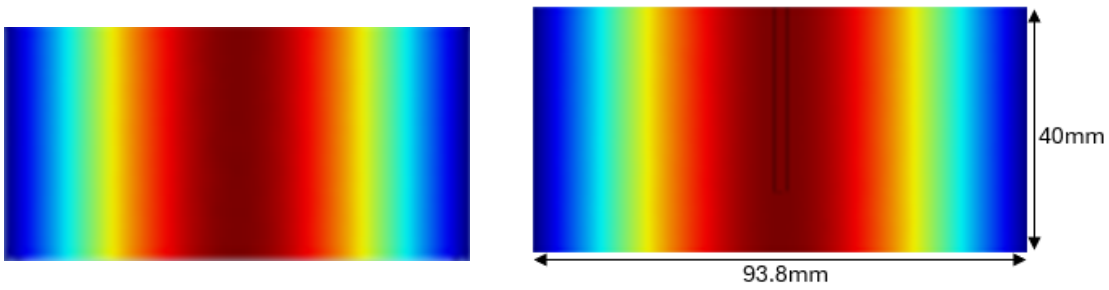

Fig. 3.12 Comparison of Electric field distributions in an empty (left) and eppendorf loaded cartridge (right) TM_{010} cylindrical cavity simulated in COMSOL Multi-physics (the cross-section is situated along the vertical axis of fig 3.11)

the long thin sample has an almost negligible effect on the internal field. The length of the sample is limited by the height of the cavity (which is 4cm). To increase the sample size, the width or radius (assuming a cylindrical shape) of our sample must be increased. Unfortunately, by simulating a thicker sample using COMSOL it is clear that this will not work practically.

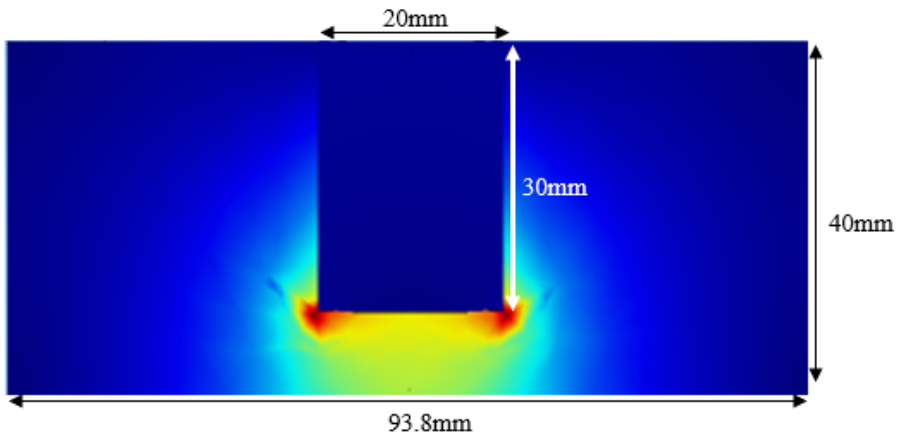

Fig. 3.13 COMSOL simulation of a 10ml Cylindrical sample inside TM_{010} cylindrical cavity resonating at 2.45GHz. The sample holder is modelled as a thin-walled plastic tube of height and diameter 30mm and 20mm respectively

Here it can seen that the electric field distribution no longer follows the same pattern as before. The electric field within the sample was simulated to be 13V/m, which shows a substantial reduction from 440V/m and demonstrates that the majority of the electric field will not permeate the sample, meaning it will have no heating effect. In order to increase the electric field within the larger sample, the principle of aligning the electric field to a sample geometry held perpendicular to the direction of the electric field is explored.

3.3.2 Depolarization

Understanding how different bodies act within an electric field is essential when designing a suitable sample geometry.

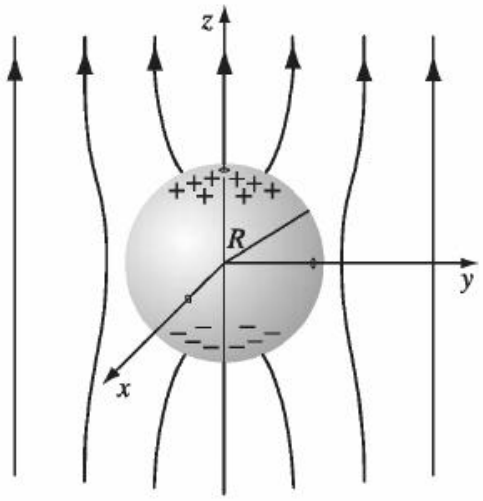

Fig. 3.14 This diagram shows the displacement of electrons and the change in a static electric field distribution of a metallic sphere introduced into a uniform electric field. This displacement also occurs in the bound charges found in an ideal dielectric, however, the resulting internal electric field reduction is not as great as the electrons are not free. The results are subtly different for an AC field but this analysis is sufficient for design purposes.

Any electric field applied to materials that are metallic (with free electrons within their structure) or materials made from molecules with a net dipole moment (such as water) will cause an alignment of the charge with the electric field and creation of polarised regions within the material.

Using the example of a metallic sphere introduced into a uniform electric field (fig 3.15) it can be seen that the free electrons inside the metallic material move respective to the electric field and create a positive region with the direction of the electric field and a negative region in the opposite direction of the electric field. As there are now two areas of opposite charge, this creates an electric field in the opposite direction to the applied field which reduces the net field inside the sphere. Inside metals this reduction is complete so the net field inside a metallic material will be zero.

If the material the of the sphere is polar (water, for example) the electric field reduction still takes place as the polar molecules align and cause an opposite electric field, however, this reduction is not complete so there will be a net electric field (still in the direction of the applied electric field) within the material. As shown previously in fig 3.13, the geometry of the sample applied has a great impact on how the depolarization affects the internal electric field, linked to the extent of the sample surfaces perpendicular to the field.

For this problem, it is possible to obtain a general solution using Laplace's Equation ($\nabla^2\Phi = 0$, where Φ is the (quasi)static electric potential, the gradient of which is -E).

Using the model shown in fig. 3.15 as a simple starting point. In this model, E_0 denotes the magnitude of the electric field applied; θ denotes the angle from the normal to the electric field; and a denotes the radius of the sphere. Creating equations for the electric flux inside and outside the sphere, based on linear contributions of potential functions, each of which can be solved using Laplace's equation.

$$For\ r < a\,(inside\ the\ sphere), \qquad \Phi = -E_1 r cos\theta \tag{3.28}$$

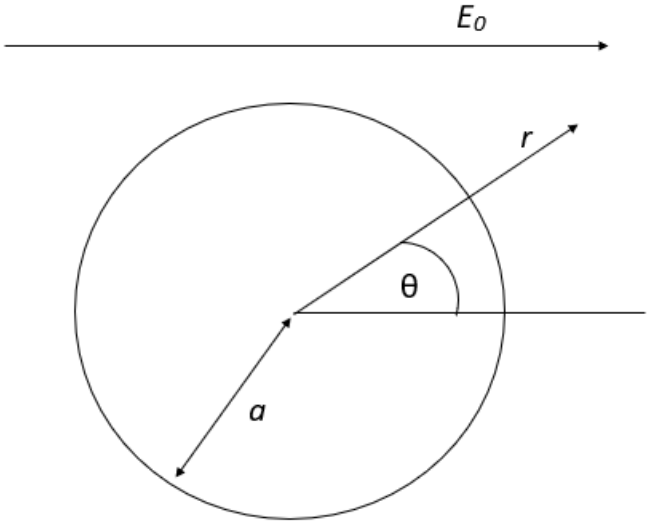

Fig. 3.15 Simple Diagram of the polar coordinate geometry used to solve Laplace's equation in spherical or cylindrical geometries.

$$For\ r \geq a\ (outside\ the\ sphere), \qquad \Phi = -E_0 r cos\theta + \frac{p}{4\pi\varepsilon_0 r^2} cos\theta \tag{3.29}$$

where:

- p is the dipole moment of the sphere
- E_1 is the electric field within the sphere

The solutions to Laplace's equation are unique, meaning that if these assumed forms fit the boundary conditions then they are the only correct solutions.

For the sake of ease, A can be used in place of $\frac{p}{4\pi\varepsilon_0}$.

These equations can then be used to calculate the field components of the system.

- E_r and E_θ denoting the parallel and perpendicular components of the electric field.
- D_r and D_θ denoting the parallel and perpendicular components of the electric flux density.

At boundaries between materials, both D_r and E_θ are continuous.

These values are related by the equation:

$$\underline{D} = \varepsilon_r \varepsilon_0 \underline{E} \tag{3.30}$$

Since: $\underline{E} = -\underline{\nabla}\Phi$,

$$E_r = -\frac{\partial \Phi}{\partial r} \qquad E_\theta = -\frac{1}{r}\frac{\partial \Phi}{\partial \theta} \tag{3.31}$$

$$D_r = -\varepsilon_r \varepsilon_0 \frac{\partial \Phi}{\partial r} \qquad D_\theta = -\varepsilon_r \varepsilon_0 \frac{1}{r}\frac{\partial \Phi}{\partial \theta} \tag{3.32}$$

An equation for E_θ at the sphere's surface both outside and inside the sphere can be calculated by simply substituting equations 3.33 and 3.34 respectively.

$$Inside \qquad E_\theta = -E_1 sin\theta \tag{3.33}$$

$$Outside \qquad E_\theta = -E_0 sin\theta + \frac{A}{a^3} sin\theta \tag{3.34}$$

As E_θ is continuous at the boundary, these equations can be equated to yield:

$$-E_1 = -E_0 + \frac{A}{a^3} \tag{3.35}$$

As D_r is also continuous at the boundary, the equation for the electric flux density outside and inside the sphere can be defined, equated, and calculated.

$$Inside \qquad D_r = \varepsilon_{r_{in}} \varepsilon_0 E_1 cos\theta \tag{3.36}$$

$$Outside \qquad D_r = \varepsilon_{r_{out}} \varepsilon_0 E_0 cos\theta + \varepsilon_{r_{out}} \varepsilon_0 \frac{2A}{a^3} cos\theta \tag{3.37}$$

Giving:

$$\frac{\varepsilon_{r_{in}}}{\varepsilon_{r_{out}}}E_1 = E_0 + \frac{2A}{a^3} \tag{3.38}$$

By considering a subtraction of the simultaneous equations 3.35 and 3.38 ((3.35)-2x(3.38)). It is possible to obtain an equation linking E_0 and E_1:

$$E_1 = \frac{3E_0}{\frac{\varepsilon_{r_{in}}}{\varepsilon_{r_{out}}} + 2} \tag{3.39}$$

The ratio between the relative permittivity of each material is key in this equation. Consider a water droplet in air, then the electric field within the droplet drops to just 3.7% of the external field (assuming ε_r for water is 80 and ε_r for air is 1).

The dipole moment of the material can also be calculated from this model.

Equation 3.38 can be rearranged to yield,

$$\frac{2A}{a^3} = \frac{\varepsilon_{r_{in}}}{\varepsilon_{r_{out}}}E_1 - E_0 \tag{3.40}$$

Then substituting the result from 3.39,

$$\frac{2A}{a^3} = \frac{\varepsilon_{r_{in}}}{\varepsilon_{r_{out}}}\left(\frac{3E_0}{\frac{\varepsilon_{r_{in}}}{\varepsilon_{r_{out}}} + 2}\right) - E_0 \tag{3.41}$$

Which can be rearranged and reduced to:

$$\frac{2A}{a^3} = E_0\left(\frac{2\frac{\varepsilon_{r_{in}}}{\varepsilon_{r_{out}}} - 2}{\frac{\varepsilon_{r_{in}}}{\varepsilon_{r_{out}}} + 2}\right) \tag{3.42}$$

Reinserting $A = \frac{p}{4\pi\varepsilon_0}$ and rearranging for p yields:

$$p = 4\pi\varepsilon_0\left(\frac{\frac{\varepsilon_{r_{in}}}{\varepsilon_{r_{out}}} - 1}{\frac{\varepsilon_{r_{in}}}{\varepsilon_{r_{out}}} + 2}\right)E_0 a^3 \tag{3.43}$$

This equation can be simplified further as $\frac{4}{3}\pi a^3$ relates to the volume of the sphere (V_s):

$$p = 3\varepsilon_0 \left(\frac{\frac{\varepsilon_{r_{in}}}{\varepsilon_{r_{out}}} - 1}{\frac{\varepsilon_{r_{in}}}{\varepsilon_{r_{out}}} + 2} \right) E_0 V_s \tag{3.44}$$

3.3.3 Frequency Change

It is important to note that the addition of a lossy sample (e.g. water) into the cavity will cause a drop in frequency.

Using the geometry shown in fig 3.16, but this time assuming the sphere material is dielectric, the relationship between the applied electric field (E_0) and the internal electric field in the sample (E_1) can be written as:

$$E_1 = \frac{E_0}{1 + N(\varepsilon - 1)} \tag{3.45}$$

where $\varepsilon = \varepsilon_1 - j\varepsilon_2$ i.e. the complex permittivity of the sample material and for a sphere, N = $\frac{1}{3}$

The change in frequency is related to the change in stored electrical energy (U_e) of the cavity.

$$f_0 = \frac{1}{2\pi} \frac{1}{\sqrt{LC}} \rightarrow \frac{\Delta f}{f_0} \approx -\frac{1}{2} \frac{\Delta C}{C} \approx -\frac{1}{2} \frac{\Delta U_e}{U_e} \tag{3.46}$$

It can assumed that the magnetic field energy does not change if the sample is placed in the anti node of the electric field (as the magnetic field is 0). By maintaining a constant applied electric field (E_0), it can assumed that the electrical energy is proportional to the equivalent capacitance.

By assuming that the total stored electrical energy U_e is unaltered to first order so can be computed straightforwardly from the electric field distribution in the empty resonator. However, the small change in electric energy ΔU_e is not so straightforward to calculate since the modified field energy must be included within both the volume of the sample and in the

space around it. There is a net concentration of field energy at the "poles" of the sample, which is most extreme for a metal sample, and this concentration means that ΔU_e is always positive and so $\Delta f < 0$ (i.e. the frequency always reduces). This can be greatly simplified by considering the electric dipole moment p induced in the sample. Assuming that E_1 is uniform (i.e. uniform polarisation within the sample, with only surface - not volume - polarisation charges), it can be shown that:

$$p \approx (\varepsilon - 1)\varepsilon_0 E_1 V_s \approx \frac{\varepsilon - 1}{1 + N(\varepsilon - 1)}\varepsilon_0 E_0 V_s \tag{3.47}$$

The electric energy of an induced dipole (where $p \propto E_0$) is $\Delta U_e = +\frac{1}{2} pE_0$ and this results neatly captures all the changes in electric energy density associated with the sample, both inside it and out. It is evident from Eqn.(3.47) that in a lossy dielectric sample there is a phase difference between p and the applied field E_0 , which means that some of the dipole energy will be stored (linked to the in-phase, i.e. real part, of the product pE_0) and some dissipated (linked to the out-of-phase, i.e. imaginary, part of pE_0). Substituting this result in Eqn.(3.46) and taking peak field values gives:

$$\frac{\Delta f}{f_0} \approx -\frac{1}{2}\frac{\Delta U_e}{U_e} \approx -\frac{Re(pE_0)}{4U_e}, U_e \approx \frac{1}{2}\varepsilon_0 \int_V E^2\, dV \approx \frac{1}{2}\varepsilon_0 {E_0}^2 V_m \tag{3.48}$$

Defining the mode volume as V_m.

Combining Eqns. (3.47) and (3.48) leads to the final result for the fractional frequency shift:

$$\frac{\Delta f}{f_0} \approx -\frac{1}{2}\frac{\Delta U_e}{U_e} \approx -\frac{Re(pE_0)}{4U_e} \approx -\mathrm{Re}\left(\frac{\varepsilon - 1}{1 + N(\varepsilon - 1)}\right)\frac{V_s}{2V_m} \tag{3.49}$$

This phenomenon has been visible in previous work as the sample size used ($\leq 250\mu l$) only leads to a frequency drop of around 100MHz which, when working with a cavity operating at 2.5GHz, is fairly insignificant. When increasing the volume of sample to 10ml the frequency drop this causes will be substantially higher and will need to be compensated

for so the operating frequency remains within the bandwidth of the microwave applicator device.

3.3.4 Sample Orientation respective to Electric Field

For the current sample geometry used, the electric field is induced as such:

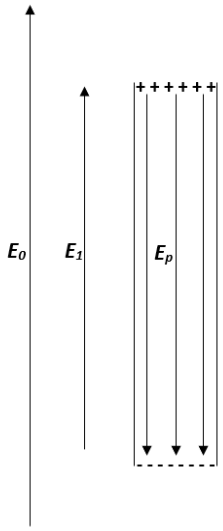

Fig. 3.16 This diagram shows the electric field within a long thin sample parallel to the direction of the field.

Where:

- E_0 is the electric field in the cavity
- E_p is the electric field created by the movement of water molecules
- E_1 is the resultant electric field inside the water sample

The sample in this orientation works slightly differently to the parallel sample. The molecules of water in a sample work to counter the cavity field. As water is a dielectric and not a metal the electric field the molecules produce is not as large as the surrounding field, so it does not fully cancel it out.

For this orientation:

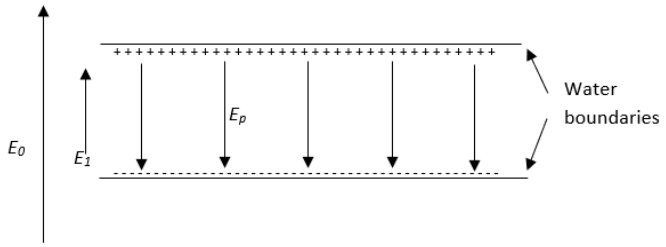

Fig. 3.17 This diagram shows the electric field within a long thin sample perpendicular to the direction of the field.

$$E_1 = E_0 - E_p > 0, \quad E_1 < E_p \tag{3.50}$$

The volume of sample can then be increased by stacking multiple thin tubes on top of each other within the cavity.

3.4 Sample Cartridge Design and Experimentation

To test this, a cartridge was created to hold multiple Eppendorf tubes. The cartridge needed to be made of a material with a low permittivity and loss tangent to reduce the amount of power it absorbs. In order to reduce this further it needs to contain as little material as possible while being able to hold the Eppendorf tubes close to the centre of the cavity (i.e. the maximum electric field). As such, a cartridge was made out of a plastic called PTFE as it has a low permittivity constant ($\varepsilon_r = 2$) which will minimise the amount of electric field taken up by the cartridge. It is also cheap and easy to mill. The small cylindrical part on top fits into the small hole at the top of the cavity that was used to add samples. This holds the cartridge in place whilst the cavity is closed.

The cartridge, designed and fabricated at Cardiff University, holds 10 Eppendorf tubes with 250μl each, totaling 2.5ml.

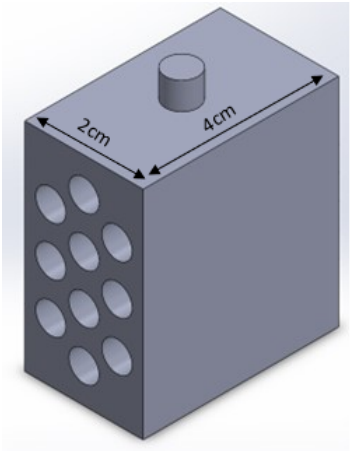

Fig. 3.18 PTFE cartridge with a maximum volume of 2.5ml, the diameter of the holes was matched to the Eppendorf tubes at 6mm, these pass completely through the cartridge

In order to measure the efficiency of this system, the relationship of an empty and sample loaded cavity Q-factors was compared. The empty cavity has an inherent Q-factor which relates to its inherent material losses. The sample can be seen as an additional source of loss (even though this loss is a desired effect) and so the Q-factor value will decrease when the sample is added. The ratio of empty cavity Q-factor to cavity with sample Q-factor is related to the efficiency of power delivered into the cavity and power delivered into the sample with the following equation.

$$P_s = P_0 \left(1 - \frac{Q_s}{Q_0}\right) \tag{3.51}$$

Where:

- P_s is the power delivered into the sample
- P_0 is the power delivered into the cavity
- Q_s is the Q-factor of the cavity with sample

- Q_0 is the Q-factor of the empty cavity

The efficiency (η) of power delivery to the sample can then be calculated as:

$$\eta = \frac{P_s}{P_0} = 1 - \frac{Q_s}{Q_0} \tag{3.52}$$

The Q-factor of the empty cavity is around 8000. The Q-factor of the cavity with the vertical sample (250μl) is around 100. This gives a power transfer efficiency of around 99%. Using a network analyser, the S_{21} characteristic of the cavity was measured with the cartridge and increasing volumes of sample added using water as a sample. The empty cartridge characteristic is important as it also reduces the Q-factor, showing that the cartridge absorbs part of the power entering the cavity.

3.4.1 Results and Discussion

The Q-Factor at a volume of 0μl shows the effect of the empty cartridge. The Q is reduced by about half, meaning that approximately half the power is absorbed by the cartridge. The full 2.5ml sample then reduces the Q to around 850. The power transfer into the sample can then be calculated as

$$\eta \approx \frac{4000}{8000} - \frac{850}{8000} \approx 40\% \tag{3.53}$$

Ideally this figure needs to be increased, by reducing the cartridge losses, as the method should be as low power as possible. The Q factor drops only to 850 with 2.5ml, which indicates the sample size can be increased. The frequency drop poses a problem. A major

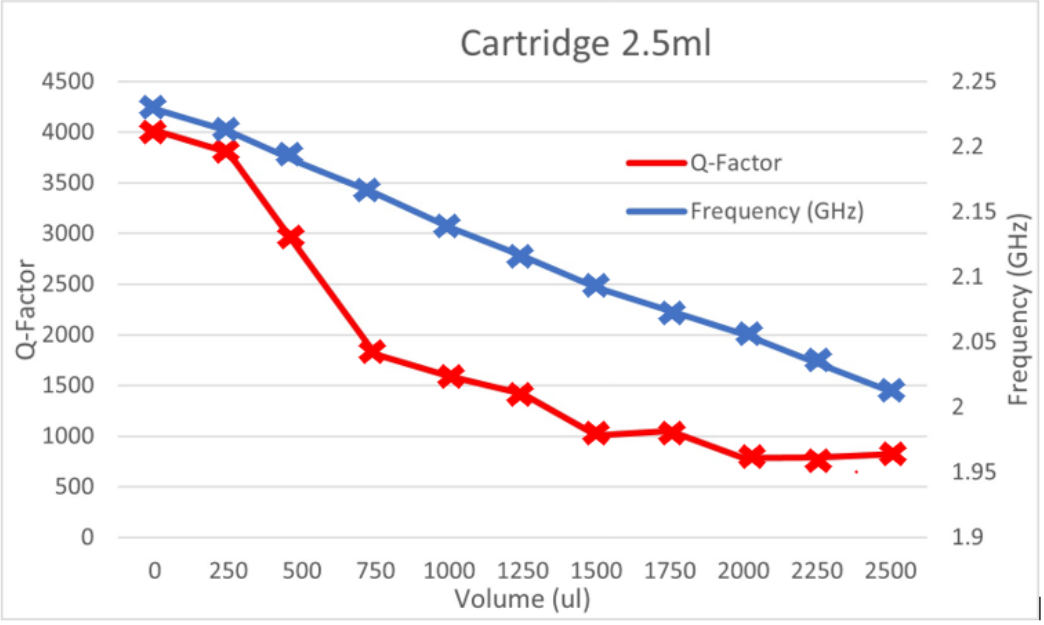

Fig. 3.19 This Graph demonstrates the relationship between the volume of the sample within the cavity shwon in fig 3.18 and the Q-Factor and frequency of the cavity. All Eppendorf tubes contained water, they were added from the top of the central line down, then filling in alternating sides to maintain as much symmetry as possible

component of the excitation system (the circulator) has a bandwidth of 2.3-2.7GHz. With the empty cartridge the coupling frequency starts at around 2.21GHz then drops to around 2GHz, meaning that the excitation system will attenuate any attempt to excite the sample. This will need to be fixed before further experimentation. The next design will work to reduce the amount of plastic in the cartridge as well as place the Eppendorf tubes closer together, so they are closer to the highest electric field density.

3.5 New Cartridge Model

A second model for the cartridge that works in a similar way but with a number of improvements. The cartridge holds a much larger volume (up to 4.5ml) with each Eppendorf tube

held much closer to the others. This allows for a larger volume in a proportionally smaller area.

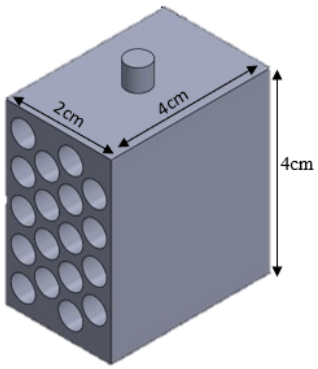

Fig. 3.20 PTFE Cartridge with a maximum volume of 4.5ml, the diameter of the holes matches the outer diameter of the Eppendorf tubes (6mm), these pass completely through the cartridge.

The new model was tested in the same fashion as the initial model.

3.5.1 Results and Discussion

The relationship between volume, change in Q-factor and frequency is very similar. However, this cartridge only absorbs around 38% of the power, which is a large improvement. The percentage of power transferred into the sample has increased to around 53%. These both indicate good progress, but there is still room for improvement. One of the main components which takes up space is the Eppendorf tubes. By eliminating those the volume close to the high electric field could increase dramatically. Our Q-factor at max volume has still not been reduced the same as the vertical sample (i.e. 100) so it is still possible to increase the volume. The problem then becomes how to create tube-like dividers in a liquid solution.

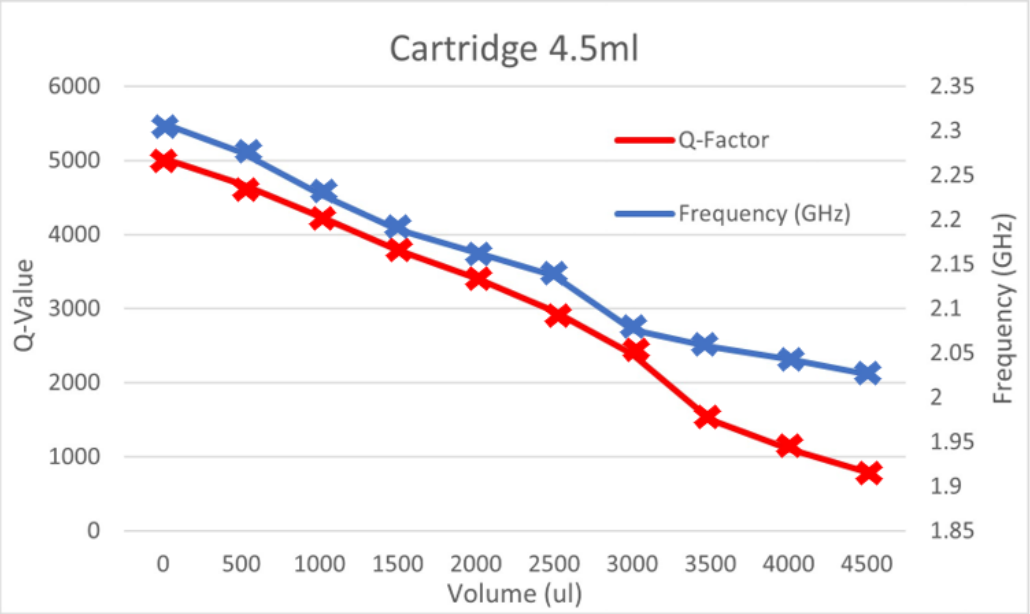

Fig. 3.21 This graph demonstrates the relationship between the volume of the sample within the cartridge shown in fig 3.20 and the Q-factor and frequency of the cavity.All Eppendorf tubes contained water, they were added from the top of the central two columns filling in diagonally down, then filling in alternating each side columns to maintain as much symmetry as possible.

3.6 Lattice Cartridge

A possible solution to this problem is to have a cuboid shaped cartridge in which the sample is deposited, then use a lid to seal the sample. This lid has a square lattice structure on it which creates the tube-like structures within the sample.

This model was simulated using COMSOL within a TM_{010} cavity at 2.2GHz. It is difficult to see the exact field values in this simulation but the relationship between the electric field in the sample and in the cavity becomes clear. By evaluating the magnitude of the electric field at a point within the plastic cartridge gives a value of around 2800 V/m and a magnitude of around 90 V/m within the sample. Comparing this to the value of maximum field for the vertical sample (around 430V/m), it can be seen that the electric field inside the

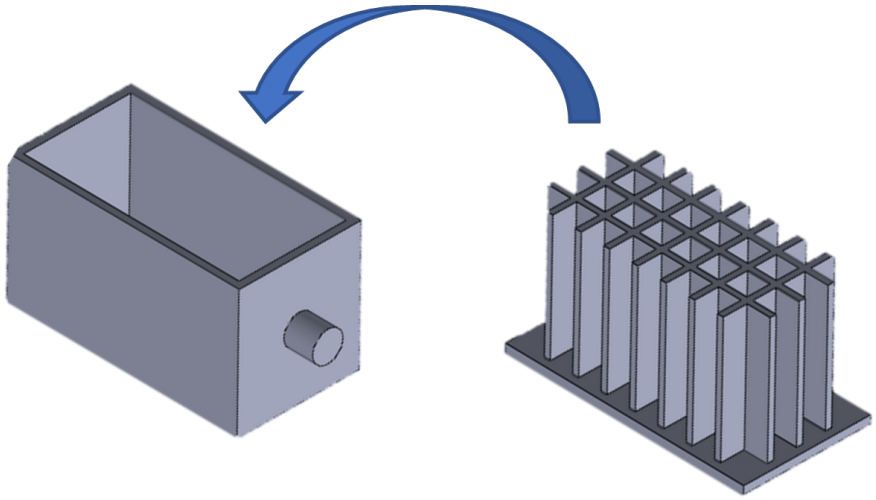

Fig. 3.22 Lattice Cartridge SolidWORKs Model

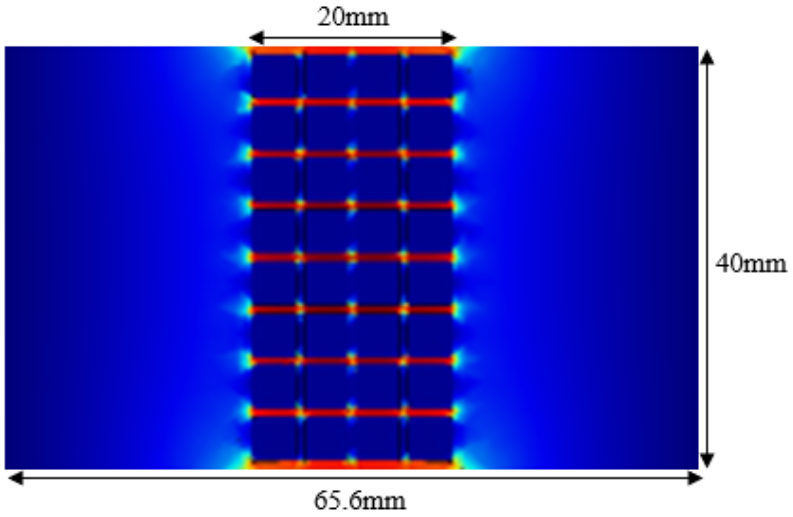

Fig. 3.23 COMSOL simulation of the Lattice cartridge within a TM_{010} cylindrical cavity resonating at 2.2GHz (3.5GHz empty cavity), the cartridge contains 10ml water

lattice sample is around 1/5th of this value. This is potentially a good thing as lower electric field will aid lowering the heating effects of the energy transfer. Another important thing to factor here is that the vertical dividers of the lattice do not seem to have an effect on the field. If these can be removed, then the cartridge would become far easier and cheaper to make. Creating square holes in plastics is a difficult task and the cartridges cannot be 3D printed as

these plastics have much higher loss tangents and would dissipate a far higher portion of the input power. By having only horizontal dividers, we can simply use a router bit to remove the unwanted plastic to the required depth. For a system which utilises a single use cartridge any ability to lower the cost is essential.

3.7 Stack Cartridge

Following from the lattice experiment, a new cartridge was designed which does not contain any vertical dividers.

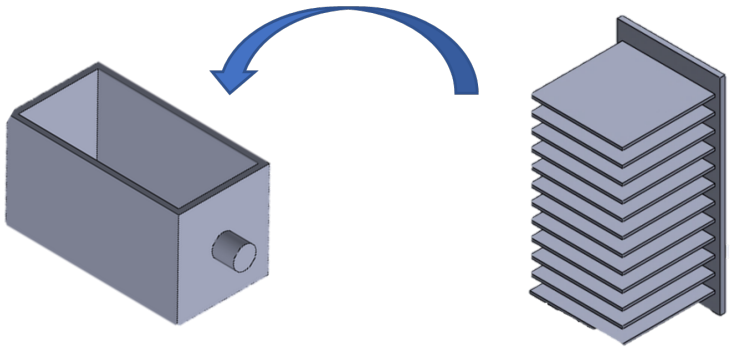

Fig. 3.24 PTFE Stack Cartridge with a maximum volume of 10ml

This consists of an outer container and a lid with 12 x 1mm horizontal protrusions to act as dividers.This gives 13 x 2mm stacks of sample. This works in the same way as the lattice in that the sample is deposited in the cartridge then the lid with dividers is pushed through the sample. Again, to test this, a COMSOL simulation of the cartridge was created to visualise the electric field densities within the cartridge. This is shown below.

The result of this model is almost identical to that of the lattice. Again, evaluating a single point within both sections (the cartridge and the sample) it is found that the magnitude of the electric field is around 2800 V/m and 90 V/m, respectively. The elimination of the vertical dividers has very little to no effect on the electric field.

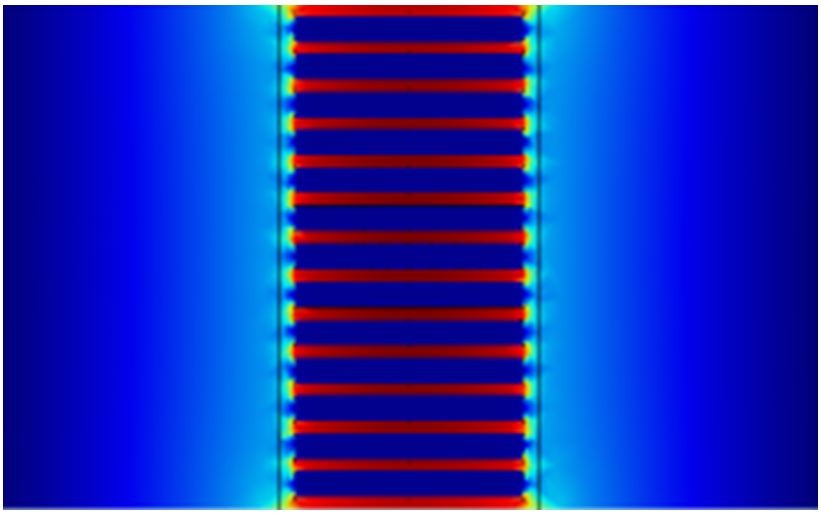

Fig. 3.25 COMSOL simulation of Stack Cartridge within TM_{010} Cylindrical Cavity

3.7.1 Electric fields in Stack Cartridge

Both experiments give a ratio of approximately 30 between the electric field in the sample and the electric field in the cartridge. This can be explained by looking at the relationship of the relative permittivity values of each material, assuming a uniform electric field perpendicular to the boundaries between each material.

where:

- E_0 is the electric field produced by the cavity

- E_s is the electric field inside the sample, which was shown earlier to be a sum of the cavity field and the depolarising effects of the water molecules

- E_a is the electric field inside the cavity

When electric fields pass perpendicular to a boundary the electric flux density is preserved not the electric field itself. For this value D is used, which can be related to the electric using the following equation.

$$D = \varepsilon_r \varepsilon_0 E \tag{3.54}$$

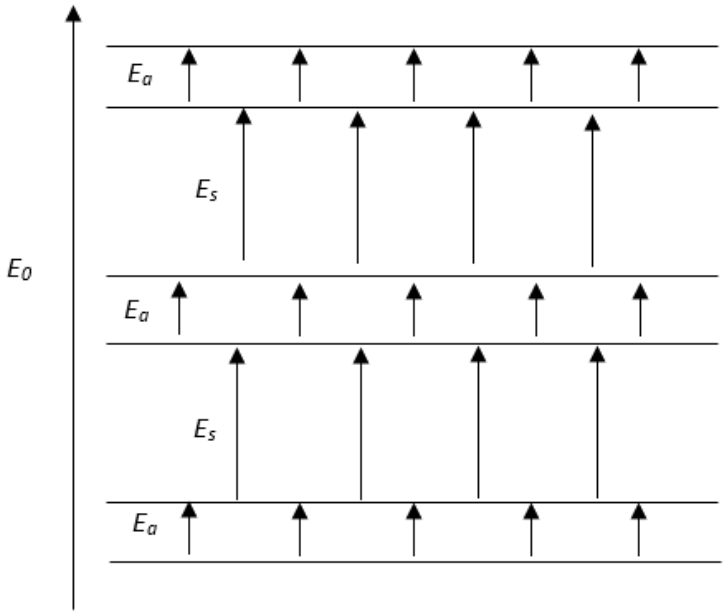

Fig. 3.26 This diagram shows the distribution of electric field when passing between perpendicular boundaries of two materials with different relative permittivity

The perpendicular component of D is preserved so the electric field multiplied by the relative permittivity is equal for both materials.

$$\varepsilon_{r_s} E_s = \varepsilon_{r_a} E_a \tag{3.55}$$

The ratio of electric field in the materials is then shown to be,

$$\frac{E_s}{E_a} = \frac{\varepsilon_{r_a} E_a}{\varepsilon_{r_s} E_s} \tag{3.56}$$

As the permittivity of PTFE plastic is given as 2 and the permittivity of water @2.5GHz is 80, we would expect to see a ratio of 40:1. The simulation predicts a 31.11:1 ratio. The

slight reduction can be explained by the inherent imperfections in the model, and by the fact that there are no boundaries of infinite extent.

This chapter has shown the design and construction of a 10ml cartridge including partitions horizontal to the E-field with data to support its use to promote microwave interaction with high volume samples. The following chapter describes the verification of this cartridge using an initial high accuracy simulation followed by the details for fabrication and in vivo testing of the cartridge using various mycobacteria.

Chapter 4

Modelling of water samples inside Stack Cartridge

The outcomes of the initial investigations of the stack cartridge model described in chapter 3 deliver a good understanding of its functionality. Further improvement on these simulations by including additional functionality and detail to the COMSOL model (as shown in fig 4.1).

4.1 Effective Sealing Method

It is of utmost importance to render the cartridge entirely waterproof during processing. Firstly, to avoid cross contamination of samples but more importantly to maintain the safety of the device operator. Microwave heating at the local level is notoriously difficult to predict so it would be entirely possible for the excitation to boil/aerosolize a small amount of the sample. If improperly contained, this could lead to widespread contamination if the cartridge were to rupture due to high pressure steam formation, for example.

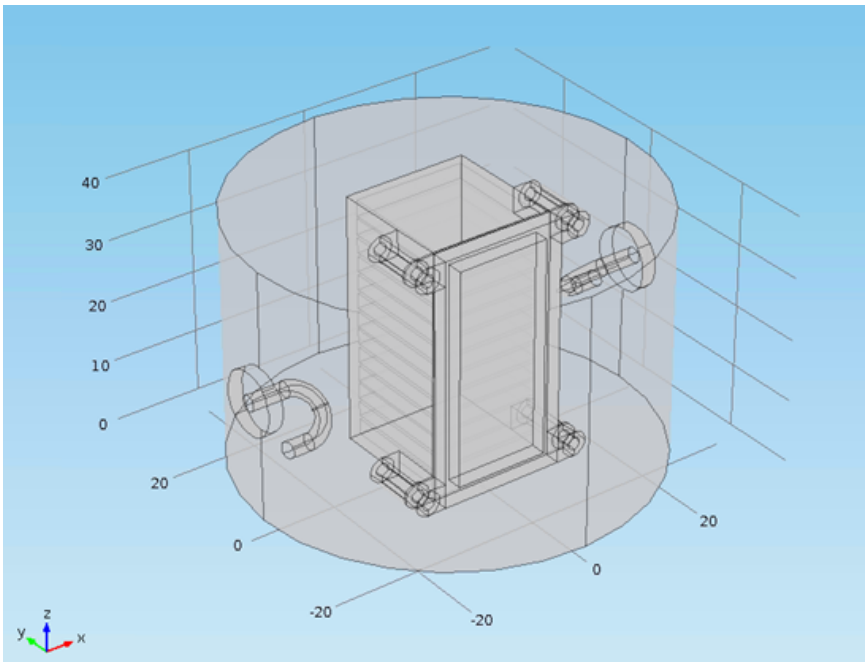

Fig. 4.1 Complete model of Stack Cartridge inside 3.5GHz TM_{010} cylindrical cavity (diameter = 65.6mm), including coupling loops. Model also shows waterproof seal and clamp with screw holes to keep the seal in place, thus giving a prototype method of keeping the cartridge waterproof. (The diagram axes are in mm)

4.1.1 Discussion

The prototype design has proved functional with water samples of 1 – 10ml in volume. The construction requires the use of 4x2mm screws to hold the clamp to the case. This requires a high degree of manual dexterity and takes up a lot of time. Additionally, the necessity for 4 separate parts, as well as the relatively high cost of the seal [156] (∼£3) makes this impractical as a cheap, rapid point of care cartridge and will certainly require improvement. At this point it is useful for proof of concept. This design has been incorporated into the COMSOL model to show its effect on the electric field (see fig 4.4).

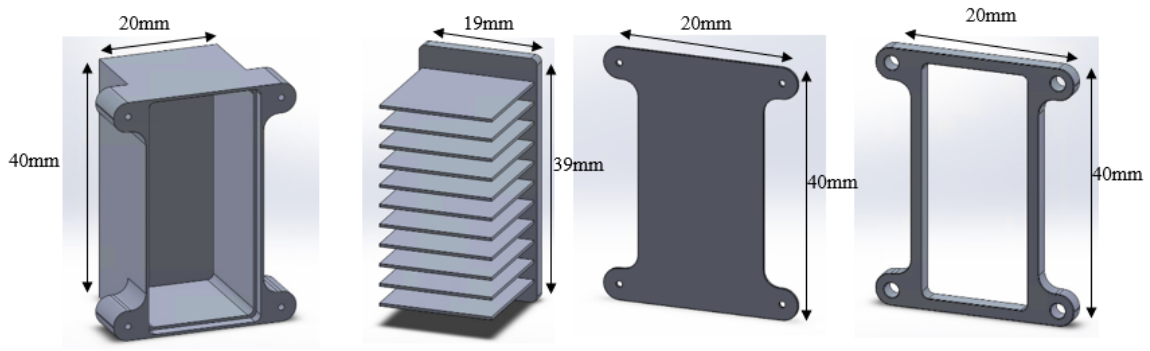

Fig. 4.2 4 Main components of Waterproofed Stack Cartridge (left to right), Case, Lid, Seal and Clamp. The clamp is held on by 4 nylon screws placing sufficient pressure on the seal to waterproof the cartridge. The Case, Lid and Clamp are made of PTFE plastic and the Seal is made of TESNIT® BA-203. The cartridge is 40mm x 20mm x 20mm. The slats on the lattice lid are 1mm thick and space 2mm apart.

4.2 Modelling Method

It is important to assess the viability of the cartridge design with various volumes of sample as the volume of sample provided would be greatly varied for real world application. As the cartridge consists of 13 even compartments for the water sample, these have been incremented from 0 and an electric field simulation has been done for each (shown in fig 4.4) with a 12W excitation at the input port. The simulation uses two steps to first gauge frequency change caused by the sample, then create electric field plots for the given frequency. Initially an Eigenfrequency simulation is calculated and the appropriate Eigenfrequency selected from those given. Following this, a Frequency Domain simulation is calculated to give the electric field. While the simulation is equipped with the potential for greater tuning (rotational and angular movement of the coupling loops), this has not yet been optimised due to the large time requirement of a parametric sweep simulation including both variables. This shall be undertaken as future work.

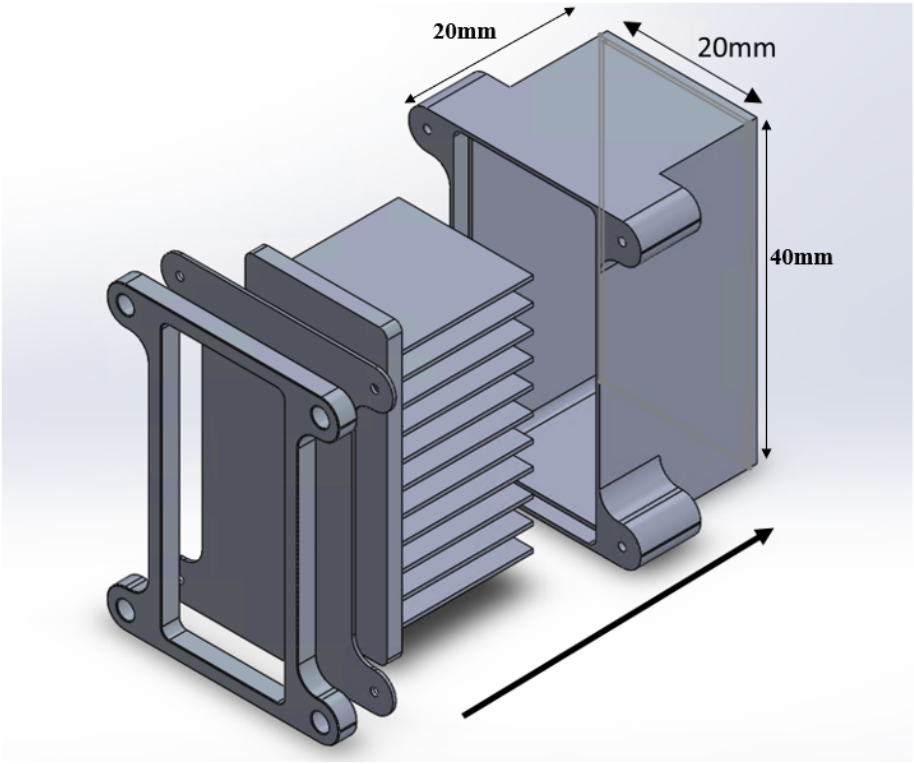

Fig. 4.3 Assembly of Waterproofed Stack Cartridge. Parts are held in place using 12mm M2 nylon screws

4.2.1 Results and Discussion

Each of the plots in fig 4.4 are colour coded to show areas of high electric field (in red) and low electric field (in blue). An upper limit of 2000V/m has been set on the electric field range to allow for accurate comparison. For each of these plots, the input port (12W excitation) is the right-hand coupling loop shown. As expected, the plots indicate that the electric field within the sample decreases as the volume increases (and begins to taper off at around 6 sections full). This is shown in Fig 4.5. Interestingly, the electric field seems to be smaller in the uppermost section in all simulations bar the full cartridge simulation. This suggests that if it is best to obtain the most uniform excitation within the sample, it would be best to fill the cartridge entirely. Otherwise, less DNA may be released from bacteria in the

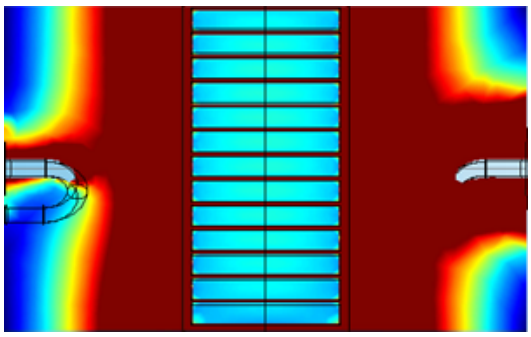

(a) Full cartridge Electric field simulation.

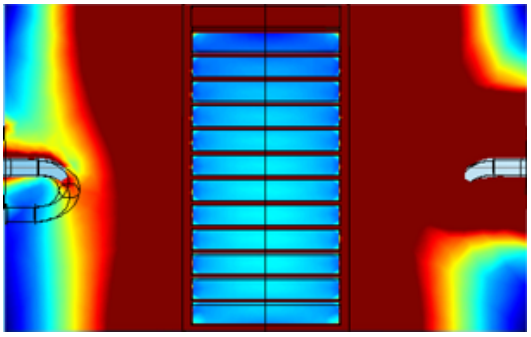

(b) 12/13 sections

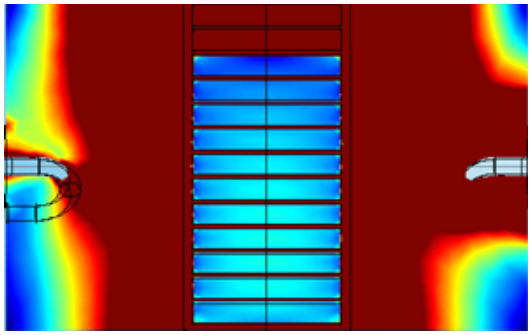

(c) 11/13 sections

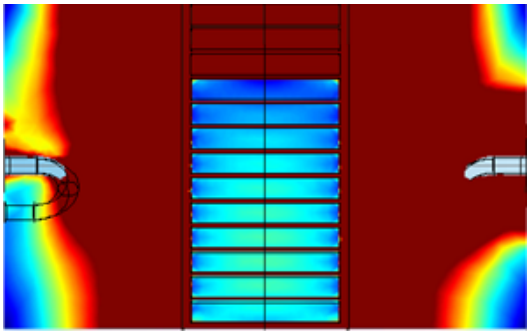

(d) 10/13 sections

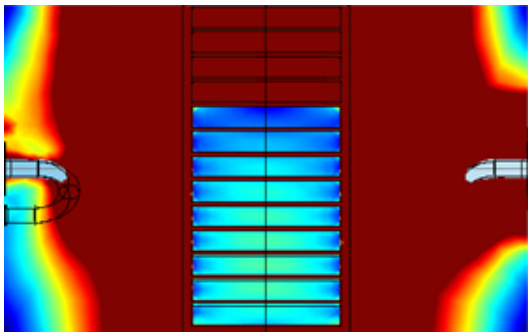

(e) 9/13 sections

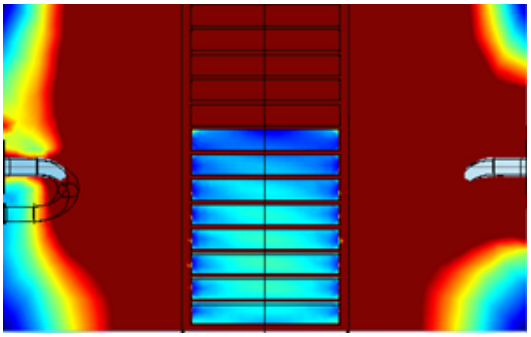

(f) 8/13 sections

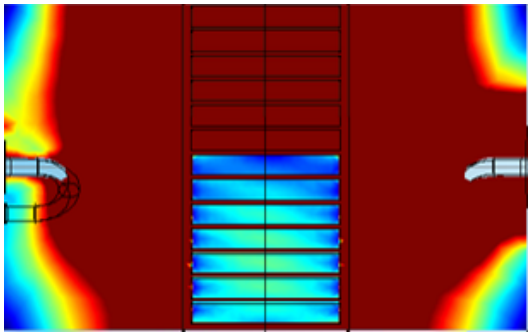

(g) 7/13 sections

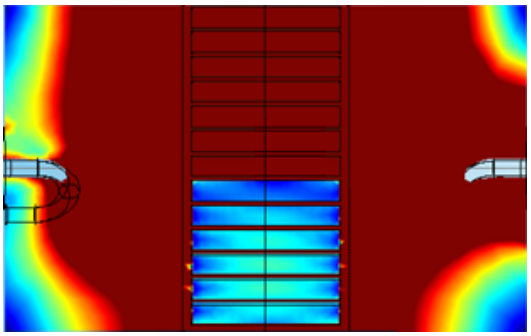

(h) 6/13 sections

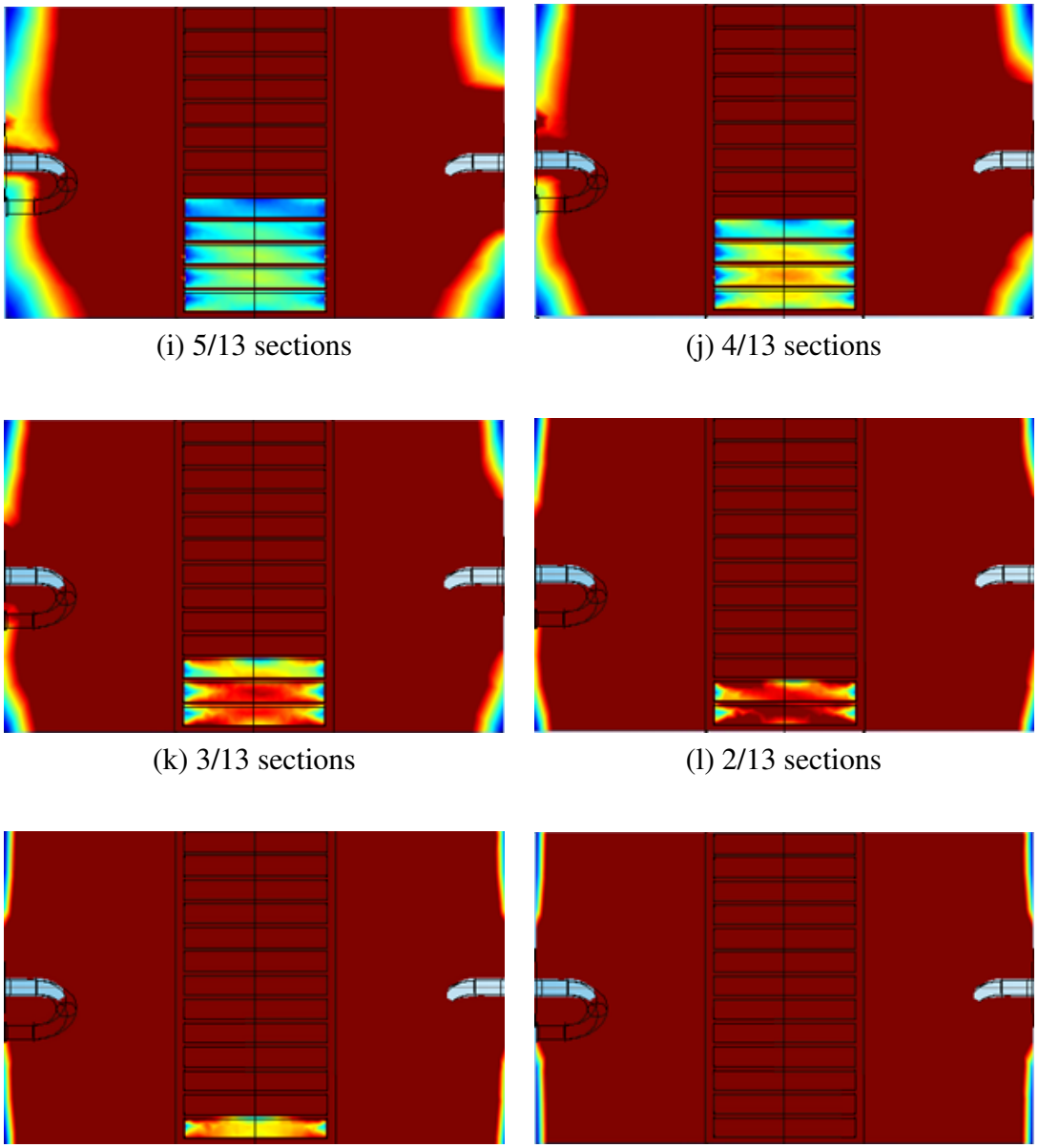

(i) 5/13 sections (j) 4/13 sections

(k) 3/13 sections (l) 2/13 sections

(m) 1/13 sections (n) Empty Cartridge

Fig. 4.4 COMSOL Simulations of varying volumes of aqueous sample inside 10ml cartridge design. The fraction denotes the number of horizontal sections filled with aqueous sample.

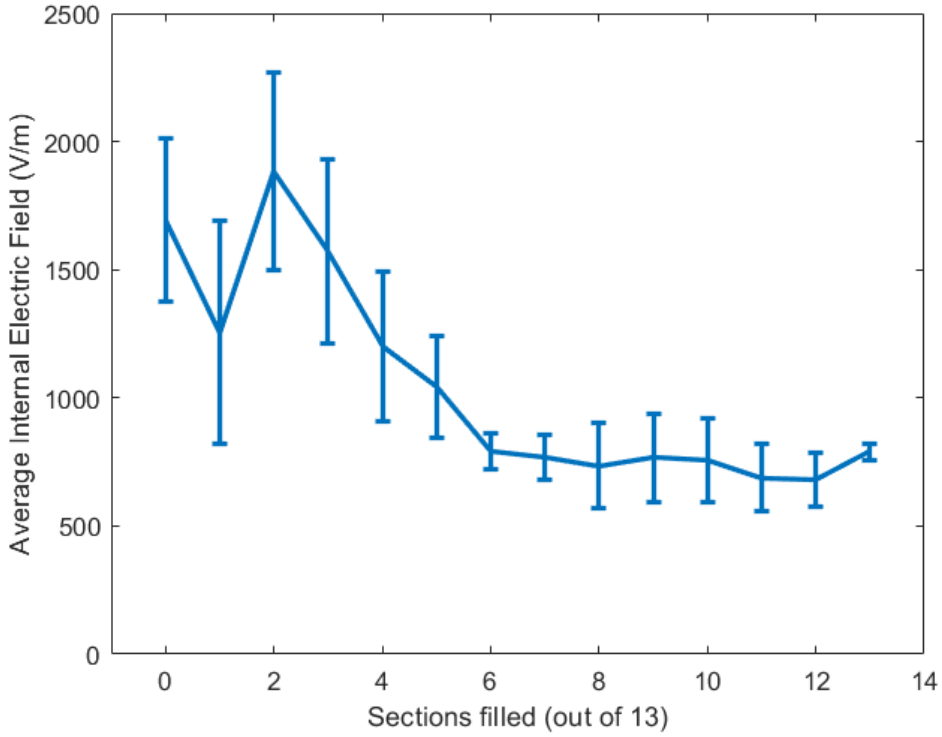

Fig. 4.5 Average internal electric field strength relative to number of cartridge sections filled with water. Error bars are 1 standard deviation away from the mean

upper section. However, the decrease in electric field is not extreme, and as this process is currently unpredictable at the individual bacterium level, it is likely that this phenomenon will cause very little noticeable effect. That being said, the addition of a buffer fluid to our sample to entirely fill the cartridge has been discussed and the sample may require the addition of mucolyse to ensure its viscosity is low enough to allow the movement of magnetic nanoparticles with relative ease. The numerical analysis of the electric field in the full cavity simulation gives a "worst case scenario" and, when compared with the numerical analysis of the electric field inside a standard 250μl Eppendorf tube, gives an idea of the difference in effectiveness of these two methods.

The electric field data in fig 4.6 is taken along the central line of the Eppendorf tube. The length 0mm corresponds to the bottom of the Eppendorf tube and lowest electric field. The

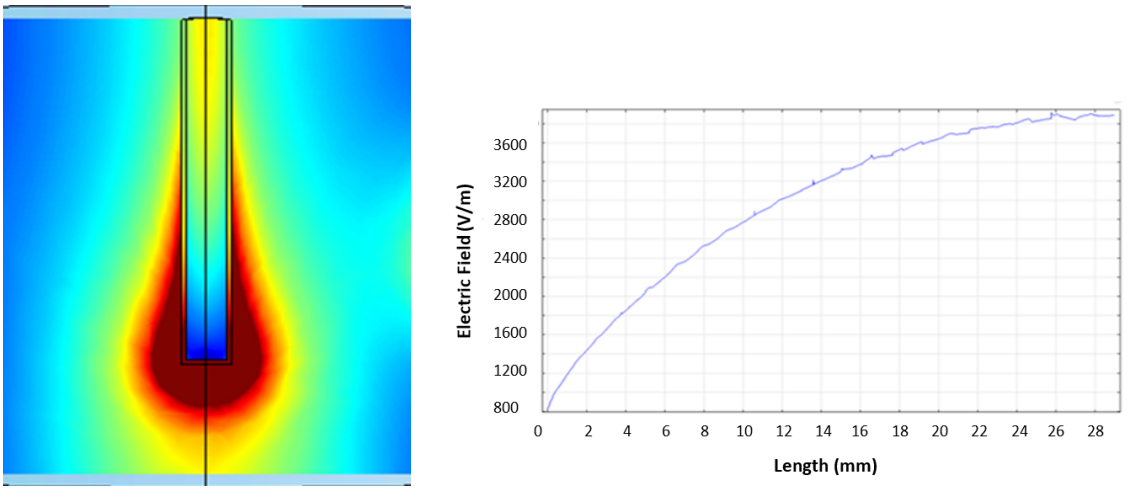

Fig. 4.6 Simulation (left) and graph (right) of electric field in aqueous sample inside eppendorf tube. The graph is taken along the central vertical line of the eppendorf with length "0" at the bottom of the inside of the eppendorf

highest electric field appears at the top of the Eppendorf tube giving a maximum value of 3800V/m. The lowest electric field is at the bottom of the tube and yields a minimum value of 800V/m. From this, 3000V/m is obtained as the maximum change in electric field (ΔE_m).

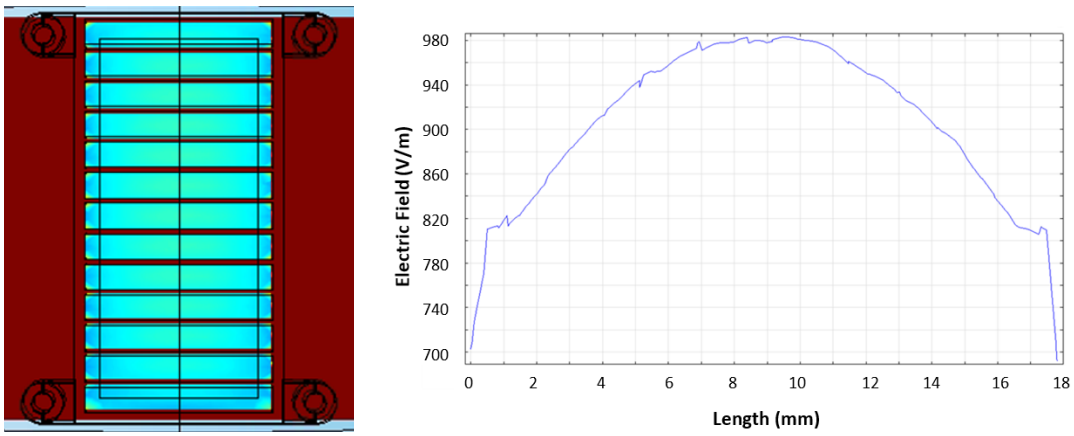

Fig. 4.7 Simulation (left) and graph (right) of electric field of aqueous sample inside 10ml cartridge. The graph is taken along the central line of the eppendorf with length "0" at the bottom of the inside of the eppendorf

The electric field data in fig 4.7 were taken along the horizontal central line of the cartridge. The variation in electric field for each of the 13 sections in the plot was minimal. The maximum electric field is this design is 980V/m and ΔE_m is 280V/m.

The implementation of this cartridge method greatly reduced the change in electric field throughout the sample allowing for a more uniform DNA release. Additionally, taking the average electric field for each sample, Eppendorf average: $\frac{3800+800}{2} = 2300Vm^{-1}$, Stack Cartridge Average: $\frac{980+700}{2} = 840Vm^{-1}$, the average field strength is shown to only be reduced by a factor of 1/3. Additionally, the value given can be compared with a numerical estimate of the internal electric field. Rearranging the following equation for rms power dissipation in the sample:

$$P_s = \pi\varepsilon_0\varepsilon_2 f_o V_s {E_s}^2 \quad \rightarrow \quad E_s = \sqrt{\frac{P_s}{\pi\varepsilon_0\varepsilon_2 f_o V_s}} \tag{4.1}$$

where:

- E_s is the average electric field strength in the sample
- P_s is the rms power input to the sample (this is a very high percentage of the excitation power $>99\%$, estimated), given as 12W
- ε_0 is the permittivity of free space, $8.854 \times 10^{-12} Fm^{-1}$
- ε_2 is the imaginary permittivity of the sample, (for water at room temperature this is around 10)
- f_0 is the resonant frequency, 2.45GHz
- V_s is the volume of the sample, 250μl

$$E_s = 1014Vm^{-1} \tag{4.2}$$

This result agrees with the COMSOL simulated electric field with 12W excitation power.

The cartridge model manufacture is limited by the technology available. The cartridge is constructed from PTFE plastic and can only be milled reliably to a thickness of 0.5mm (which is the thickness used for the slats). The use of Cyclic Olefin Copolymer (COC) [157] was also discussed as an option as it can be 3D printed with excellent performance and also has a dielectric constant ($\varepsilon_r = 2.30@1GHz$) and low loss tangent. This was decided against as it was quicker for the mechanical workshop to manufacture using PTFE. For larger batches requiring faster manufacture, the use of COC may be revisited. Preliminary simulations have shown that by using thinner slats the electric field can be further enhanced.

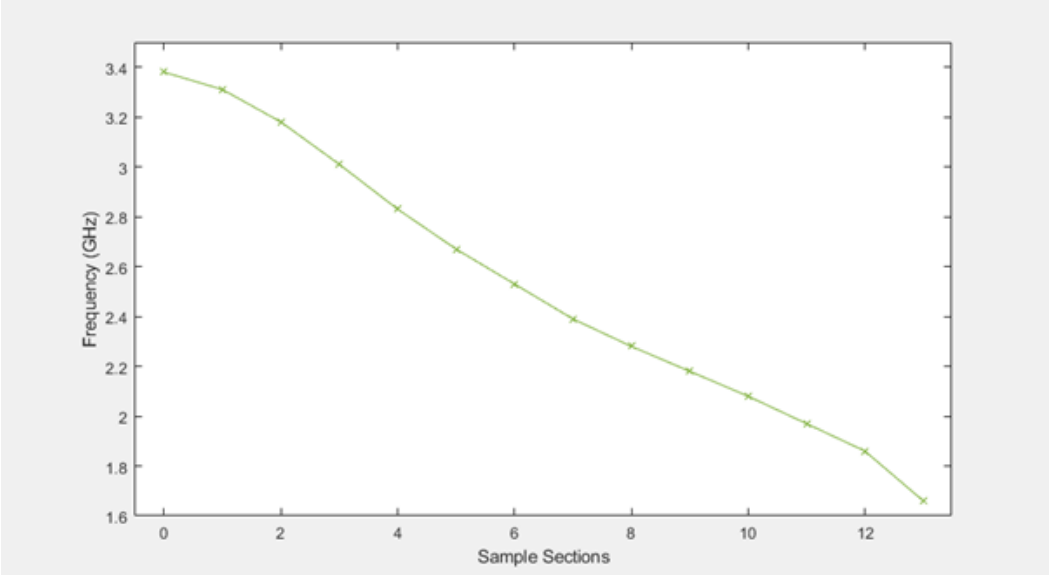

Fig. 4.8 Plot of cavity resonant frequency against increasing sample volume; the sample has been denoted as the number of full sections in the simulation. Each section is 1/13th of the total volume (10ml).

The simulations also give an estimate of the drop in frequency experienced by the sample (shown in fig 4.8). This is important to note as the current excitation system has a bandwidth of 2-4GHz. The large sample volume has a large decreasing effect (from 3.5GHz to 1.6GHz

with a full cartridge) on the frequency meaning a new excitation system will have to be built and a 3.5GHz cavity created to contain the cartridge.

4.3 Alterations to Microwave Excitation System

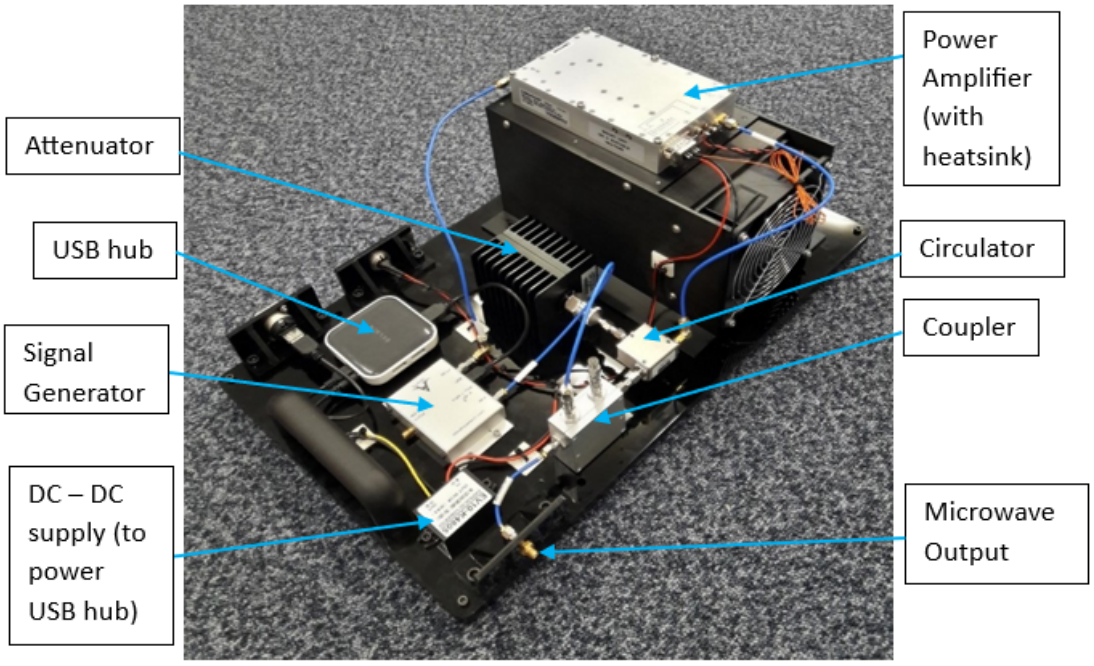

Fig. 4.9 Second Generation Microwave Excitation System (locally known as the PMA - Portable Microwave Applicator) developed for this project [163]

A new excitation system was developed that updated and refined the system first developed as part of a PhD project in 2017 [158]. It improves upon the old model by updating the components as well as the inclusion of a power sensor along with start-up protocols to enable a precise power input. The new system was also made more compact and, to a certain extent, more portable. It is designed to the same specifications as the previous system, so a few adjustments have been made based on the results of the initial experiments.

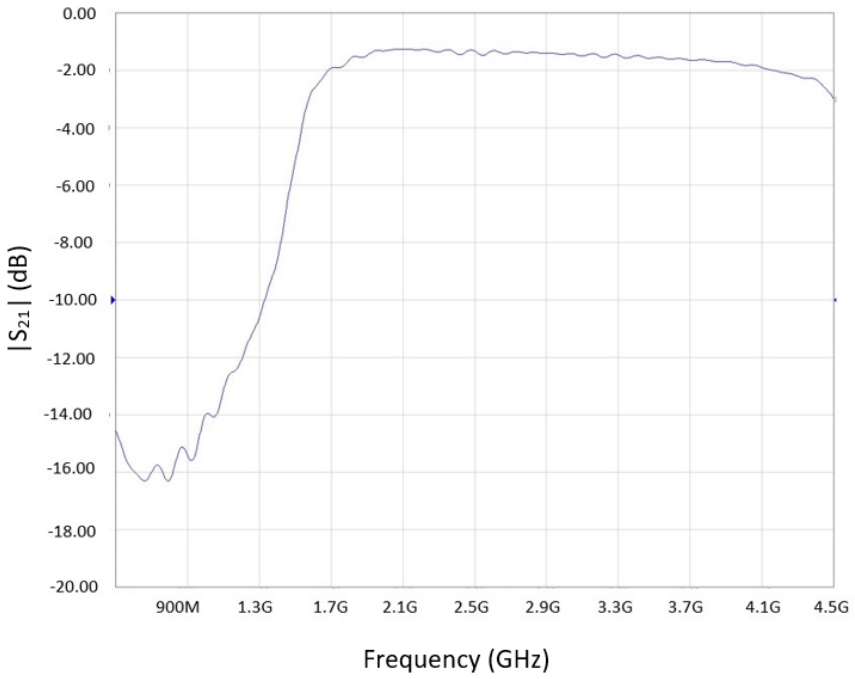

Fig. 4.10 S21 (reflected power) plot for circulator showing frequency drop off at 1.7GHz - restricting the bandwidth of the applicator

Whilst the current excitation system has been sufficient for previous studies, the use of larger volume sample causes significant problems. These are linked to the effect the sample has on the coupling frequency of the cavity. To recap, the frequency of the cavity with no sample has been designed to be around 2.5GHz. When a sample of 200µl is added the frequency is reduced only by ∼100MHz. The current excitation system has been designed to this specification. The two important parts to look at are the coupler and the circulator. The models of coupler and circulator used in this system have an inherent bandwidth of 1.7-3.2GHz and 2-4GHz, respectively, and these are the most constrictive bandwidths within the system. This means that if the coupling frequency for the loaded cavity is below 2GHz (the higher of the two minima takes precedence here) then the system will not run as the circulator will attenuate any input power. A new cavity must be designed with a higher resonant frequency such that any frequency drop remains within the bandwidth.

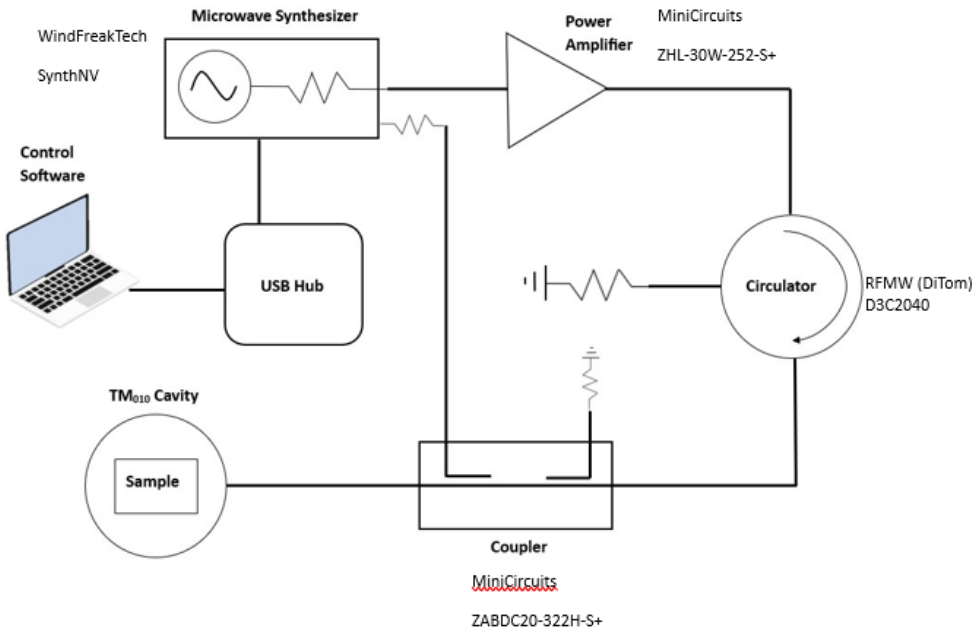

Fig. 4.11 Circuit Diagram for the Microwave Excitation System

4.3.1 Cavity Design

When designing a new cavity, the resonant frequency needs to be known. The difference in resonant frequency for an empty and full (sample added) 2.5GHz cavity is about 1GHz, so the empty resonant frequency of the new cavity must be at least 1GHz higher than the lower limit of the bandwidth. By choosing an unloaded frequency of around 3.5GHz, any frequency decreasing effects of the sample load should still fall within the bandwidth. The translation of this frequency into a physical geometry can be done by using the following equation for a TM_{010} cylindrical cavity:

$$f = 2.405\frac{c}{2\pi a} \tag{4.3}$$

A value of f = 3.5GHz gives a value of a = 3.28cm. When designing a cavity for a desired mode it is important to check that no other potential modes can interfere.

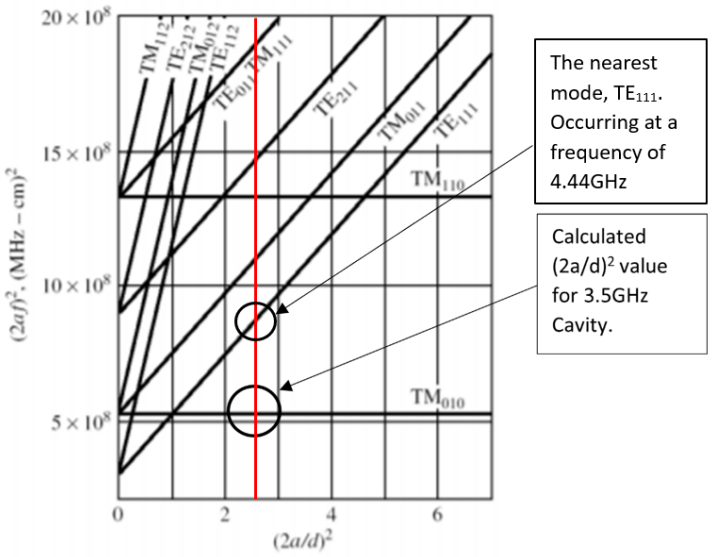

Fig. 4.12 Resonant mode chart for a cylindrical cavity [164]

Fig 4.12 [159] shows the relationship between the dimensions of the cylinder and the normalised unloaded frequency of the cavity. Using the expression $(2a/d)^2$ (shown in Fig 3.9), a value of 2.69 for the cavity is obtained which, when placed along the TM_{010} line, does not come very close to any other modes which might interfere (demonstrated using the red vertical line). The cavity is then constructed from 2 pieces of aluminium held together using brass clasps (shown in Fig 3.12). One corner is flattened to allow a hole for an N-type connector to be passed though. This connector is open at one end and a loop is created using wire. This connector can be manually rotated and moved further in or out of the cavity to allow for critical coupling of differing samples.

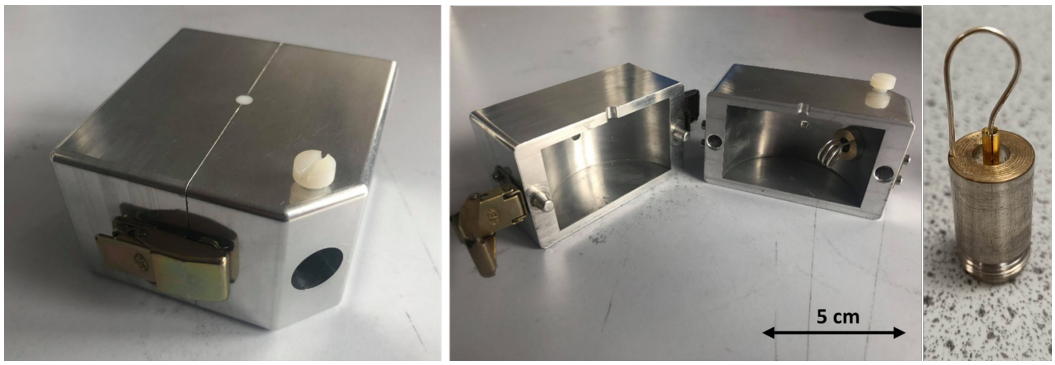

Fig. 4.13 Aluminium TM_{010} Cylindrical cavity, 3.5GHz. Outer View (Left), Inner View (Middle), and N-Type connector with coupling loop (Right). The cavity has a large hole for an N-Type connector with a larger loop to couple to samples. There are also two smaller holes for SMA connectors used to characterise the cavity (via measurement of S_{11} and S_{21} parameters).

4.4 Quantifying DNA release within Stack Cartridge Design

To confirm the effectiveness of the stack cartridge as suggested by the simulated work, a physical cartridge was created (shown in fig 4.14).

It is important initially to confirm that the reflection coefficient (S_{11}) is sufficiently low to show a high efficiency of power transmission/absorption by the cartridge and its contents. It is also important to note the frequency drop caused by the addition of the cartridge and sample to confirm it falls within the parameters of the microwave excitation system ($\sim 2.0-2.6$GHz).

Figs 4.15 and 4.16 demonstrate a frequency drop of around 1.3GHz caused by the addition of the 10ml aqueous sample to the cartridge with a reduced frequency at 2.122GHz, which is within the bandwidth of our microwave excitation system.

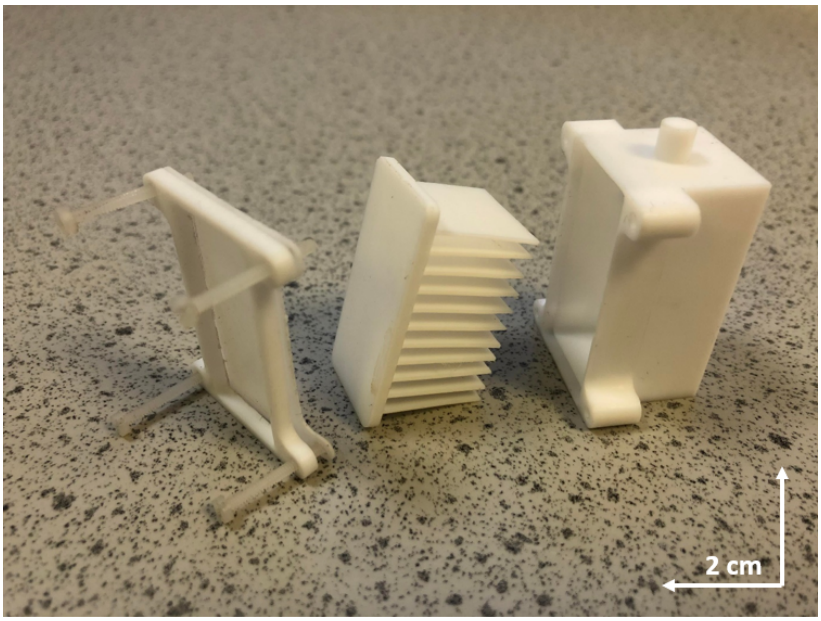

Fig. 4.14 PTFE Stack Cartridge

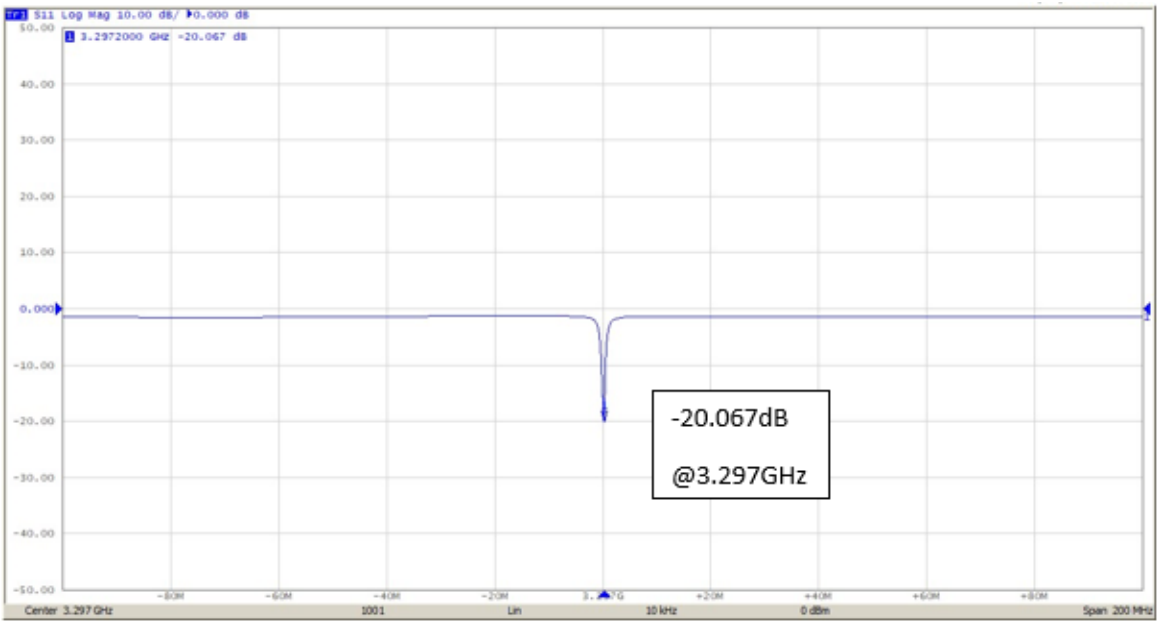

Fig. 4.15 VNA plot showing the S11 characteristic of the empty stack cartridge within the 3.5GHz microwave cavity. The resonant frequency here drops to 3.297GHz by only the addition of the empty cartridge.

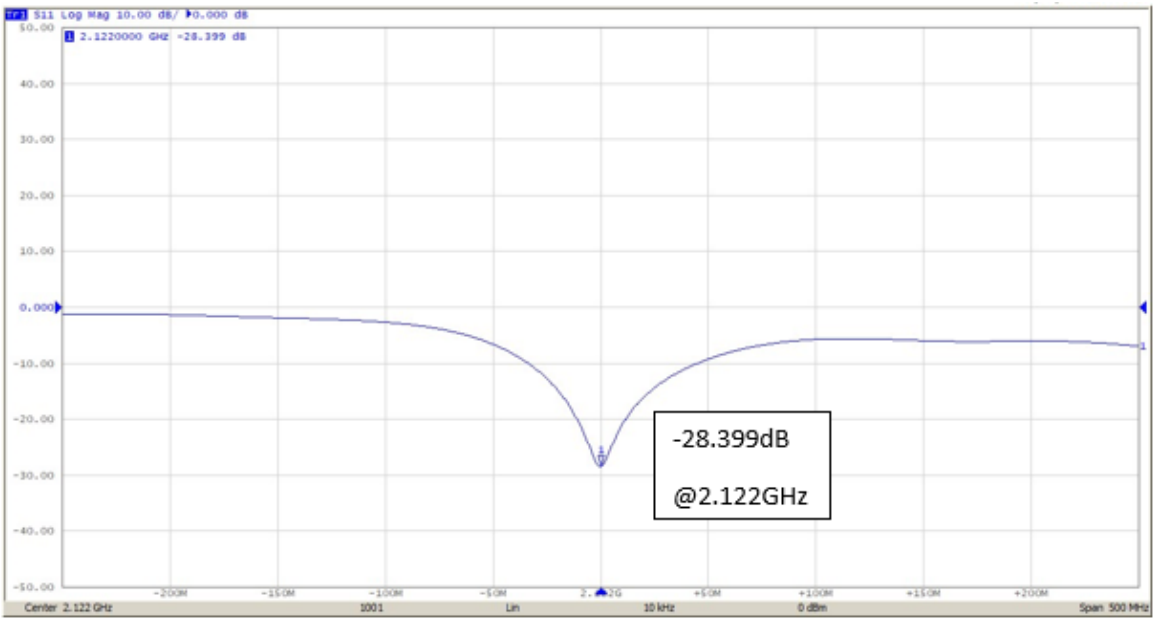

Fig. 4.16 VNA plot showing the S11 characteristic of 10ml of aqueous sample within the stack cartridge in the 3.5GHz microwave cavity. The resonance here drops to 2.122GHz.

4.5 ssDNA release from *Mycobacterium smegmatis (M.smeg)* and *Mycobacterium abscessus (M.abs)*

An initial simple experiment was undertaken to test the efficacy of this cartridge design. The most imperative outcome is the cartridge's ability to promote DNA release from mycobacteria. The technique developed to quantify the DNA release (which is discussed in greater detail in Chapter 5) require the DNA to be single stranded so it can be collected. As such, the following experiment uses the Qubit ssDNA Assay Kit for quantification [160]. Many thanks here are given to Dr Evans Ahortor and Suzan Abdullah A Alzeer for providing bacterial cultures and support with microbiological work.

4.5.1 Propagation of *M.smegmatis* & *M.abcessus*

The rapidly growing mycobacterial strains (*M. smegmatis* Mc2155(S2) and *M. abscessus* ATCC 19977) used in these studies were incubated in 50ml LB broth for 3 days in a shaking incubator (MaxQTM440, Thermo Scientific) at 200 rpm, after which they were centrifuged at 4000 x g for 10 mins. The resulting pellet was washed three times using phosphate buffered saline(PBS) and finally re-suspended in 1ml PBS.

4.5.2 Qubit Fluorometer ssDNA Quantification

The ssDNA was quantified using the Qubit™ ssDNA Assay Kit [160]. The working solution was prepared as standard using 25μl of the reagent and 4.975ml of the buffer solution (allowing for 25 measurements to be taken). The upper and lower boundaries were obtained by mixing 10μl of the Standard #2 and Standard #1 to 190μl of working solution, respectively. These were measured using the 'oligo' setting on the Qubit Fluorometer. The ssDNA content of each sample was then measured by adding 20μl of the sample to 180μl of working solution and using the 'oligo' setting on the fluorometer.

4.5.3 Microwave Excitation

The excitation time for the 10ml sample was initially estimated by extrapolating the excitation time used for the 200μl samples. The 200μl sample are microwaved at 12W for 20 seconds using a 20% duty cycle (as demonstrated by Ahortor. E to yield the highest ssDNA release [23]). This was extrapolated using the ratio of sample volumes ($\frac{10}{0.2}$), multiplying the excitation time by this value and then dividing by 2 (achieved by removing the duty cycle) yielding an excitation time of around 8 minutes using the same 12W power level.

The results for both the 200μl sample and the 10ml sample are shown side by side for comparison in fig 4.17. The results show ssDNA release occurs with both isolates but also suggest that *M.abs* is most susceptible to microwave interaction than *M.smeg*, as the ssDNA

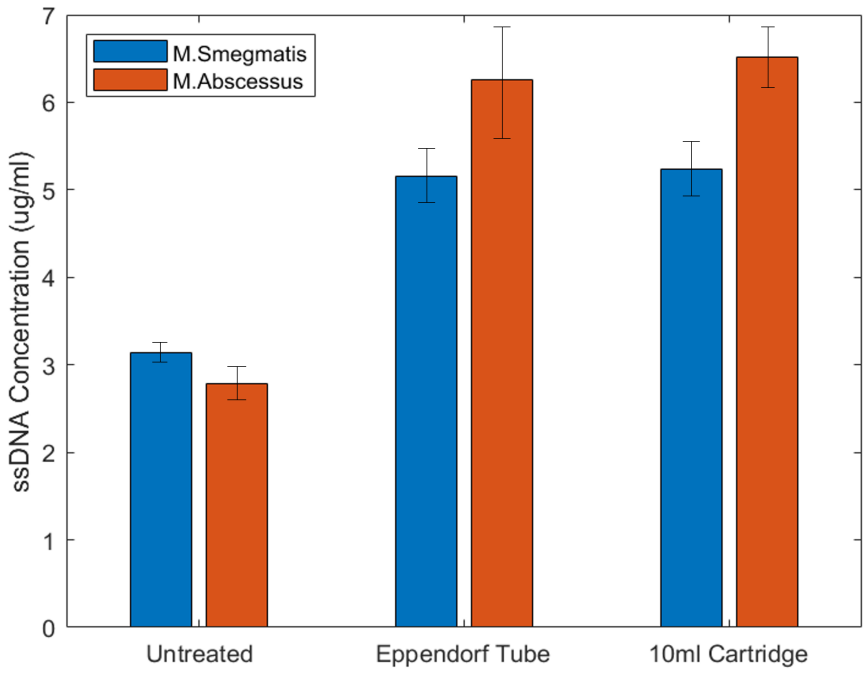

Fig. 4.17 Bar graph showing the ssDNA release of *M.smeg* and *M.abs* (conc. 10^8 CFU/ml) using both the Eppendorf (12W, 20 seconds, 20% duty cycle) and 10ml Cartridge (12W, 8 minutes, no duty cycle) setups. Error bars show 1 standard error either side of the mean resultt, following 3 biological and 3 technical iterationst. The "Untreated" column denotes the ssDNA present without any microwave interaction.

release is 76% higher for the Eppendorf method and 79% higher for the 10ml cartridge method.

4.6 Discussion

The results of this section show that a 10ml cartridge has been created able to promote microwave interaction with samples and ssDNA has been successfully released from 2 different mycobacterial isolates used as surrogates for *M.tb*. The microwave applicator system has received some changes to help maintain the necessary operating frequency despite a greater frequency change due to a large sample. The 10ml cartridge has proved to be comparable to the Eppendorf tube in ability to cause ssDNA release.

Subsequent chapters will look at the further optimisation of this 10ml cartridge method by using simulated sputum samples to more accurately predict the microwave interaction with real world samples. A full extraction method will also take place using probes and nanoparticles to collect the ssDNA released. Further work will also look at the automated mixing and collection of these magnetic nanoparticles using external electromagnets and microfluidics to direct and concentrate the DNA coated nanoparticles to a specific point where signal detection can take place.

Chapter 5

Optimization of ssDNA release and capture from Mycobacteria

5.1 Introduction and Chapter Aims

As the viability of the 10ml cartridge design has been verified in the previous chapter, it is now necessary to optimise the parameters of the microwave excitation to ensure the maximum quantity of ssDNA (required for collection via DNA specific probes) is released. Another objective of the project is to minimise the power usage for this process such that it becomes viable in areas with limited power (allowing for a potentially battery powered/solar powered system). As such, it is important to demonstrate the lowest possible power usage of the excitation whilst maximising ssDNA release.

It is important to consider the variability of samples that will be encountered by this system. A sputum sample provided by every individual person will be different, depending on a wide variety of factors. This will greatly affect the global permittivity value of the sample which can have a large impact on the resonant frequency of the sample loaded cavity, and which will necessitate a large degree of variability on the part of the microwave excitation system. Additionally, this permittivity will have a large impact of the strength of the E field

applied to the sample, leading to very different excitation times needed to produce maximum ssDNA release.

Finally, it will be important to understand the affect the addition of magnetic nanoparticles will have to the ssDNA release. These are likely to produce small amplified regions of E-field which may contribute to faster ssDNA release but could also lead to degradation of the released ssDNA if the excitation time is not altered appropriately. To optimise these parameters, the surrogate organisms *M.smeg* and *M.abs* were used in the initial studies as they are easier to grow than *M.tb* and are considerably less pathogenic. The results of these studies were verified using *M.bovis* as a more accurate surrogate for *M.tb*.

5.2 Methods

5.2.1 Propagation of *M.smegmatis* & *M.abcessus*

The rapidly growing mycobacterial strains (*M. smegmatis* Mc2155(S2), and *M. abscessus* ATCC 19977) used in these studies were incubated in 50ml Luria-Bertani (LB) broth for 3 days in a shaking incubator (MaxQTM440, Thermo Scientific) at 200 rpm, at 37°C after which they were centrifuged at 4000g for 10 mins. The resulting pellet was washed three times using Phosphate Buffered Saline(PBS) and finally re-suspended in 1ml PBS. LB broth was purchased from Thermo Fisher Scientific Ltd, UK. Yeast extract, it was prepared according to manufacturer's protocol and sterilised for 15 minutes at 121°C and 100 kPa using a bench top autoclave (CertoClav EL sterilizer, Austria). Both strains were purchased from the HPA Culture Collections Service (Public Health England, Porton Down, UK).

5.2.2 Propagation of *M.bovis*

The slow growing *M.bovis* BCG (str. Pasteur 1173P2) was incubated in 10ml of 7H9 broth media (Becton Dickinson and Company) incubated for 2 weeks at 37°C in a shaking incubator

(MaxQTM440, Thermo Scientific) at 200 rpm. The resulting pellet was washed three times in PBS and finally re-suspended in 1ml PBS.

5.2.3 Determination of the Purity of Individual Cultures using the Streaking Method

LB agar plates were used for *M.Smeg* and *M.abs* and prepared as follows: 37g of LB Agar powder was added to 1000ml water and autoclaved at 121°C and poured into individual plates to set.

7H10 plates were used for *M.bovis* and prepared as follows: Suspend 19.47 g of Middlebrook 7H10 Agar base in 900 ml of molecular grade water containing 5 ml of glycerol. Autoclave at 121°C for 10 minutes. Cool to 50-55°C and aseptically add 100 ml of Middlebrook OADC Enrichment. The liquid was then poured into individual agar plates to set.

The bacterial colony was gently touched using a 10μl loop and spread the material over the first quadrant of the agar plate, then turn the Petri dish 90 ° and streak the second quadrant with new loop. Near the end of the last streak, using the back-and forth pattern, cross over the last half of the streaks in the first quadrant then move into the empty second quadrant. Repeat this step with the third and fourth quadrants. Invert the plate upside down and incubate at 37°C for 48 - 72 hours in the case of *M. abs* and *M.smeg*, and for two weeks for *M.bov*. Single colonies were observed for uniformity and the colonial morphology associated with the particular strain.

To further assist in the characterization of individual isolates, colonies were stained using the Ziehl Neelson method (described in section 2.5.1) after which they were observed using a light microscope (Leica DM750) under oil immersion using x100 objective lens.

5.2.4 Standardization of Cell Concentration

To standardise the bacterial concentrations, a calibration curve was generated by correlating cell concentration with varying optical densities (OD). Initially, M. bovis, M. abscessus, and M. smegmatis cells were cultured and pelleted by centrifugation at 4000 × g for 10 minutes. The bacterial pellets were washed twice with sterile 1X PBS solution to prepare the stock bacterial concentration. This stock concentration was serially diluted (1/10) in PBS to create bacterial suspensions with OD values ranging from 0.05 to 1.2 (measured at 600 nm). These suspensions were further diluted (1/10) in eight sequential steps. 20 µL from each dilution was plated in triplicate on the appropriate agar media. The plates were then incubated under the required conditions for each organism. The lowest dilution that yielded between 30 and 100 countable colonies on the agar plate was used to determine the cell concentration of each sample (expressed as CFU/mL). This process was repeated twice to ensure accuracy, and the mean colony-forming units were calculated using the following formula:

Colony-forming units per millilitre (CFU/mL) = Mean colony count × dilution factor / Volume inoculated (mL)

The mean number of colony-forming units per millilitre (y-axis) was plotted against the optical densities on the x-axis, and a line of best fit was generated. The estimated concentration of cells was calculated from the graph equation with known optical density values. While initial calculations were performed using bacterial concentrations (CFU/mL), all results are expressed as total bacterial quantities (CFU) to simplify data interpretation and emphasise the total bacterial load within the sample volume.

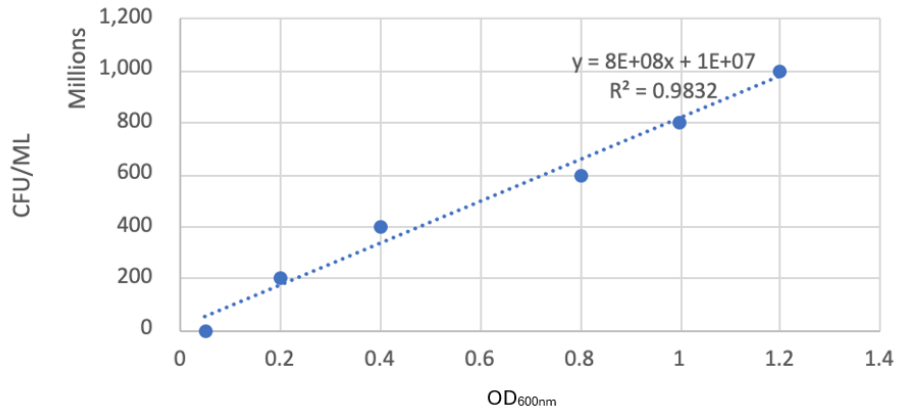

Fig. 5.1 The OD600 was determined as standard by adding multiple ($N = 3$) 20μl drops of stock bacteria with factor of 10 serial dilutions. A dilution was determined with a countable (between 30 and 300) number of colony forming units in each 20μl section.The OD600 was then measured using a spectrophotometer (Ultraspec 2100 pro, Amersham Biosciences)

5.2.5 Simulated Sputum

A simulated sputum solution was prepared to mimic the viscosity of a human sputum sample. This was created by mixing 1% methyl cellulose (viscosity = 4000cPs) in 500ml molecular grade water using a magnetic stirrer until fully dissolved [161]. The solution was then autoclaved to sterilize (140°C, 45 minutes). Each bacterial stock was diluted to 10^8 CFU/ml (dilution first assessed in water using the $OD600_{nm}$, determined as shown in fig 5.1, then diluted with sufficient simulated sputum) in a 10ml solution for the microwave excitation optimisation experiment using water or the simulated sputum mixture.

5.3 Enzyme Linked Oligonucleotide Sandwich Hybridisation Assay (ELOSHA)

It is essential for a fully integrated diagnostic method to incorporate a method of ssDNA capture and quantification following release via microwave excitation. Until this point, the

Qubit 3.0 fluorometer has been used to quantify ssDNA release. To integrate pathogen specific DNA detection into our system, the following method has been developed (known as ELOSHA) which quantifies ssDNA release and capture using Horseradish Peroxidase (HRP) coated magnetic nanoparticles (method outlined in fig 5.2 [23]). Streptavidin coated magnetic beads, coupled with two specifically designed probes, one labelled with biotin and the other horse radish peroxidase (HRP), formed the basis of the assay. The presence of the DNA target was indirectly identified via the catalytic conversion of 3,3',5,5'-Tetramethylbenzidine by HRP. A set of probes were designed based on a pair of PCR detection primers specific to IS1081 [173]. Anchor and reporter probes were designed and labelled with biotin and HRP respectively. The anchor probe was 17 nucleotides in length and had a biotin label at the 5' end, followed by 5 thymine (5T) residues to enhance probe flexibility. The reporter probe has 22 nucleotides and was labelled with HRP at the 3' end.

biotin -TTTTT-CCCTGCTGCACTCCATCTACGACCAGCCCGACGCCGAATCAGTT-HRP

GGGACGACGTGAGGTAGATGCTGGTCGGGCTGCGGCTTAGTCAA GTTGC

5.3.1 5.2 Functionalization of magnetic particles with target specific DNA probes

Preparing high-quality DNA/magnetic particles (MPs) conjugates is challenging. Ideally, the resulting conjugate should demonstrate colloidal stability, efficient DNA probe labelling, and presentation to maximize hybridization with the target DNA, while minimizing non-specific DNA binding. DNA probes are attached to MPs using various chemistries. For instance, thiol groups can be attached to the terminals of the DNA probe, enabling the DNA to bind to metal surfaces through a metal-thiolate bond. A metal–thiolate bond is a type of chemical bond formed between a metal atom and a thiolate (or thiol) group. Aslan and colleagues utilized a thiolated DNA probe attached to silver to develop a system capable of detecting B. anthracis in under 30 seconds [20]. Other methods for attaching DNA sequences to MPs have been developed, including chemical modification of the MPs' surface to incorporate functional groups such as carboxylate (-COOH) or amine (-NH2).

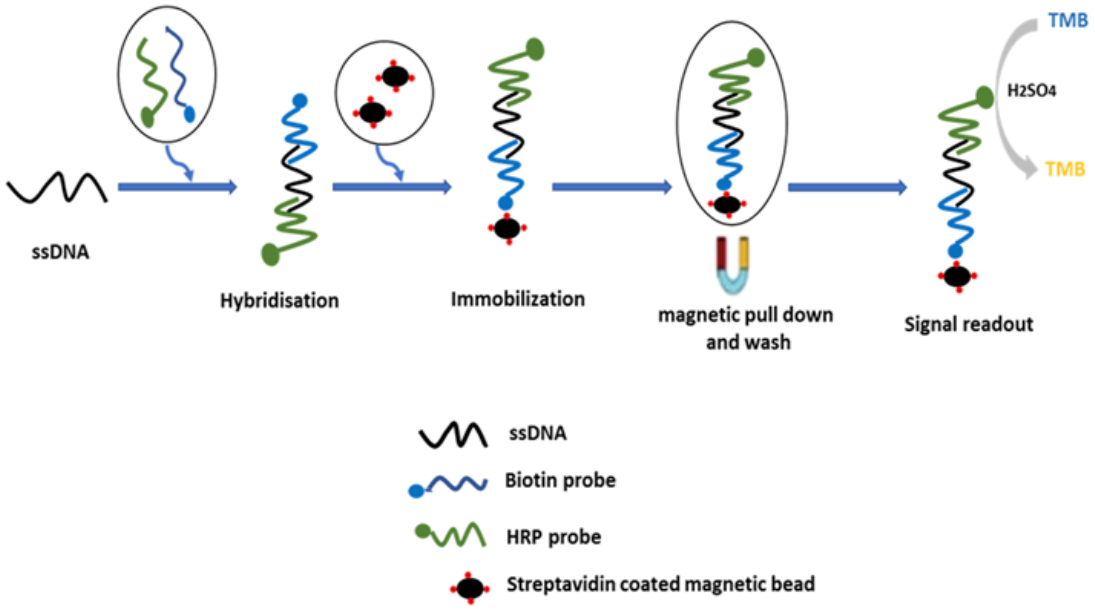

Fig. 5.2 A cartoon describing the various steps in the target DNA capture and detect process. After the ssDNA has been released, it is captured by pathogen DNA specific biotin probes attached to magnetic nanoparticles. Pathogen specific HRP DNA probes are also added which attach to the opposite end of the DNA strand to the biotin. These structures can be pulled out using a magnet and washed to remove the excess sample. The quantity of HRP probe removed can then be measured afterwards [24]. The reaction is halted using sulphuric acid, addition of peroxidase causes the colour change from blue to yellow in the presence of HRP

Proteins such as streptavidin can also be used. Streptavidin provides high-affinity biotin binding. The streptavidin-biotin complex is a potent binding partner found in nature, exhibiting binding strengths significantly greater than those of typical protein-ligand pairs. In the previously studies undertaken in our laboratory, we have shown that commercially available streptavidin coated MPs (Dynabeads MyOne streptavidin coated beads C1) labelled with biotin tagged DNA probes in combination with microwaves can be used to detect *M. abs* and *M. smeg* [23]. This study will build on these results to develop an approach capable of detecting *M.bov*.

5.3.2 Microwave Parameter Optimisation

The microwave power level used to extract bacterial DNA from intact organisms was fixed at 12W with zero duty cycle to minimise the excitation period. The time parameter was increased steadily from 0 to 16 minutes with 2 minute intervals (using separate sample for each iteration) to identify optimum settings for the release of ssDNA. Power transfer efficiency did not drop below 90% for any iteration ($N = 3$). The ssDNA release was quantified using the Qubit ssDNA Assay Kit(Invitrogen) and Qubit Qubit 3.0 fluorometer (Invitrogen).

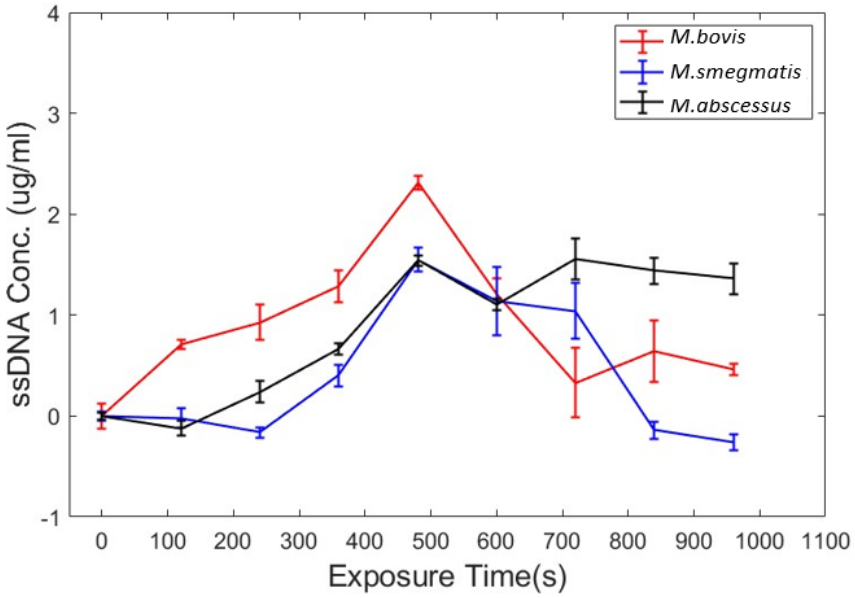

Fig. 5.3 Microwave Mediated ssDNA release using 10ml Stack cartridge from 10^8 CFU/ml sample of various Mycobacteria in molecular grade water. The data has been corrected by subtracting each respective time 0 value. The error is shown as 1 standard error away from the mean value ($N = 3$).

The data presented in figs 5.3 and 5.4 have been corrected by subtracting the time 0 results respectively for each mycobacteria to eliminate the measurement of the background ssDNA in the sample. It clearly demonstrates that the maximum ssDNA release occurred after 480 seconds (or 8 minutes) for all samples (the data for *M.abscessus* in simulated sputum, however, showed that

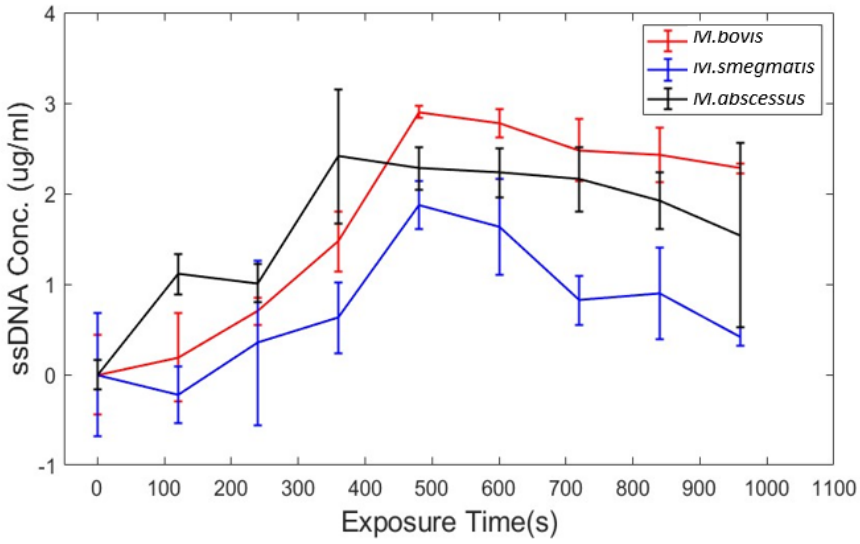

Fig. 5.4 Microwave Mediated ssDNA release using 10ml Stack cartridge from 10^8 CFU/ml sample of various Mycobacteria in Simulated Sputum. The data has been corrected by subtracting each respective time 0 value. The error is shown as 1 standard error away from the mean value ($N = 3$).

the ssDNA concentration peaks after 6 minutes and remained constant until the 8 minute mark). Establishing an 8 minute excitation period for a 10ml sample size is therefore justified. These parameters were used for all experiments going forward. The simulated sputum data also demonstrated a greater variation (the error margins are an average of 176% larger than the data in water) of ssDNA concentration compared to the data obtained from samples suspended in water, suggesting that the non-uniform nature of the simulated sputum resulted a non-uniform release of ssDNA. The simulated sputum data also demonstrates a greater retention of ssDNA for *M.bovis* and *M.smeg* after the 500 seconds mark. After this point, the ssDNA released in the *M.bovis* and *M.smeg* water samples seems to degrade at a much faster rate. The ssDNA concentration for *M.smeg* is below the normalized 0 level at 960 seconds, showing that up to 100% of the released ssDNA has been destroyed. For *M.bovis* the ssDNA concentration is 0.4μg/ml (normalized) at 960 seconds, meaning that 83.3% of the released DNA had been destroyed. The results for *M.bovis*, *M.smeg*, and *M.abs* in simulated sputum show an average reduction in ssDNA of 11%, 21%, and 64%, respectively. As these are far lower than for

the water samples, this could suggest a certain level of protection for the released ssDNA given by the simulated sputum; however, the high variability in measurements makes it difficult to be fully confident in this assumption.

The final experiment in this chapter determines the ability of DNA probes with specificity for a region of DNA within the IS1801 gene which is unique to *M.bovis*, to distinguish the bacterium from other Mycobacterial species (the IS1801 specific gene probes were designed and validate by Mrs Suzan Alzeer, PhD student, School of Pharmacy and Pharmaceutical Sciences, Cardiff University 2022). This was achieved by combining microwaved extracted DNA with DNA capture using DNA probe functionalized magnetic nanoparticles (Dynabeads™MyOne™ Streptavidin C1). The MP/target DNA complex was detected by a send target DNA specific probe labeled with an enzyme (HRP) in a process known as Enzyme Linked Oligonucleotide Sandwich Hybridisation Assay (ELOSHA) [23]. Figs 5.5 to 5.8 show the specificity of *M. bovis* detection and sensitivity of *M. bovis* detection in water and simulated sputum samples respectively.

As can be seen in fig. 5.5, *M.bovis* generated a significantly stronger signal (p-value < 0.05, one way ANOVA) than the other non-*M.bovis* isolates when suspended in PBS. The limit of detection of the combined microwave/ELOSHA system was determined using different concentrations of *M.bovis* suspended in PBS. As can be seen in fig. 5.6 a significant (p-value < 0.05) signal was observed at a concentration of 10^4 CFU/ml as determined using a one way (ANOVA) test.

These experiments were repeated with bacteria suspended this time in simulated sputum. The simulated sputum experiments show the same relationship. The *M. bovis* absorbance is significantly higher, and the other two Mycobacteria isolates show similar absorbance as the control (NTC), demonstrated in fig 5.7. Similarly, the limit of detection of the combined microwave/ELOSHA system was determined using different concentrations of *M.bovis* suspended in PBS. As can be seen in fig. 5.8, a significant (p-value < 0.05) signal was observed at a concentration of 10^4 CFU/ml as determined using a one way (ANOVA) test.

5.4 Discussion

The ability of the 10ml cartridge to aid in the release of ssDNA from bacterial samples using mycobacteria has been confirmed. This process has also been optimised to release as much ssDNA as possible to be captured by pathogen specific DNA probe coated magnetic nanoparticles. It has also been confirmed that the microwave extracted DNA has been recognised (and attached) to the pathogen specific DNA probes using pathogen specific HRP probes. The 10ml cartridges limit of detection is shown to be $10^4 CFU/ml$ for *M.bov*, equivalent to the previous approach using eppendorf tubes ($7.8 \times 10^4 CFU/ml$ as shown in [23]). This is currently 100x less sensitive than the industry standard (PCR, $10^2 CFU/ml$,[162]) and is similar to other standards such as microscopy (5000 CFU/ml, [106] [107]). While the simulated sputum is a good substitute to mimic the viscosity of a patient sample, its composition is far simpler. Further experiments with genuine patient sputum samples would be necessary to verify fully the efficacy of the assay for real world samples. The fact that there is no drop in detection or sensitivity of the method from samples in water and samples in simulated sputum is, however, a good indicator that the viscosity of human sputum will not affect the sensitivity of the assay.

Future studies will look at replacing the HRP probes with fluorescent probes, or look to adopt an SPR approach as methods of pathogen detection that can be integrated into a single system. This will increase the sensitivity of the assay, as well as allow all stages of the diagnosis (microwave extraction, magnetic mixing/collection, and detection) to occur in one device. This is further explored in the next chapter.

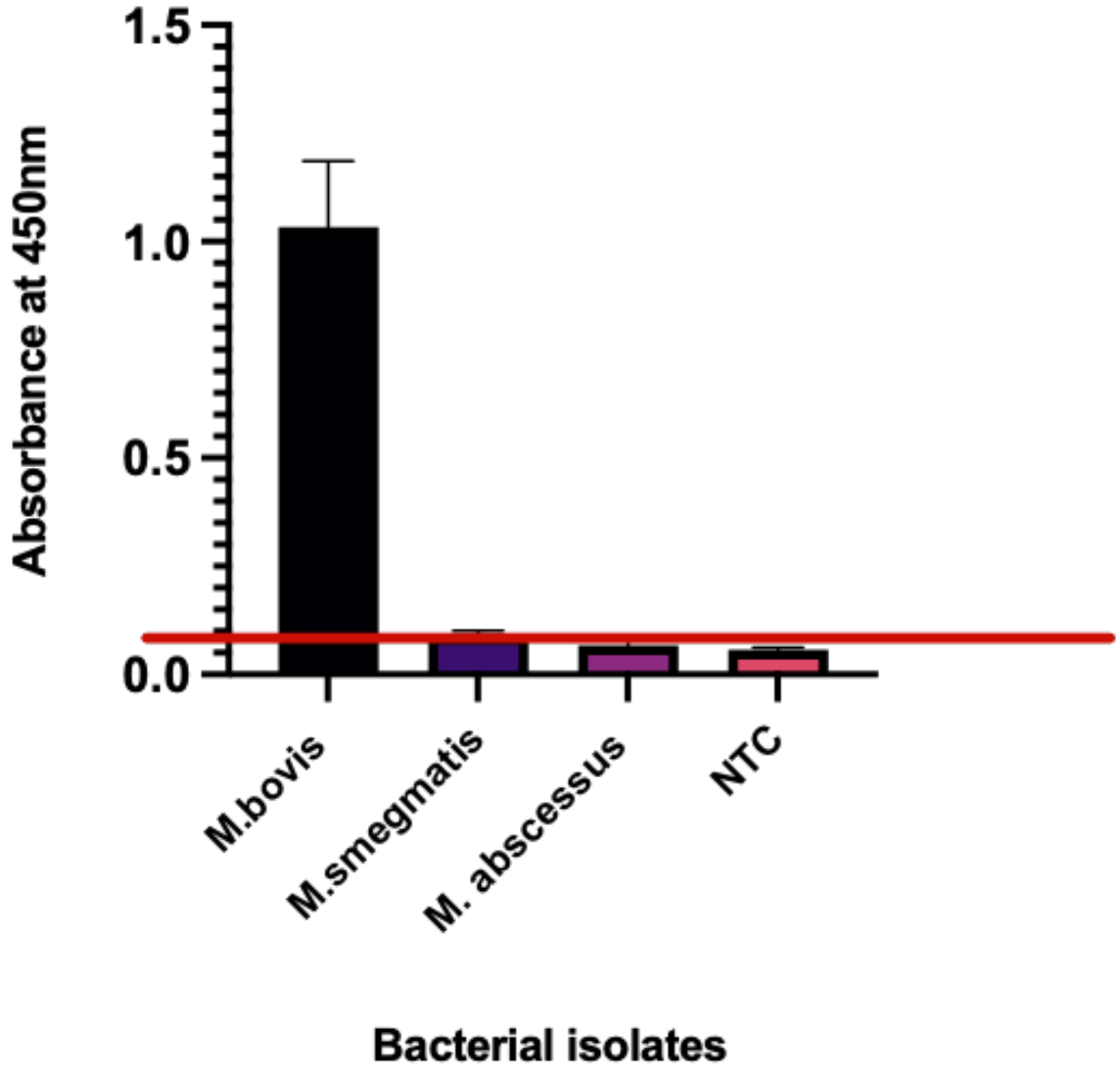

Fig. 5.5 **Detection of *M.bovis* using a combination of microwaves and ELOSHA.** *M. bovis* BCG str. Pasteur 1173P2, *M. smegmatis* Mc2155(S2) and *M. abscessus* ATCC 19977 suspended in PBS were microwaved and probed with magnetic nanoparticle and IS1801 specific probes. The presence of target specific DNA was determined by the intensity of the colour change due to the action of HRP. A positive cut-off value for the assay was determined as the mean optical density (OD) plus three x3 mean values of the mean value of *M.smegmatis* which is indicated by a red horizontal line (NTC = No template control). Data represents mean of triplicate experiment (3 technical x 3 biological) ± standard error.)

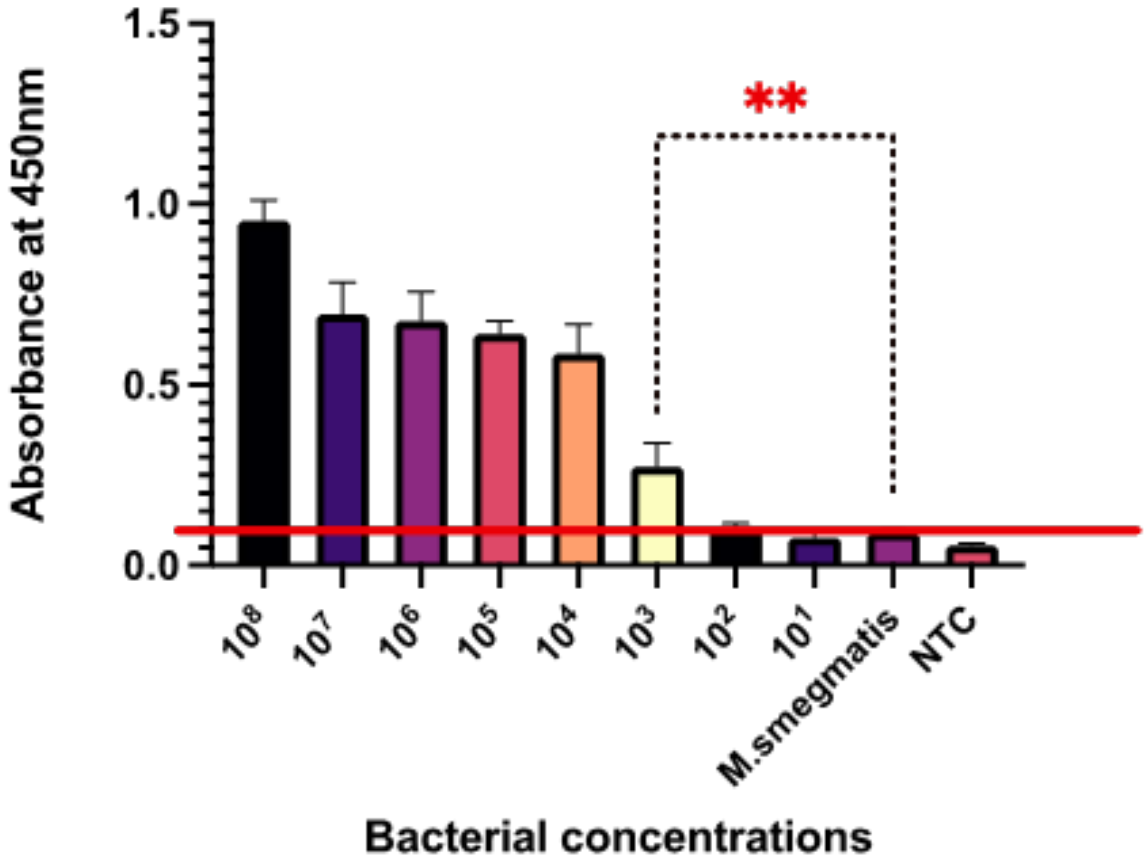

Fig. 5.6 **The limit of detection of the combined microwave and ELOSHA assay for *M.bovis*** A culture of *M. bovis* BCG str. Pasteur 1173P2, was serially diluted in molecular grade water to generate a concentration range from 10^8 CFU/ml to 10^1 CFU/ml. Each bacterial concentration was analyzed for its ability to generate a signal following processing. A positive cut-off value for the assay was determined as the mean optical density (OD) plus three 3x standard deviation of the mean value of *M. smegmatis* Mc2155(S2) (at 10^8 CFU/ml) as indicated by a red horizontal line (NTC = No template control. Data represents mean of triplicate experiment (3 technical x 3 biological) ± standard error. ** demonstrates the lack of significant difference between the $10^8 CFU/ml$ *M.megmatis* control and the $10^3 CFU/ml$ *M.bovis* measurement).

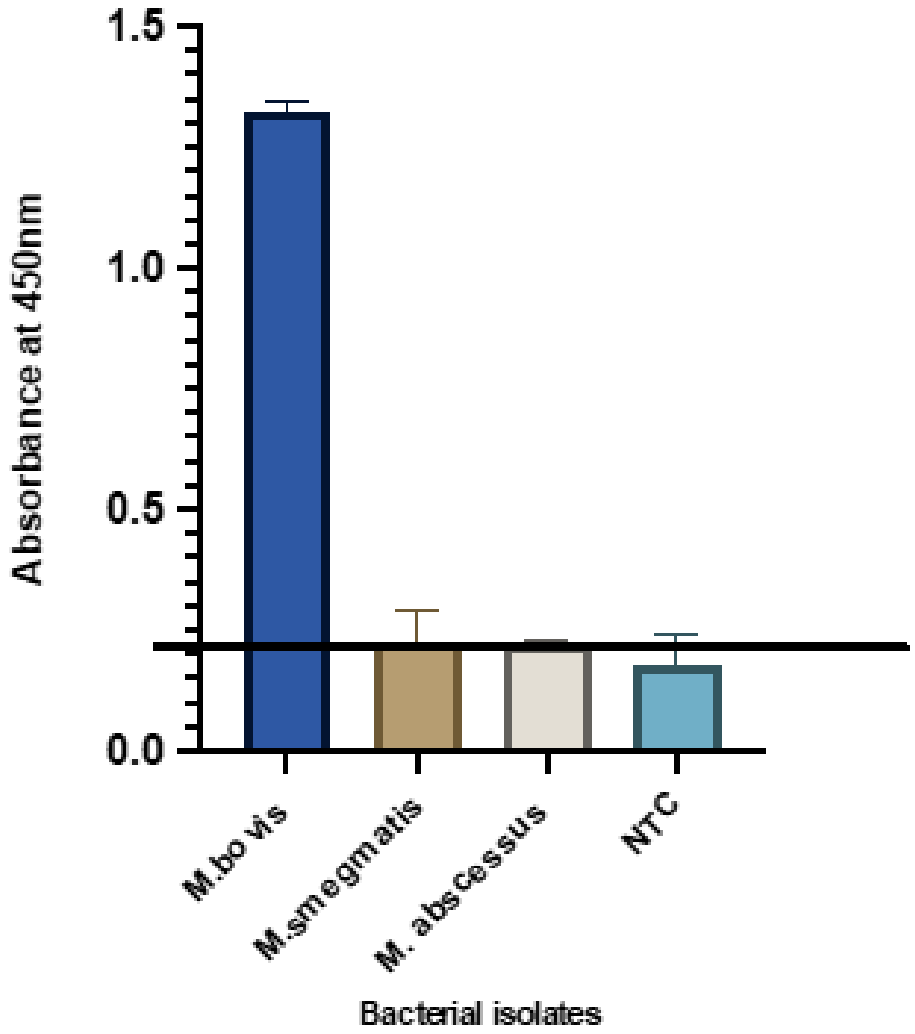

Fig. 5.7 **Detection of *M.bovis* using a combination of microwaves and ELOSHA.** *M. bovis* BCG str. Pasteur 1173P2, *M. smegmatis* Mc2155(S2) and *M. abscessus* ATCC 19977 suspended in simulated sputum were microwaved and probed with magnetic nanoparticle and IS1801 specific probes. The presence of target specific DNA was determined by the intensity of the colour change due to the action of HRP. A positive cut-off value for the assay was determined as the mean optical density (OD) plus three x3 mean values of the mean value of *M.smegmatis* which is indicated by a red horizontal line (NTC = No template control. Data represents mean of triplicate experiment (3 technical x 3 biological) ± standard error.)

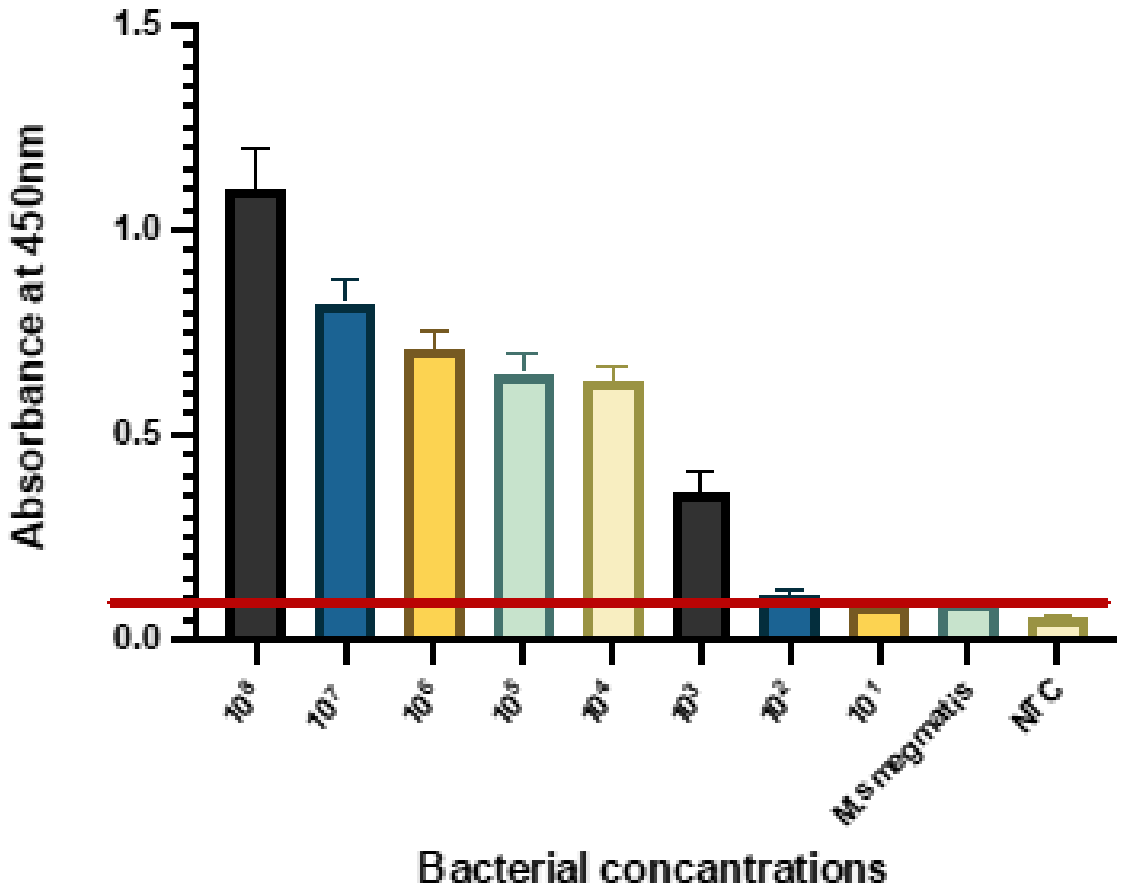

Fig. 5.8 **The limit of detection of the combined microwave and ELOSHA assay for *M.bovis*** A culture of *M. bovis* BCG str. Pasteur 1173P2, was serially diluted in simulated sputum to generate a concentration range from 10^8 CFU/ml to 10^1 CFU/ml. Each bacterial concentration was analyzed for its ability to generate a signal following processing. A positive cut-off value for the assay was determined as the mean optical density (OD) plus three 3x standard deviation of the mean value of *M. smegmatis* Mc2155(S2) (at 10^8 CFU/ml) as indicated by a red horizontal line (NTC = No template control. Data represents mean of triplicate experiment (3 technical x 3 biological) ± standard error. ** demonstrates the lack of significant difference between the $10^8 CFU/ml$ *M.Smegmatis* control and the $10^3 CFU/ml$ *M.bovis* measurement).

Chapter 6

Manipulation of DNA Coated Magnetic Nanoparticles

6.1 Introduction and Chapter Aims

The overarching aim of this project is the creation of an all-in-one, point of care assay capable of diagnosing TB (although there are other additional inclusions which would provide greater utility; diagnosis of additional mycobacteria; diagnosis of antibiotic resistance in mycobacteria; and multiplexing diagnosis; to name a few). One essential inclusion is the ability to mix the nanoparticles within the cartridge once the DNA has been released to maximise the binding of target DNA and thus optimise sensitivity. The collection and transport of DNA coated nanoparticles, potentially to a separate cartridge for further interrogation, will depend on the method used to detect the binding of pathogen specific DNA. In an ideal sense, this detection event will occur within the sample cartridge to minimise cross contamination and the exposure of the assay operator to potentially infectious material. This chapter explores a variety of nanoparticle manipulation methods using external electromagnets and microfluidics to perform the required actions.

6.2 Techniques for Integrated Diagnosis

An intrinsic aspect of this project is the ability to identify the presence of the pathogen-specific DNA in patient samples released following microwave exposure in an integrated system. The challenge is to develop a system which maximizes target sensitivity, prevents contamination the assay platform, and reduces exposure of the operator to infectious material.

In partnership with colleagues in Ukraine (at The Institute of Environmental Geochemistry of National Academy of Sciences of Ukraine) we have explored the feasibility of developing an approach which replaces the current pathogenic DNA enzyme labeled HRP probes with fluorescent alternatives. Using this approach, the magnetic nanoparticles with their pathogen-specific DNA cargo can then be extracted into a secondary cartridge which feeds into a fluorescence measuring device. This device flashes light through the extracted nanoparticle sample and reads the resulting fluorescence. If pathogen DNA is present in the sample, the intensity of the fluorescent signal will be proportional to the amount of DNA which is present (demonstrated in table 6.1).

This approach combines high specificity with the ability to detect multiple targets in a single sample. This can be achieved by using DNA probes labelled with fluorophores, which fluoresce at different wavelengths (say red for *M.tuberculosis*). It is also theoretically possible to add another wavelength probe (say green) and design it to attach to *M.bovis* DNA.

Fluorophore	**Absorbance (nm)**	**Emission (nm)**	**Visible Colour**
Alexa fluor 448	494	517	green
Alexa fluor 568	578	603	red

Table 6.1 Examples of fluorphores than can be attributed to different pathogen DNA.

Thus one could detect different pathogens in the same sample by exposing the sample to different wavelengths, as two distinct peaks would be visible at different parts of the colour spectrum. This can then be extrapolated to encompass multiple pathogens, but will likely be limited by fluorescent peak overlap and peak reduction (i.e. if two fluorescent probes have too similar a wavelength but

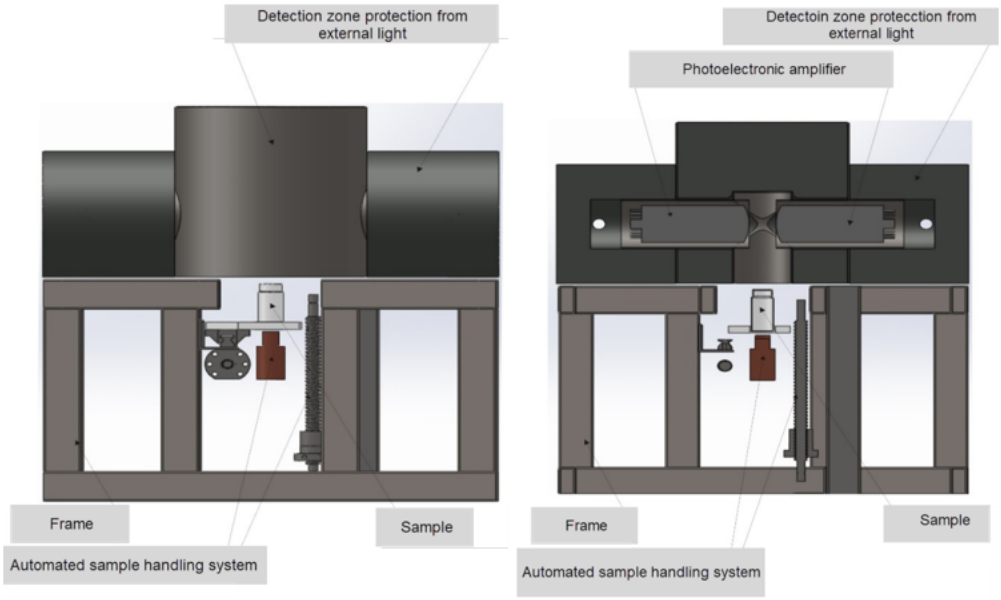

Fig. 6.1 Visualization of measurement device for fluorescent probe attached DNA. (The Institute of Environmental Geochemistry of National Academy of Sciences of Ukraine, 30/10/2023)

a sample contains significantly more of one pathogen than another then the peak caused by the majority pathogen may reduce the visibility of the peak caused by the minority pathogen, thereby adding uncertainly and necessitating a secondary run using only the minority probes). The size of the fluorescence measuring device will also need to be considered as it will add to the overall weight of the system and may result in a device which is less portable than desired. The fluorescent probes will also add to the cost of the assay.

A redesign of the cartridge and cavity have been included in this chapter as an initial idea for increased user safety and integration with the fluorescence system (shown in the following section).

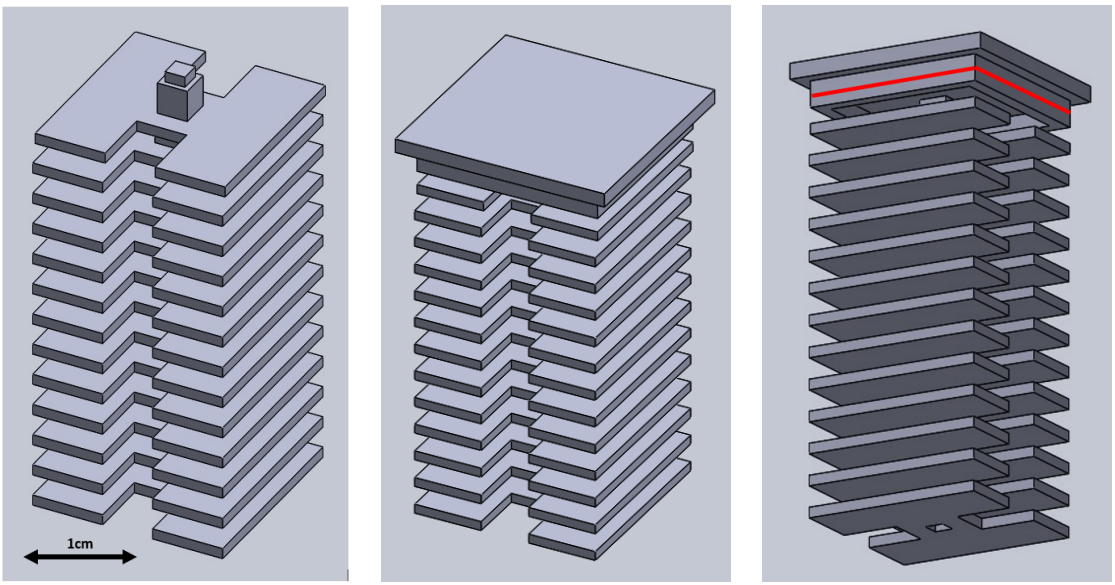

Fig. 6.2 Sealed cartridge design. Left: Horizontal section held together by central column. Middle/Right: Horizontal section with lid included. Constructed in SolidWORKS.

6.3 Cartridge redesign to increase user safety

While the previous cartridge design has proven functional, there is still an issue with user safety. The cartridge has a tendency to leak when it is excited inside the cavity. Using real-world patient samples this would increase the risk of exposure of the operator to infectious material, as well as cross contaminating other samples.

As shown in fig 6.2, the horizontal sections have been redesigned as a separate object held together by a small central column connected to the lid. The lid has a small protruding lip which fits snugly into the body of the cartridge (shown in fig 6.3). To create a seal, a small groove will be milled around the perimeter (demonstrated by the red line) to house an O-ring, rendering the cartridge watertight when pushed into the body. The horizontal sections also have rectangular sections cut out to avoid a plunger type effect on the sample when it is pushed into the body (thus causing a spill) and to allow the magnetic nanoparticles to be magnetically manipulated/collected at a bottom corner of the cartridge when excitation is complete.

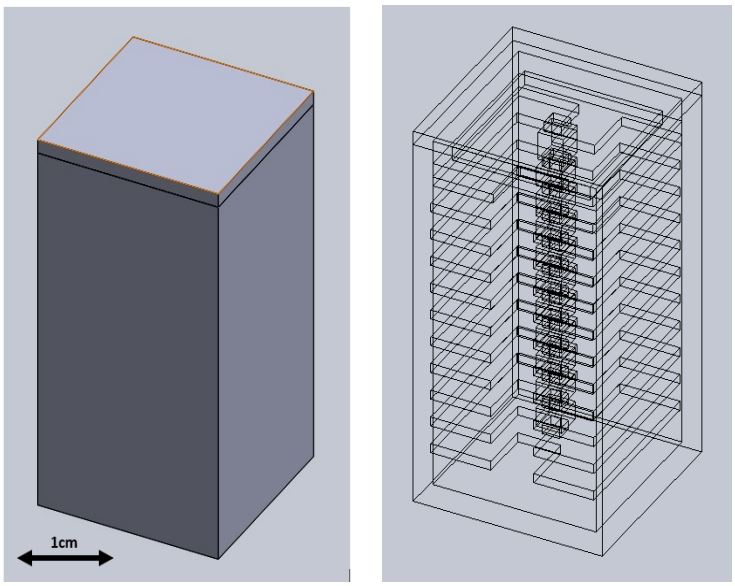

Fig. 6.3 Inner section fitted into cartridge body. Also shown as transparent so the full inner structure can be seen.

6.4 Microwave cavity design for integration with fluorescent probe diagnostic method

The design of the fluorescence measurement system is fairly simple (demonstrated in fig 6.4). A sample is placed in an optically clear cuvette between an emitter and detector. The laser (shown as a red arrow) emitted by the emitter is uniform for each iteration. The detector then measured any difference in the light intensity across the spectrum occurring in the sample, the presence of fluorescent probes causes a large difference at a specific wavelength (determined by the probe design).

From information given by the Ukrainian partner, the detector and emitter can be up to 10cm apart. The cavity design shown in fig 6.5 has two major alterations to incorporate the redesigned cartridge and potentially integration with a fluorescent detection system. The first is a pair of aligned 5mm x 5mm square holes drilled either side of the cavity in opposite parallel walls (shown on the left image of fig 6.5). These allow the laser to pass through the cavity and interact with the cartridge and sample (shown by the red arrow in the right hand image). Assuming the emitter and detector

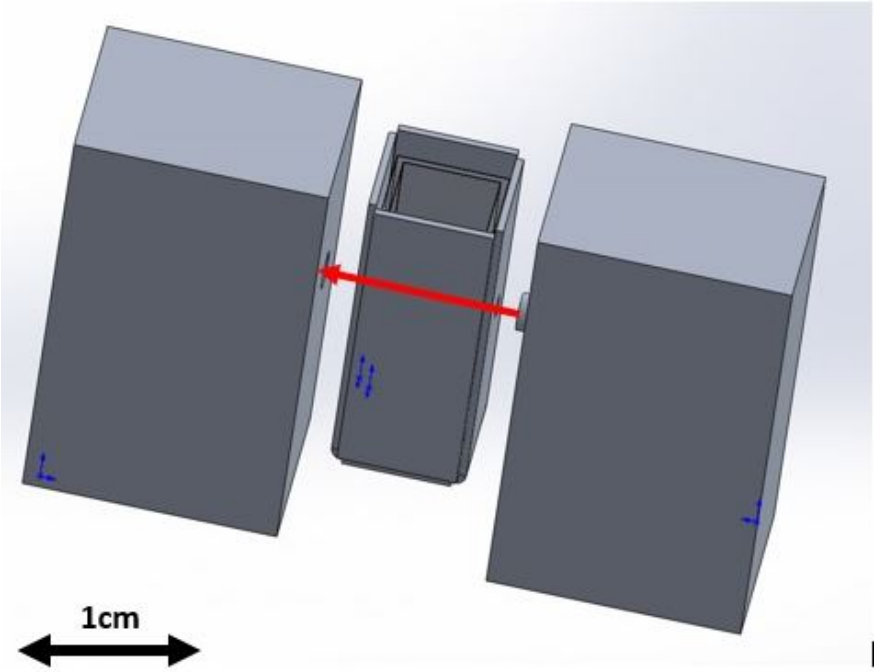

Fig. 6.4 Fluorescent measurement system including (from left to right) detector, cuvette, and emitter.

are placed immediately outside the cavity, they will be no more than 7.5cm apart so well within acceptable limits.

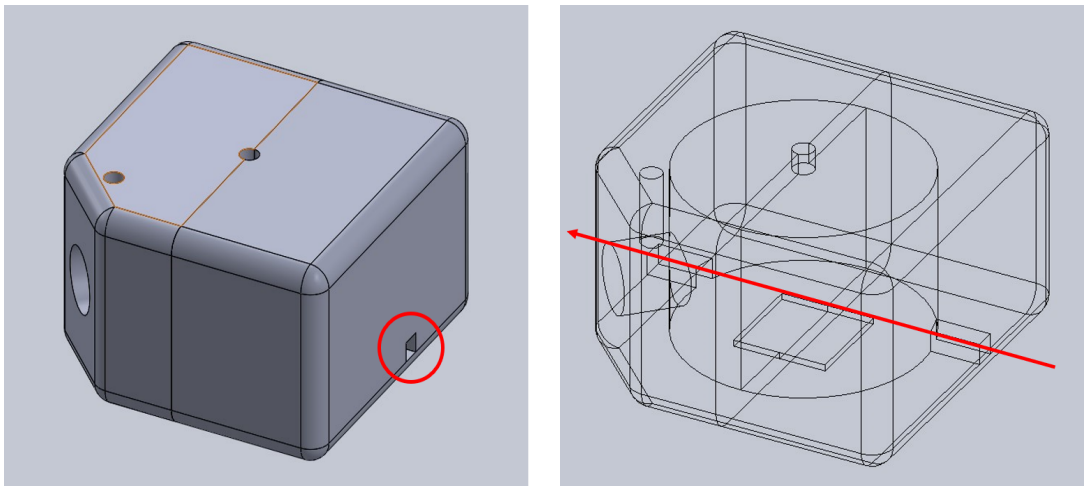

Fig. 6.5 Cavity design including holes for laser path and 1mm recess for cartridge housing and alignment.

The second is a 1mm recess set into the bottom of the cavity which allows the cartridge to sit inside and align with with the path of the laser (shown in fig 6.6).

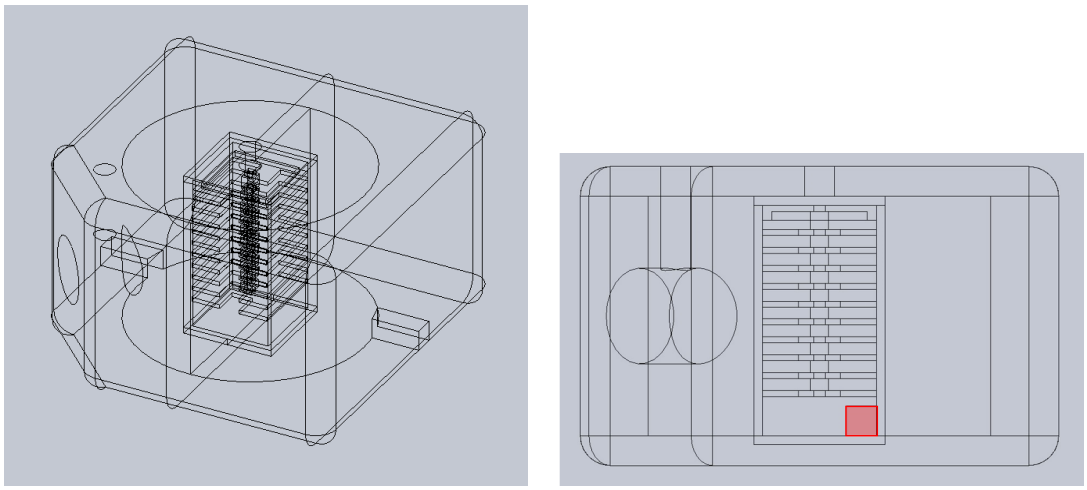

Fig. 6.6 Cavity design including holes for laser path and 1mm recess for cartridge housing and alignment.

An external magnetic system can then maneuver the magnetic nanoparticles with their DNA cargo to the corner of the cartridge in the path of the laser so the fluorescent reading is maximised, thus increasing the sensitivity of the detection. The build of this design is currently in progress. Its purpose is a proof-of-concept design for enabling the combination of microwave, magnetic, and fluorescent technologies and is, as of yet, untested. It has been pointed out that the debris from a patient sample would settle at the bottom of the cartridge making the fluorescent sensing more difficult with this approach. This problem can be easily rectified in a final design by the relocation of the fluorescent viewing port..

6.5 Magnetic Manipulation of Nanoparticles

In chapter 5, it is established that DNA can be released from target bacteria via microwave interaction with a sample (this action promoted by the interaction of electric fields with cartridge geometry). The previous section describes some possible techniques for the detection of target DNA require the nanoparticles to congregate at a specific point. The focus of the following section is the movement of magnetic nanoparticles within the cartridge. The premise of using magnets to separate magnetic nanoparticles from a mixture is common practise. The process usually follows the basic stages shown in fig 6.9 [163].

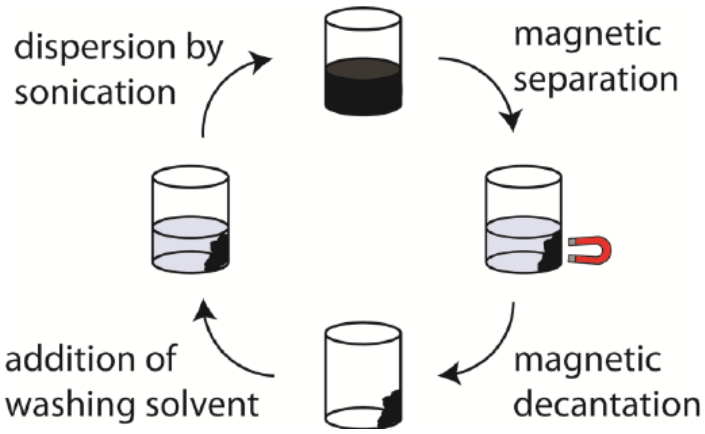

Fig. 6.7 General process of nanoparticle mixing and separation [170]

The specifics of each stage can differ greatly, for example the sonication stage is often replaced with the simple depression of a pipette plunger. This works very well for smaller volumes (up to a few ml) but larger volume pipettes usually do not cause the liquid to reach enough speed to make this a viable option, hence the use of sonication. This stage is imperative for the assay as maximisation of the amount of target DNA bound to the nanoparticles increases the sensitivity of the assay. Both pipetting and sonication are unsuitable for our proposed work as the former would require the cartridge to be removed from the cavity and opened, potentially causing cross contamination and/or infection of the user. Sonication would also be impractical as it would require the construction of an entire sonication module rendering the machine design undesirably bulky for a point of care assay. Sonication units

can also be very expensive and often require a probe which needs to be submerged in the sample to be sonicated, causing further problems with cross contamination (requiring a cleaning stage between each sample run). As for the magnetic separation stage, there are numerous designs for test tube racks with incorporated magnets to aid the mixing/separation process (such as the one shown in fig 6.10) [164].

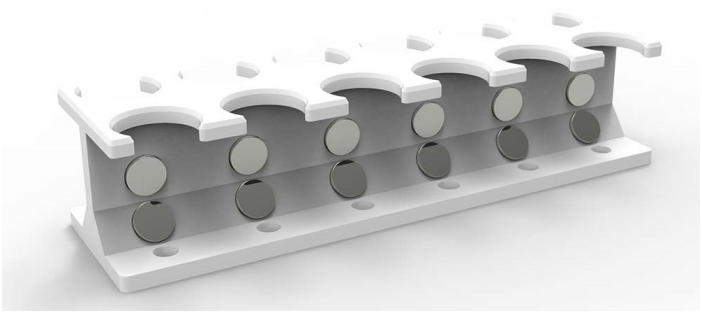

Fig. 6.8 Magnetic separating test tube rack (Ariumlab design) [171]

The tube rack has one or several permanent magnets (usually neodymium based) which attract the nanoparticles and cause them to "attach" to the side of the tube.

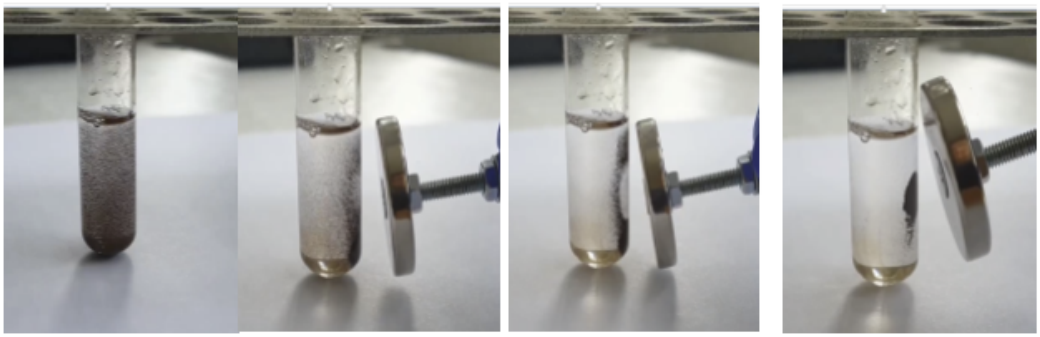

Fig. 6.9 Separating of Fe3O4/Ag sample from the solution by the external magnet

The supernatant can then be removed without disturbing the particles, and replaced with a solution which can be used to wash/re-suspend the particles (this step can be repeated for more effective washing). The benefit of using permanent magnets for this application relates to the size and shape of the sample and the relative strength of neodymium magnets. Small neodymium magnets, such as those used in these designs, are incredibly magnetically strong whilst being relatively small and light

(especially when compared to electromagnets), so can easily be incorporated into a small plastic tube rack without causing any structural problems. They are also powerful enough to pull the nanoparticles across the entire sample tube in a relatively short period of time. As magnetic pull strength follows (approximately) an inverse square law (as demonstrated by Coulomb's Law of Magnetic Force [165]) the ability of the magnets to move the nanoparticles within the sample decrease rapidly as distance between them increases (i.e. if the distance between the magnet and particle is twice as large then the force between them is approximately a quarter of the strength).

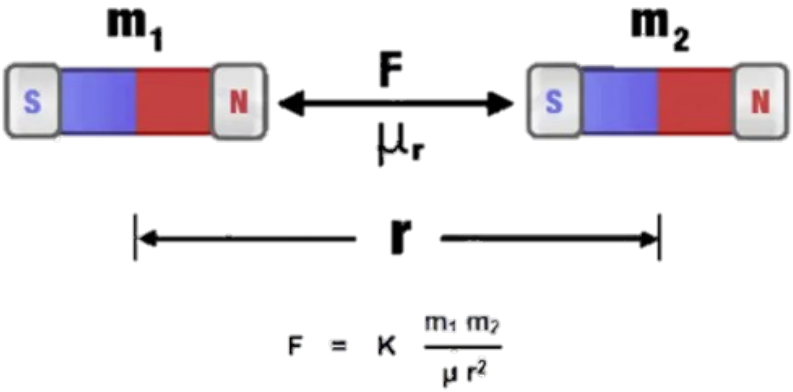

Fig. 6.10 Demonstration of Coulomb's Law of Magnetic attraction [172]

The relationship then follows that as the size of sample gets larger, the magnet strength must increase quadratically. The relationship between the physical size of the magnet and its strength is not quite as simple (this is related to material properties as well as the physical geometry of the magnet) but there does exist a strong linear correlation between the size of the magnet and its strength [166], defined by magnetic moment equations:

$$m = \frac{1}{\mu_0} B_r V \tag{6.1}$$

where:

- m is the net magnetic moment of the magnet
- B_r is the residual flux density,
- V is the volume of the magnet

- μ_0 is the permeability of vacuum

Logically then the stronger magnet needed for nanoparticles extraction from larger samples will need to be significantly physically larger, however, it is limited for this application by the strength of the magnetic field closest to the magnet. Our process requires the collection of magnetic nanoparticles with their DNA payload. With excessive force, it is conceivable that the act of pulling this structure through a viscous medium could cause the target DNA to detach from the nanoparticle, making them useless for the intended operation.

There is a commercial solution to this problem created by a company called SepMag [167]. They have constructed a system whereby electromagnets are strategically placed around the sample, allowing a constant force to be applied to the nanoparticles regardless of their position. These systems have been designed from test tube size (few μl) up to 20l (commercially available [168], but bespoke larger systems are also offered). Such a system could easily be incorporated with the current microwave cavity sample as the internal radius of the SepMag separator can be adjusted to house the entirety of the microwave cavity. The cavity is constructed of aluminium, which will not diminish the magnetic field applied. The SepMag system could then be modified to allow the microwave power input as well as a microfluidics output if required, or simply direct the particles to a position within the cartridge to allow for either the fluorescent or surface plasmon resonance approaches, so creating a fully integrated diagnostic.

Unfortunately, it was not possible to acquire a SepMag system due to time constraints and the considerable cost of the system. Hence, a more cost effective solution was proposed using general purpose electromagnets controlled using a micro-controller.

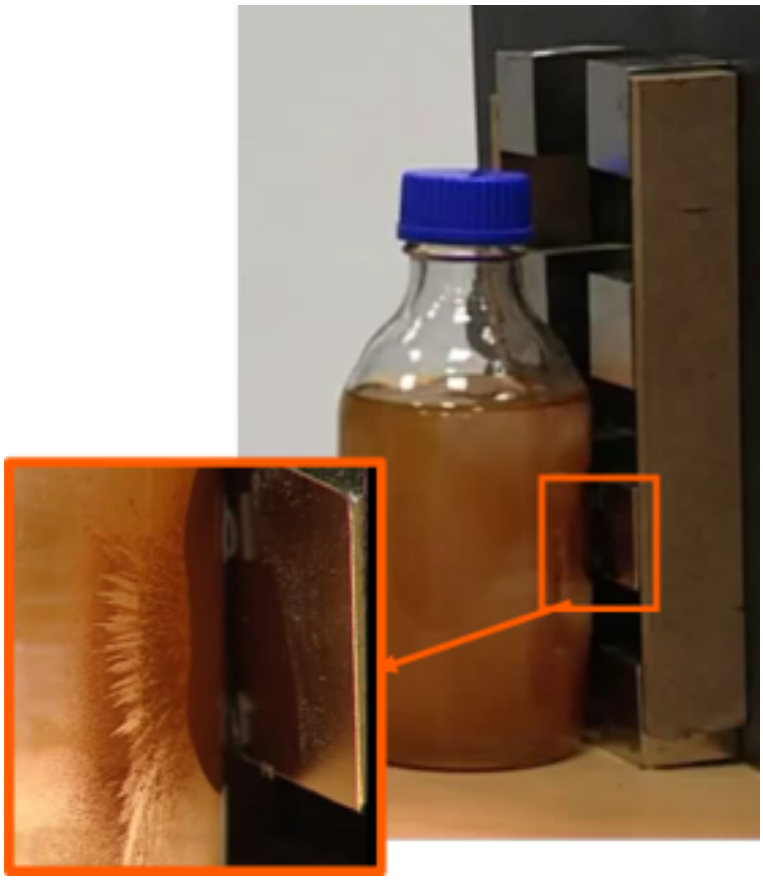

Fig. 6.11 Demonstration of the acceleration and clumping issues caused by a single magnetic source for separating nanoparticles from a solution

6.6 Integration and Experimentation of Electromagnetic Mixing System

Due to our inability to acquire a SepMag system, the use of general purpose electromagnets was explored. These electromagnets were placed either side of the 10ml cartridge and controlled using a micro-controller (in this case an Arduino Uno was used, diagram shown in fig 6.16, the implemented system shown in figs 6.17 and 6.18).

To aid in mixing the nanoparticles throughout the sample, the electromagnets were switched on and off in turn to draw the nanoparticles from one side of the cartridge to the other.

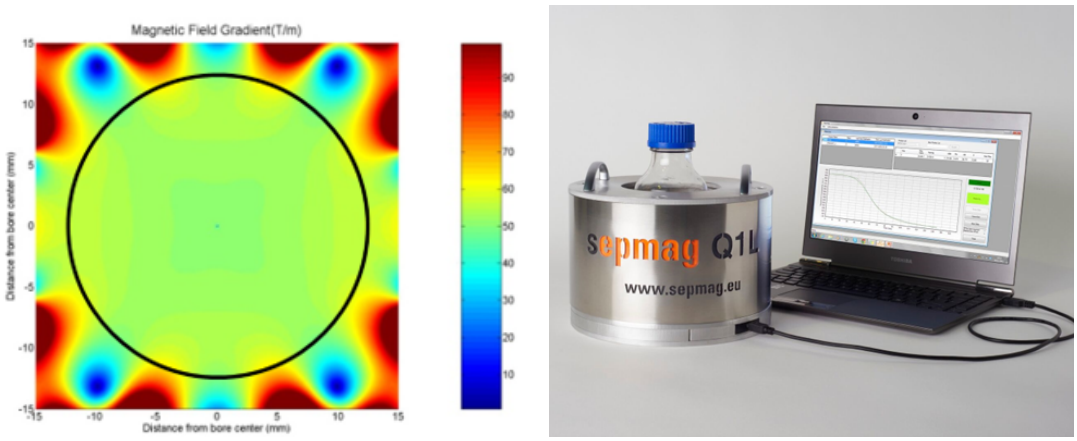

Fig. 6.12 COMSOL simulation of constant magnetic field gradient within SepMag system as a results of precise electromagnetic positioning (Left). Example of 1L SepMag separation system showing 1L sample inserted and external software control (Right) [174]

To assess the viability of this system initially, it was important to show that it was capable of moving nanoparticles in an acceptable amount of time (i.e. the magnetic mixing stage should not take significantly longer than the microwave excitation stage). The system was initially built using electromagnets listed with 25kg pull (commonly used in door and hatch mechanisms on machinery, in automated assembly lines, for robotics and the lifting and handling of ferrous materials) [169]. These are easy to obtain and inexpensive. The system test used "Dynabeads™ MyOne™ Streptavidin C1 (from Invitrogen)" as this mirrors the quantity used in the previous chapter to capture the target DNA released following microwave excitation. The time taken for the electromagnets to concentrate the particles to one side of the container was taken as the upper time limit for nanoparticle mixing (this figure is important as is represents amount of time needed to concentrate the nanoparticles for extraction after optimum mixing had occurred). For the initial test the nanoparticles were suspended in water and vortexed (for 5 seconds) to mix. The cartridge was then placed between the magnets (shown in fig. 6.14) and one magnet was switched on until all the nanoparticles had congregated to the wall nearest the magnet. This was assessed visually.

Using this system, the time taken for the nanoparticles to move to one side of the system was around 90 minutes (verified 3 times). This was considered to be too long to be effective in a real

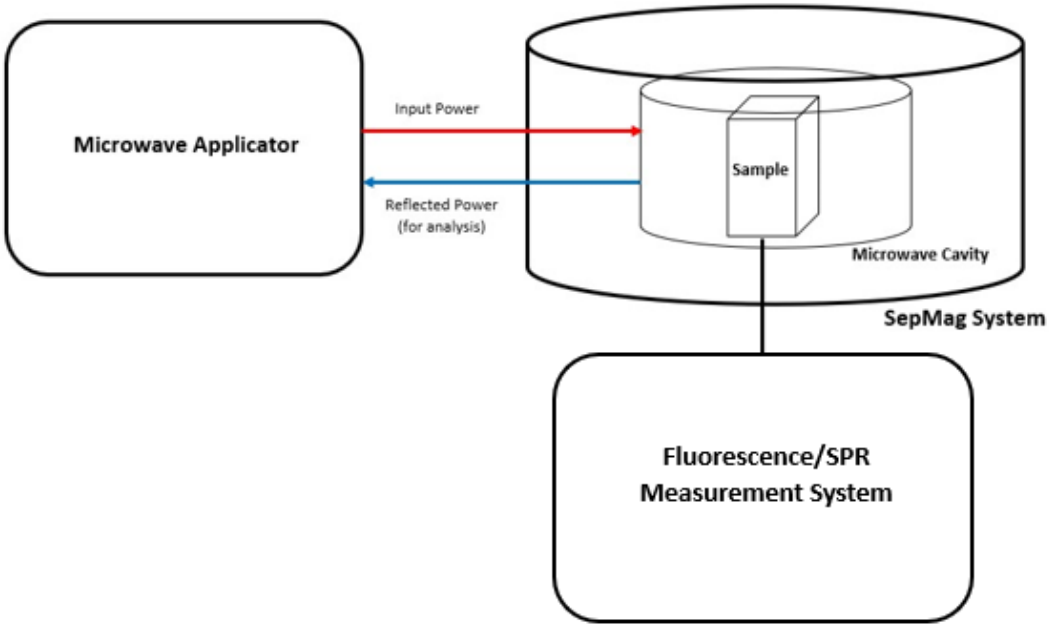

Fig. 6.13 Stages for complete integrated diagnosis using microwave applicator system transferring microwave power into microwave cavity containing the sample cartridge (stage 1). This sits within the magnetic system which is activated after the microwave application has finished and aids in DNA collection and separation (stage 2), either the fluorescent measurement system or SPR system can then be used to complete the diagnosis (stage 3).

world test scenario but it is useful to show that the system is at least someway effective. The next experiment was identical but used stronger electromagnets in an attempt to reduce the separation time. It is important to note that as electromagnets get stronger they become significantly more expensive and physically larger.

The magnets used in the following experiment were supplied by Bunting Magnetics [170]. The have a pull force of 90kg (giving a 3.6x increase from the previous models). They were also slightly larger (2 1/2 Inch x 1 1/2 Inch x 1 1/4 Inch) and around 3x more expensive (£63 per magnet, as opposed to £20 for the previous models). They are connected in the same way as the previous experiment and their implementation is shown in fig 6.18.

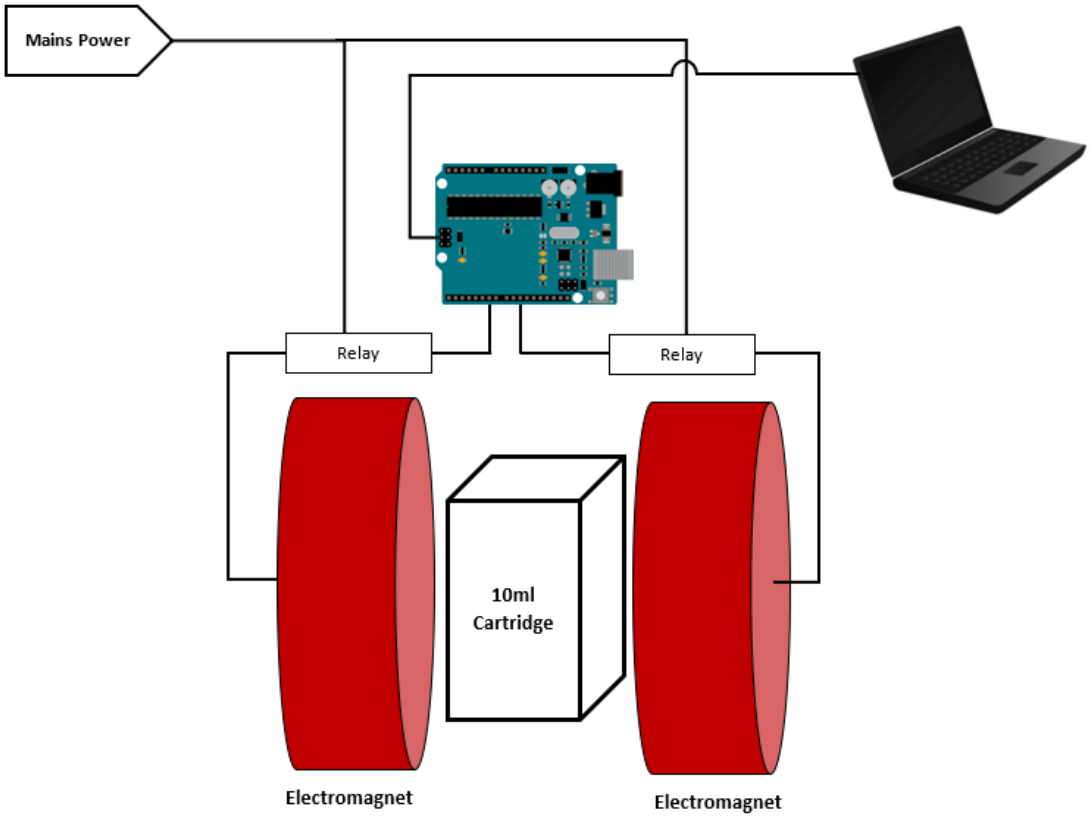

Fig. 6.14 Simple circuit diagram for experimental nanoparticle mixing hardware including micro-controller, programmed using an external computer.

Using these electromagnets the separation time was reduced to approximately 30 minutes (verified 3 times). While this was an improvement on the previous result, the system would certainly benefit from stronger magnets to produce a quicker separation time. Ideally the mixing and separation stage would be no longer than the microwave extraction stage (<10 minutes).

6.7 Magnetic Manipulation Future Work

Due to lack of time and funds it was not possible to take this system further during the course of the project, but the preliminary work described above provides a clear starting point for further

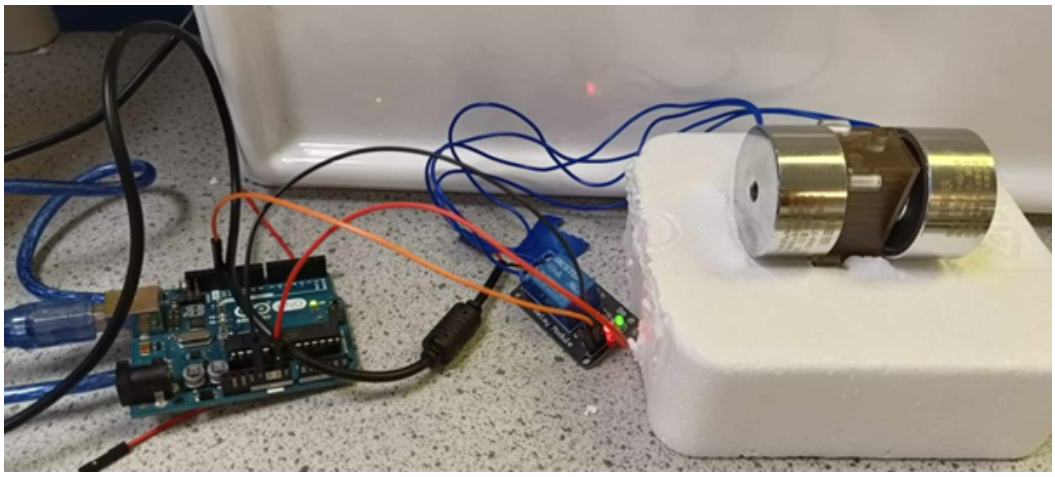

Fig. 6.15 Implementation of electromagnetic mixing system showing (from left to right) Arduino Uno microcontroller, relay switch, and electromagnets with cartridge.

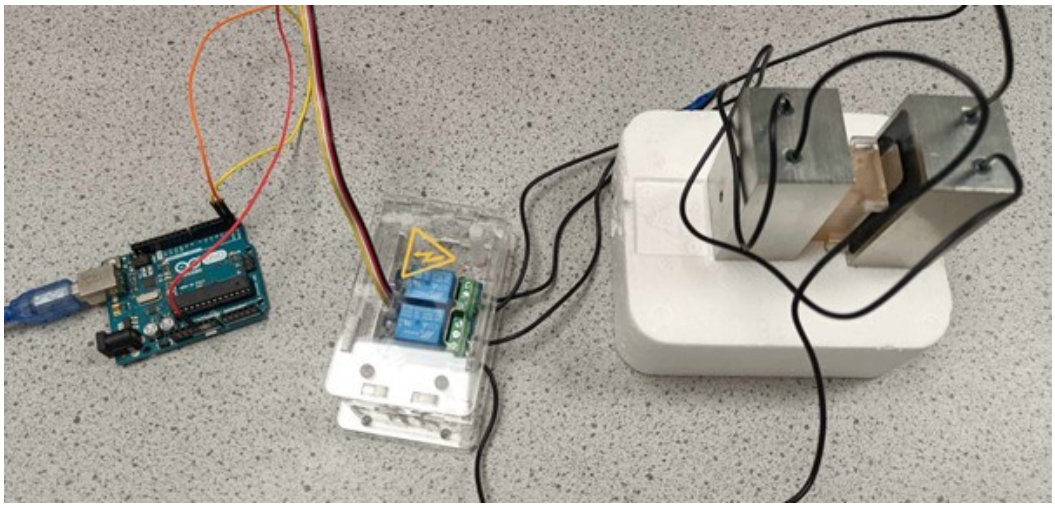

Fig. 6.16 Implementation of electromagnetic mixing system shown as before with the larger electromagnets [177].

development efforts. Further exploration should look at using stronger electromagnets to achieve quicker separation time.

Following this, experimentation should be undertaken to determine on how this mixing stage effects (improves) the yield of DNA collected from the sample, thereby improving the sensitivity of the assay.

6.8 General Discussion

The aim of this project was to develop a high volume (10ml) cartridge able to promote microwave interaction with aqueous samples containing mycobacteria. This cartridge had to be integrated into a microwave applicator system, the variables of which were to be optimised for promoting maximum DNA extraction from the bacteria.

In Chapter 3, the design and construction of a 10ml cartridge was described and it was shown that the addition of horizontal slats (perpendicular to the electric field) focused the microwave power into the sample. The design integrates with the existing microwave applicator system and facilitated rapid DNA release from mycobacteria with the modification of a few parameters.

In Chapter 4, the parameters used are optimised to maximise quantity of DNA extracted from a given sample. Using these parameters it was shown that maximum DNA release within the 10ml cartridge occurred following 6-8 minutes of applied 12W microwave power. This figure was uniform for water and simulated sputum based samples. The power level is the same as used for eppendorf tube samples but the excitation time was increased for 10ml samples. While the results for simulated sputum samples indicate that these microwave parameters can be used for real world samples (the viscosity is not a factor), the presence of cells and other host biological material could not be simulated so confirmation of efficacy using samples containing these will be necessary before the assay can be confirmed as effective for real world samples.

In Chapter 5, the ability of the cartridge design and optimised microwave application parameters in combination with magnetic nanoparticles functionalized with target specific DNA probes to detect the presence of a specific microorganism was confirmed. The method was able to distinguish *M.bov* from other mycobacterial species. While the current level of sensitivity of $10^4 CFU/ml$ (in both water and simulated sputum samples) is promising, it is still two orders of magnitude lower than other rapid diagnostic methods such as PCR ($10^2 CFU/ml$, [162]), although it does yield results in a shorter time. It should be possible to increase the sensitivity and reduce the time to a result by further optimising

the assay parameter, such as replacing the time consuming HRP detection step with a fluorescent probe.

Finally, chapter 6 explores the idea of an integrated diagnostic approach in the forms of SPR and fluorescent systems and the requirements for the integration of these into a single machine, thereby making the assay easier and more safe to use. The integration of all components into one device should also reduce the time required to detect a pathogen. The application of microcontroller controlled electromagnets was assessed as a method of maneuvering the DNA coated magnetic nanoparticles towards an aperture for the diagnostic stage. While "off the shelf" electromagnets proved insufficient, they demonstrated that the idea was sound but requires further time and expertise to implement in the context of an integrated system.

6.9 Final Conclusions

Overall this project achieved its principle aim of creating a 10ml cartridge for rapid DNA release. This cartridge was shown to have a sensitivity of $10^4 CFU/ml$ comparable to the previous eppendorf method. Using this approach, in combination with magnetic nanoparticles, it was possible to detect the presence of a particular microorganism in 10ml samples in 6-8 minutes. Preliminary studies in the laboratory suggest that by optimizing the signal reporting aspects of the system it should be able to increase the sensitivity and reduce the time to detection. The work described in this project has advantaged the development of a real-time, point of care assay for the rapid detection of pathogenic microorganisms in clinical samples.

6.10 Future Work

1. Develop a fully integrated system of diagnosis incorporating the microwave application, magnetic mixing and collection, and fluorescent diagnosis stages.

2. Explore the use of a bespoke magnetic system (such as the one described in Chapter 6) to precisely control the magnetic nanoparticles within the cartridge and avoid the loss of DNA via excessive acceleration.

3. Further enhance the sensitivity of the assay to align with the industry standard (PCR, $10^2 CFU/ml$).

4. Explore the idea of multiplexing using different wavelength fluorescent probes to search for different pathogen-specific DNA.

5. Condense the Microwave Applicator into a smaller package, allowing for inclusion of all stage systems into a desktop/portable device.

References

[1] S. Banik, S. Bandyopadhyay, and S. Ganguly. Bioeffects of microwave—a brief review. *Bioresource Technology*, 87(2):155–159, 2003.

[2] S. J. S. Ruiter, W. J. Heerink, and K. P. de Jong. Liver microwave ablation: a systematic review of various fda-approved systems. *Eur Radiol*, 29(8):4026–4035, 2019.

[3] R. L. Cazzato, G. de Rubeis, P. de Marini, D. Dalili, G. Koch, P. Auloge, J. Garnon, and A. Gangi. Percutaneous microwave ablation of bone tumors: a systematic review. *Eur Radiol*, 31(5):3530–3541, 2021.

[4] Z. Zhang, J. Wang, Y. Hu, and L. Wang. Microwaves, a potential treatment for bacteria: A review. *Front Microbiol*, 13, 2022.

[5] O. I. Ivaschuk, R. A. Jones, T. Ishida-Jones, W. Haggren, W. R. Adey, and J. L. Phillips. Exposure of nerve growth factor-treated pc12 rat pheochromocytoma cells to a modulated radiofrequency field at 836.55 mhz: effects on c-jun and c-fos expression. *Bioelectromagnetics*, 18(3):223–229, 1997.

[6] S. Koyama, Y. Takashima, T. Sakurai, Y. Suzuki, M. Taki, and J. Miyakoshi. Effects of 2.45 ghz electromagnetic fields with a wide range of sars on bacterial and hprt gene mutations. *J Radiat Res*, 48(1):69–75, 2007.

[7] T. A. Litovitz, L. M. Penafiel, J. M. Farrel, D. Krause, R. Meister, and J. M. Mullins. Bioeffects induced by exposure to microwaves are mitigated by superposition of elf noise. *Bioelectromagnetics*, 18(6):422–430, 1997.

[8] D. F. George, M. M. Bilek, and D. R. McKenzie. Non-thermal effects in the microwave induced unfolding of proteins observed by chaperone binding. *Bioelectromagnetics*, 29(4):324–330, 2008.

[9] Asher Shazman, Shimon Mizrahi, Uri Cogan, and Eyal Shimoni. Examining for possible non-thermal effects during heating in a microwave oven. *Food Chemistry*, 103(2):444–453, 2007.

[10] S. Y. Kim, E. K. Jo, H. J. Kim, K. Bai, and J. K. Park. The effects of high-power microwaves on the ultrastructure of bacillus subtilis. *Lett Appl Microbiol*, 47(1):35–40, 2008.

[11] Y. Shamis, A. Taube, N. Mitik-Dineva, R. Croft, R. J. Crawford, and E. P. Ivanova. Specific electromagnetic effects of microwave radiation on escherichia coli. *Appl Environ Microbiol*, 77(9):3017–22, 2011.

[12] P. W. French, M. Donnellan, and D. R. McKenzie. Electromagnetic radiation at 835 mhz changes the morphology and inhibits proliferation of a human astrocytoma cell line. *Bioelectrochemistry and Bioenergetics*, 43(1):13–18, 1997.

[13] A. Peinnequin, A. Piriou, J. Mathieu, V. Dabouis, C. Sebbah, R. Malabiau, and J. C. Debouzy. Non-thermal effects of continuous 2.45 ghz microwaves on fas-induced apoptosis in human jurkat t-cell line. *Bioelectrochemistry*, 51(2):157–161, 2000.

[14] R. B. Stagg, W. J. Thomas, R. A. Jones, and W. R. Adey. Dna synthesis and cell proliferation in c6 glioma and primary glial cells exposed to a 836.55 mhz modulated radiofrequency field. *Bioelectromagnetics*, 18(3):230–236, 1997.

[15] S. Velizarov, P. Raskmark, and S. Kwee. The effects of radiofrequency fields on cell proliferation are non-thermal. *Bioelectrochem Bioenerg*, 48(1):177–180, 1999.

[16] F. Taglia, L. Wang, C. H. Setser, N. Fernández-Tejero, B. R. McCord, and S. B. Lee. Development of a microwave-based extraction for forensic biological samples. *Forensic Sci Int Synerg*, 2022.

[17] D. C. Goodwin and S. B. Lee. Microwave miniprep of total genomic dna from fungi, plants, protists and animals for pcr. *Biotechniques*, 15(3):438–444, 1993.

[18] A. Cheyrou, C. Guyomarc'h, P. Jasserand, and P. Blouin. Improved detection of hbv dna by pcr after microwave treatment of serum. *Nucleic Acids Res*, 19(14):4006, 1991.

[19] Kadir Aslan, Yongxia Zhang, Stephen Hibbs, Les Baillie, Michael J. R. Previte, and Chris D. Geddes. Microwave-accelerated metal-enhanced fluorescence: application to detection of genomic and exosporium anthrax dna in <30 seconds. *Analyst*, 132:1130–1138, 2007.

[20] Kadir Aslan, Michael J. R. Previte, Yongxia Zhang, Theresa Gallagher, Les Baillie, and Chris D. Geddes. Extraction and detection of dna from bacillus anthracis spores and the vegetative cells within 1 min. *Analytical Chemistry*, 80(11):4125–32, 2008.

[21] L. T. Joshi, B. L. Mali, C. D. Geddes, and L. Baillie. Extraction and sensitive detection of toxins a and b from the human pathogen clostridium difficile in 40 seconds using microwave-accelerated metal-enhanced fluorescence. *PLoS One*, 9(8):e104334, 2014.

[22] Evans K. Ahortor, Dmitry Malyshev, Catrin F. Williams, Heungjae Choi, Jonathan Lees, Adrian Porch, and Les Baillie. The biological effect of 2.45GHz microwaves on the viability and permeability of bacterial and yeast cells. *Journal of Applied Physics*, 127(20):204902, 05 2020.

[23] Evans K. Ahortor. *The Rapid Detection of Drug Resistant Mycobacteria*. Thesis, Pharmacy, 2019.

[24] S. D. Lawn and A. I. Zumla. Tuberculosis. *Lancet*, 2011.

[25] Albert R. Zink, Christophe Sola, Udo Reischl, Waltraud Grabner, Nalin Rastogi, Hans Wolf, and Andreas G. Nerlich. Characterization of mycobacterium tuberculosis complex dnas from egyptian mummies by spoligotyping. *Journal of Clinical Microbiology*, 41(1):359–67, 2003.

[26] B. M. Rothschild, L. D. Martin, G. Lev, H. Bercovier, G. K. Bar-Gal, C. Greenblatt, H. Donoghue, M. Spigelman, and D. Brittain. Mycobacterium tuberculosis complex dna from an extinct bison dated 17,000 years before the present. *Clin Infect Dis*, 33(3):305–11, 2001.

[27] S. J. Jay, U. Kırbıyık, J. R. Woods, G. A. Steele, G. R. Hoyt, R. B. Schwengber, and P. Gupta. Modern theory of tuberculosis: culturomic analysis of its historical origin in europe and north america. *Int J Tuberc Lung Dis*, 22(11):1249–1257, 2018.

[28] Koch. R. [the etiology of tuberculosis by dr. robert koch. from the berliner klinische wochenschrift, volume 19 (1882)]. *Zentralbl Bakteriol Mikrobiol Hyg A Med Mikrobiol Infekt Parasitol*, 251(3):287–96, 1982.

[29] C. Wejse, P. Gustafson, J. Nielsen, V. F. Gomes, P. Aaby, P. L. Andersen, and M. Sodemann. Tbscore: Signs and symptoms from tuberculosis patients in a low-resource setting have predictive value and may be used to assess clinical course. *Scand J Infect Dis*, 40(2):111–20, 2008.

[30] R. M. Houben and P. J. Dodd. The global burden of latent tuberculosis infection: A re-estimation using mathematical modelling. *PLoS Med*, 3(10):e1002152, 2016.

[31] WHO. *Global tuberculosis control: surveillance, planning, financing: WHO report 2005*. World Health Organization, 2005.

[32] *Evidence-based Respiratory Medicine*. Wiley-Blackwell, Australia, 2005.

[33] T. Battaglioli, N. Rintiswati, A. Martin, K. R. Palupi, G. Bernaerts, B. Dwihardiani, R. A. Ahmad, F. Matthys, Y. Mahendradhata, and P. Van der Stuyft. Comparative performance of thin layer agar and löwenstein–jensen culture for diagnosis of tuberculosis. *Clinical Microbiology and Infection*, 19(11):E502–8, 2013.

[34] S. M. Katrak. Central nervous system tuberculosis. *J Neurol Sci*, 421:117278, 2021.

[35] B. M. Madison. Application of stains in clinical microbiology. *Biotechnic & Histochemistry*, 76(3):119–25, 2001.

[36] O Bolbot. Structure of tubercle bacillus, 2022.

[37] BrainKart. Ultrastructure of a bacterial cell, 2022.

[38] Richard Daniellou, Mateja Seničar, Ludovic Landemarre, Pierre Lafite, Svetlana Eliseeva, and Stephane Petoud. Galactofuranose-related enzymes: Challenges and hopes. *International Journal of Molecular Sciences*, 21(10):3465, 2020.

[39] jawad1212. Bacterial cell structure cell wall gram-positive bacteria gram-negative bacteria, 2018.

[40] Francis Xavier Emmanuel, Amie-Louise Seagar, Christine Doig, Alan Rayner, Pauline Claxton, and Ian Laurenson. Human and animal infections with mycobacterium microti, scotland. *Emerging infectious diseases*, 13(12):1924–7, 2007.

[41] Bouke C. de Jong, Martin Antonio, and Sebastien Gagneux. Mycobacterium africanum—review of an important cause of human tuberculosis in west africa. *PLOS Neglected Tropical Diseases*, 4(9):e744, 2010.

[42] Deb Cousins, Ricardo Bastida, Angel Cataldi, Viviana Quse, Sharon Redrobe Obe, Sue Dow, Padraig Duignan, Alan Murray, Christine Dupont, Niyaz Ahmed, Des Collins, W Butler, David Dawson, Diego Rodriguez, Julio Loureiro, María Romano, Alicia Alito, Martin Zumarraga, and Amelia Bernardelli. Tuberculosis in seals caused by a novel member of the mycobacterium tuberculosis complex: Mycobacterium pinnipedii sp. nov. *International journal of systematic and evolutionary microbiology*, 53:1305–14, 10 2003.

[43] Jean Miltgen, Marc Morillon, Jean-Louis Koeck, Anne Varnerot, Jean-François Briant, Gilbert Nguyen, Denis Verrot, Daniel Bonnet, and Véronique Vincent. Two cases of pulmonary tuberculosis caused by mycobacterium tuberculosis subsp. canetti. *Emerging infectious diseases*, 8(11):1350–2, 2002.

[44] S. Mostowy, A. Onipede, S. Gagneux, S. Niemann, K. Kremer, E. P. Desmond, M. Kato-Maeda, and M. Behr. Genomic analysis distinguishes mycobacterium africanum. *J Clin Microbiol*, 42(8):3594–9, 2004.

[45] S. Mostowy, J. Inwald, S. Gordon, C. Martin, R. Warren, K. Kremer, D. Cousins, and M. A. Behr. Revisiting the evolution of mycobacterium bovis. *J Bacteriol*, 187(18):6386–95, 2005.

[46] I. Schiller, B. Oesch, H. M. Vordermeier, M. V. Palmer, B. N. Harris, K. A. Orloski, B. M. Buddle, T. C. Thacker, K. P. Lyashchenko, and W. R. Waters. Bovine tuberculosis: a review of current and emerging diagnostic techniques in view of their relevance for disease control and eradication. *Transbound Emerg Dis*, 57(4):205–20, 2010.

[47] R. de la Rua-Domenech, A. T. Goodchild, H. M. Vordermeier, R. G. Hewinson, K. H. Christiansen, and R. S. Clifton-Hadley. Ante mortem diagnosis of tuberculosis in cattle: a review of the tuberculin tests, gamma-interferon assay and other ancillary diagnostic techniques. *Res Vet Sci*, 2006.

[48] P. Torres-Gonzalez, O. Soberanis-Ramos, A. Martinez-Gamboa, B. Chavez-Mazari, M. T. Barrios-Herrera, M. Torres-Rojas, L. P. Cruz-Hervert, L. Garcia-Garcia, M. Singh, A. Gonzalez-Aguirre, A. Ponce de Leon-Garduño, J. Sifuentes-Osornio, and M. Bobadilla-Del-Valle. Prevalence of latent and active tuberculosis among dairy farm workers exposed to cattle infected by mycobacterium bovis. *PLoS Negl Trop Dis*, 68(7):704–718, 2013.

[49] Ní Bhuachalla D, L. A. Corner, S. J. More, and E. Gormley. The role of badgers in the epidemiology of mycobacterium bovis infection (tuberculosis) in cattle in the united kingdom and the republic of ireland: current perspectives on control strategies. *Vet Med (Auckl)*, 6:27–38, 2015.

[50] S. Sunder, P. Lanotte, S. Godreuil, C. Martin, M. L. Boschiroli, and J. M. Besnier. Human-to-human transmission of tuberculosis caused by mycobacterium bovis in immunocompetent patients. *J Clin Microbiol*, 47(4):1249–51, 2009.

[51] E Uberoi. Bovine tuberculosis statistics: Great britain, 2019.

[52] S. M. Batt, D. E. Minnikin, and G. S. Besra. The thick waxy coat of mycobacteria, a protective layer against antibiotics and the host's immune system. *Biochem J*, 477(10):1983–2006, 2020.

[53] Vincent Jarlier and Hiroshi Nikaido. Mycobacterial cell wall: Structure and role in natural resistance to antibiotics. *FEMS Microbiology Letters*, 123(1-2):11–8, 1994.

[54] P. J. Brennan and H. Nikaido. The envelope of mycobacteria. *Annu Rev Biochem*, 64:29–63, 1995.

[55] Eila Torvinen, Pertti Martikainen, Marja Räisänen, and Marja-Leena Katila. Mycobacteria in boreal coniferous forest soils. *FEMS Microbiology Ecology*, 23:325 – 332, 01 2006.

[56] JO Falkinham 3rd. Epidemiology of infection by nontuberculous mycobacteria. *Clinical microbiology reviews*, 9(2):177–215, 1996.

[57] J. C. Lagier, S. Edouard, I. Pagnier, O. Mediannikov, M. Drancourt, and D. Raoult. Current and past strategies for bacterial culture in clinical microbiology. *Clin Microbiol Rev*, 28(1):208–36, 2015.

[58] Stephen K. Tyring, Omar Lupi, and Ulrich R. Hengge, editors. *22 - Mycobacteria*, book section 22, pages 150–250. Elsevier, 2017.

[59] R. Nambiar, S. Chatellier, N. Bereksi, A. van Belkum, N. Singh, B. Barua, A. Shetty, and C. Rodrigues. Evaluation of mycotube, a modified version of lowenstein–jensen (lj) medium, for efficient recovery of mycobacterium tuberculosis (mtb). *European Journal of Clinical Microbiology & Infectious Diseases*, 36(10):1981–1988, 2017.

[60] R. Wallace, J. Glassroth, D. Griffith, J. Oliver, K. Cook, and F Gordin. Diagnosis and treatment of disease caused by nontuberculous mycobacteria. *American Journal of Respiratory and Critical Care Medicine*, 156(2):1 – 25, 1997.

[61] Mary A. De Groote and Gwen Huitt. Infections due to rapidly growing mycobacteria. *Clinical Infectious Diseases*, 42(12):1756–63, 2006.

[62] J. M. Reyrat and D. Kahn. Mycobacterium smegmatis: an absurd model for tuberculosis? *Trends Microbiol*, 2001.

[63] A. K. Singh and J. M. Reyrat. Laboratory maintenance of mycobacterium smegmatis. *Curr Protoc Microbiol*, Chapter 10:Unit10C.1, 2009.

[64] S. H. Lee. Tuberculosis infection and latent tuberculosis. *Tuberc Respir Dis (Seoul)*, 79(4):201–206, 2016.

[65] M. Pai, M. A. Behr, D. Dowdy, K. Dheda, M. Divangahi, C. C. Boehme, A. Ginsberg, S. Swaminathan, M. Spigelman, H. Getahun, D. Menzies, and M. Raviglione. Tuberculosis. *Nat Rev Dis Primers*, 2:16076, 2016.

[66] A. C. Nachiappan, K. Rahbar, X. Shi, E. S. Guy, Jr. Mortani Barbosa, E. J., G. S. Shroff, D. Ocazionez, A. E. Schlesinger, S. I. Katz, and M. M. Hammer. Pulmonary tuberculosis: Role of radiology in diagnosis and management. *Radiographics*, 37(1):52–72, 2017.

[67] Centers for Disease Control and Prevention. How tb spreads, 2022.

[68] R. de la Rua-Domenech. Human mycobacterium bovis infection in the united kingdom: Incidence, risks, control measures and review of the zoonotic aspects of bovine tuberculosis. *Tuberculosis (Edinb)*, 81(2):190–210, 2006.

[69] Centers for Disease Control and Prevention. Mycobacterium bovis (bovine tuberculosis) in humans, 2011.

[70] Armstrong. J. Grazing and pasture management for cattle, 2021.

[71] M. Albrecht-Seidel, R. Carrasco, C. Laithier, M. Sienkiewicz, and P. et al. Thomas. European guide for good hygiene practices in the production of artisanal cheese and dairy products, 2016.

[72] L. P. Ormerod. Multidrug-resistant tuberculosis (mdr-tb): epidemiology, prevention and treatment. *Br Med Bull*, 73-74:17–24, 2005.

[73] N. S. Shah, A. Wright, G. H. Bai, L. Barrera, F. Boulahbal, N. Martín-Casabona, F. Drobniewski, C. Gilpin, M. Havelková, R. Lepe, R. Lumb, B. Metchock, F. Portaels, M. F. Rodrigues, S. Rüsch-Gerdes, A. Van Deun, V. Vincent, K. Laserson, C. Wells, and J. P. Cegielski. Worldwide emergence of extensively drug-resistant tuberculosis. *Emerg Infect Dis*, 13(3):380–7, 2007.

[74] S. H. Blaas, R. Mütterlein, J. Weig, A. Neher, B. Salzberger, N. Lehn, and L. Naumann. Extensively drug resistant tuberculosis in a high income country: a report of four unrelated cases. *BMC Infect Dis*, 8:60, 2008.

[75] A. A. Velayati, M. R. Masjedi, P. Farnia, P. Tabarsi, J. Ghanavi, A. H. ZiaZarifi, and S. E. Hoffner. Emergence of new forms of totally drug-resistant tuberculosis bacilli: super extensively drug-resistant tuberculosis or totally drug-resistant strains in iran. *Chest*, 136(2):420–425, 2009.

[76] G. B. Migliori, J. Ortmann, E. Girardi, G. Besozzi, C. Lange, D. M. Cirillo, M. Ferrarese, G. De Iaco, A. Gori, and M. C. Raviglione. Extensively drug-resistant tuberculosis, italy and germany. *Emerg Infect Dis*, 13(5):780–2, 2007.

[77] Z. F. Udwadia, R. A. Amale, K. K. Ajbani, and C. Rodrigues. Totally drug-resistant tuberculosis in india. *Clin Infect Dis*, 54(4):579–81, 2012.

[78] M. A. Cortes, R. Nessar, and A. K. Singh. Laboratory maintenance of mycobacterium abscessus. *Curr Protoc Microbiol*, Chapter 10:Unit 10D.1, 2010.

[79] M. R. Lee, W. H. Sheng, C. C. Hung, C. J. Yu, L. N. Lee, and P. R. Hsueh. Mycobacterium abscessus complex infections in humans. *Emerg Infect Dis*, 21(9):1638–46, 2015.

[80] Y. Matsumoto, T. Kinjo, D. Motooka, D. Nabeya, N. Jung, K. Uechi, T. Horii, T. Iida, J. Fujita, and S. Nakamura. Comprehensive subspecies identification of 175 nontuberculous mycobacteria species based on 7547 genomic profiles. *Emerg Microbes Infect*, 8(1):1043–1053, 2019.

[81] J. Esteban and A. Ortiz-Pérez. Current treatment of atypical mycobacteriosis. *Expert Opin Pharmacother*, 10(17):2787–99, 2009.

[82] Rainer Döfflnger, Emmanuelle Jouanguy, Stéphanie Dupuis, Marie-Claude Fondanèche, Jean-Louis Stephan, Jean-François Emile, Salma Lamhamedi-Cherradi, Frédéric Altare, Annaïck Pallier, Gabriela Barcenas-Morales, Edgar Meinl, Christopher Krause, Sidney Pestka, Robert D. Schreiber, Francesco Novelli, and Jean-Laurent Casanova. Partial interferon-γ receptor signaling chain deficiency in a patient with bacille calmette-guérin and mycobacterium abscessus infection. *The Journal of Infectious Diseases*, 181(1):379–84, 2000.

[83] R. Nessar, E. Cambau, J. M. Reyrat, A. Murray, and B. Gicquel. Mycobacterium abscessus: a new antibiotic nightmare. *J Antimicrob Chemother*, 9(10):472–4, 2012.

[84] Y. Nishiuchi, T. Iwamoto, and F. Maruyama. Infection sources of a common non-tuberculous mycobacterial pathogen, mycobacterium avium complex. *Front Med (Lausanne)*, 4:27, 2017.

[85] E. Abston and H. Farber. Pulmonary cavity from mycobacterium malmoense in an hiv-infected patient: Complicated by bronchopleural fistula. *Open Forum Infect Dis*, 5(2):ofy023, 2018.

[86] G. K. Siberry, M. J. Abzug, S. Nachman, M. T. Brady, K. L. Dominguez, E. Handelsman, L. M. Mofenson, S. Nesheim, Health National Institutes of, Control Centers for Disease, Prevention, H. I. V. Medicine Association of the Infectious Diseases Society of America, Society Pediatric Infectious Diseases, and Pediatrics American Academy of. Guidelines for the prevention and treatment of opportunistic infections in hiv-exposed and hiv-infected children: recommendations from the national institutes of health, centers for disease control and prevention, the hiv medicine association of the infectious diseases society of america, the pediatric infectious diseases society, and the american academy of pediatrics. *Pediatr Infect Dis J*, 32 Suppl 2(0 2):i–KK4, 2013.

[87] M. Moore and J. B. Frerichs. An unusual acid-fast infection of the knee with subcutaneous, abscess-like lesions of the gluteal region; report of a case with a study of the organism, mycobacterium abscessus, n. sp. *J Invest Dermatol*, 20(2):133–69, 1953.

[88] S. Kusunoki and T. Ezaki. Proposal of mycobacterium peregrinum sp. nov., nom. rev., and elevation of mycobacterium chelonae subsp. abscessus (kubica et al.) to species status: Mycobacterium abscessus comb. nov. *Int J Syst Bacteriol*, 42(2):240–5, 1992.

[89] G. Degiacomi, J. C. Sammartino, L. R. Chiarelli, O. Riabova, V. Makarov, and M. R. Pasca. Mycobacterium abscessus, an emerging and worrisome pathogen among cystic fibrosis patients. *Int J Mol Sci*, 20(23):5868, 2019.

[90] S. K. Anisowicz, S. K. Welsh, and J. E. Gross. Eradication of mycobacterium abscessus pulmonary infection in a child with idiopathic bronchiectasis. *Glob Pediatr Health*, 3:2333794x16670985, 2016.

[91] M. M. Johnson and J. A. Odell. Nontuberculous mycobacterial pulmonary infections. *J Thorac Dis*, 6(3):210–20, 2014.

[92] Luis G. Tulloch. *24 - Nontuberculous Mycobacterial Skin Infections*, book section 24, pages 100–200. W.B. Saunders, Philadelphia, 2012.

[93] Alan A. Schmalstig, Kimberley M. Zorn, Sebastian Murcia, Andrew Robinson, Svetlana Savina, Elena Komarova, Vadim Makarov, Miriam Braunstein, and Sean Ekins. Mycobacterium abscessus drug discovery using machine learning. *Tuberculosis*, 132:102168, 2022.

[94] Nils Wetzstein, Margo Diricks, A. Kohl Thomas, A. Wichelhaus Thomas, Sönke Andres, Laura Paulowski, Carsten Schwarz, Astrid Lewin, Jan Kehrmann, C. Kahl Barbara, Karl Dichtl, Christian Hügel, Olaf Eickmeier, Christina Smaczny, Annika Schmidt, Stefan Zimmermann, Lutz Nährlich, Sylvia Hafkemeyer, Stefan Niemann, P. Maurer Florian, and Michael Hogardt. Molecular epidemiology of mycobacterium abscessus isolates recovered from german cystic fibrosis patients. *Microbiology Spectrum*, 10(4):e0171422, 2022.

[95] G. Degiacomi, J. C. Sammartino, L. R. Chiarelli, O. Riabova, V. Makarov, and M. R. Pasca. Mycobacterium abscessus, an emerging and worrisome pathogen among cystic fibrosis patients. *Int J Mol Sci*, 20(23):5868, 2019.

[96] V. Chaturvedi, N. Dwivedi, R. P. Tripathi, and S. Sinha. Evaluation of mycobacterium smegmatis as a possible surrogate screen for selecting molecules active against multi-drug resistant mycobacterium tuberculosis. *J Gen Appl Microbiol*, 53(6):333–7, 2007.

[97] A. Bohsali, H. Abdalla, K. Velmurugan, and V. Briken. The non-pathogenic mycobacteria m. smegmatis and m. fortuitum induce rapid host cell apoptosis via a caspase-3 and tnf dependent pathway. *BMC Microbiol*, 10:237, 2010.

[98] Abhinav Dey, Amit Kumar Verma, and Dipankar Chatterji. Role of an rna polymerase interacting protein, msrbpa, from mycobacterium smegmatis in phenotypic tolerance to rifampicin. *Microbiology*, 156(Pt 3):873–883, 2010.

[99] Priyanka Agrawal, Sandeep Miryala, and Umesh Varshney. Use of mycobacterium smegmatis deficient in adp-ribosyltransferase as surrogate for mycobacterium tuberculosis in drug testing and mutation analysis. *PLOS ONE*, 10(4):e0122076, 2015.

[100] Krishna Kurthkoti, Pradeep Kumar, Ruchi Jain, and Umesh Varshney. Important role of the nucleotide excision repair pathway in mycobacterium smegmatis in conferring protection against commonly encountered dna-damaging agents. *Microbiology*, 154(Pt 9):2776–2785, 2008.

[101] Junli Li, Lingjun Zhan, and Chuan Qin. The double-sided effects of mycobacterium bovis bacillus calmette–guérin vaccine. *npj Vaccines*, 6(1):14, 2021.

[102] Marcos Gustavo Araujo Schwarz, Deborah Antunes, Paloma Rezende Corrêa, Antônio José da Silva-Gonçalves, Wladimir Malaga, Ernesto Raul Caffarena, Christophe Guilhot, and Leila Mendonça-Lima. Mycobacterium tuberculosis and m. bovis bcg moreau fumarate reductase operons produce different polypeptides that may be related to non-canonical functions. *Frontiers in Microbiology*, 11:624121, 2021.

[103] R. Waked, J. Choucair, N. Chehata, E. Haddad, and G. Saliba. Intravesical bacillus calmette-guérin (bcg) treatment's severe complications: A single institution review of incidence, presentation and treatment outcome. *Journal of Clinical Tuberculosis and Other Mycobacterial Diseases*, 19:100149, 2020.

[104] World Health Organisation. Who consolidated guidelines on tuberculosis: module 4: treatment: drug-resistant tuberculosis treatment, 2020.

[105] Tankeshwar. A. Ziehl-neelsen technique-afb staining, 2022.

[106] Kamran Siddiqi, Marie-Laurence Lambert, and John Walley. Clinical diagnosis of smear-negative pulmonary tuberculosis in low-income countries: the current evidence. *The Lancet Infectious Diseases*, 3(5):288–96, 2003.

[107] Centre for Disease Control and Prevention. Core curriculum on tuberculosis: What the clinician should know, 2021.

[108] B. J. Marais, W. Brittle, K. Painczyk, A. C. Hesseling, N. Beyers, E. Wasserman, D. van Soolingen, and R. M. Warren. Use of light-emitting diode fluorescence microscopy to detect acid-fast bacilli in sputum. *Clin Infect Dis*, 2008.

[109] Basem Abbas Al Ubaidi. The radiological diagnosis of pulmonary tuberculosis (tb) in primary care. *Family Medicine and Disease Prevention*, 4:73, 2018.

[110] E. Mortaz, M. R. Masjedi, S. Matroodi, A. Abedini, A. Kiani, D. Soroush, and I. M. Adcock. Concomitant patterns of tuberculosis and sarcoidosis. *Tanaffos*, 12(4):6–9, 2013.

[111] R. Piccazzo, F. Paparo, and G. Garlaschi. Diagnostic accuracy of chest radiography for the diagnosis of tuberculosis (tb) and its role in the detection of latent tb infection: a systematic review. *J Rheumatol Suppl*, 91:32–40, 2014.

[112] A. C. Nachiappan, K. Rahbar, X. Shi, E. S. Guy, Jr. Mortani Barbosa, E. J., G. S. Shroff, D. Ocazionez, A. E. Schlesinger, S. I. Katz, and M. M. Hammer. Pulmonary tuberculosis: Role of radiology in diagnosis and management. *Radiographics*, 37(1):52–72, 2017.

[113] Patricia T Kent. *Public health mycobacteriology: a guide for the level III laboratory*. US Department of Health and Human Services, Public Health Service, Centers . . . , 1985.

[114] Emily Spellman Sheen, Ellen H Lee, and Douglas E Berg. Rapid, efficient detection and drug susceptibility testing of mycobacterium tuberculosis in sputum by microscopic observation of broth cultures. *J. Clin. Microbiol*, 38(3):1203, 2000.

[115] Louis Grandjean and David A. J. Moore. Tuberculosis in the developing world: recent advances in diagnosis with special consideration of extensively drug-resistant tuberculosis. *Current opinion in infectious diseases*, 21(5):454–61, 2008.

[116] D. Shingadia and V. Novelli. Diagnosis and treatment of tuberculosis in children. *Lancet Infect Dis*, 3(10):624–32, 2003.

[117] T. McWilliams, A. U. Wells, A. C. Harrison, S. Lindstrom, R. J. Cameron, and E. Foskin. Induced sputum and bronchoscopy in the diagnosis of pulmonary tuberculosis. *Thorax*, 57(12):1010–4, 2002.

[118] A. Trajman, E. Silva J. R. Lapa, M. Dalcolmo, and J. E. Golub. Pulmonary tuberculosis. *Pulm Med*, 2013:645747, 2013.

[119] R. E. Huebner, M. F. Schein, and Jr. Bass, J. B. The tuberculin skin test. *Clin Infect Dis*, 17(6):968–75, 1993.

[120] G Diaz. Tuberculin Skin Test (Positive Mantoux Test) Result. https://www.grepmed.com/images/2645/interpretation-tuberculosis-thresholds-induration-tuberculin, 2018. [Accessed 05-May-2023].

[121] J. Pouchot, A. Grasland, C. Collet-Gaudillat, Joel Coste, J. Esdaile, and Philippe Vinceneux. Reliability of tuberculin skin test measurement. *Annals of internal medicine*, 126(3):210–4, 1997.

[122] N. Banaei, R. L. Gaur, and M. Pai. Interferon gamma release assays for latent tuberculosis: What are the sources of variability? *J Clin Microbiol*, 54(4):845–50, 2016.

[123] Marie P Gomez, Simon Donkor, Ifedayo M Adetifa, Martin OC Ota, and Jayne S Sutherland. Analysis of lam and 38 kda antibody levels for diagnosis of tb in a case-control study in west africa. *International Scholarly Research Notices*, 2012, 2012.

[124] Toru Mori, Mitsunori Sakatani, Fumio Yamagishi, Tetsuya Takashima, Yoshiko Kawabe, Keiji Nagao, Eriko Shigeto, Nobuyuki Harada, Satoshi Mitarai, Masaji Okada, Katsuhiro Suzuki, Yoshikazu Inoue, Kazunari Tsuyuguchi, Yuka Sasaki, Gerald H. Mazurek, and Izuo Tsuyuguchi. Specific detection of tuberculosis infection. *American Journal of Respiratory and Critical Care Medicine*, 170(1):59–64, 2004.

[125] M. M. Floyd, V. A. Silcox, Jr. Jones, W. D., W. R. Butler, and J. O. Kilburn. Separation of mycobacterium bovis bcg from mycobacterium tuberculosis and mycobacterium bovis by using high-performance liquid chromatography of mycolic acids. *J Clin Microbiol*, 30(5):1327–30, 1992.

[126] W. R. Butler, Jr. Jost, K. C., and J. O. Kilburn. Identification of mycobacteria by high-performance liquid chromatography. *J Clin Microbiol*, 29(11):2468–72, 1991.

[127] P. S. Duffey, L. S. Guthertz, and G. C. Evans. Improved rapid identification of mycobacteria by combining solid-phase extraction with high-performance liquid chromatography analysis of bactec cultures. *J Clin Microbiol*, 34(8):1939–43, 1996.

[128] L. Thibert and S. Lapierre. Routine application of high-performance liquid chromatography for identification of mycobacteria. *J Clin Microbiol*, 31(7):1759–63, 1993.

[129] J. B. Brooks, M. I. Daneshvar, R. L. Haberberger, and I. A. Mikhail. Rapid diagnosis of tuberculous meningitis by frequency-pulsed electron-capture gas-liquid chromatography detection of carboxylic acids in cerebrospinal fluid. *Journal of Clinical Microbiology*, 28(5):989–97, 1990.

[130] Pascal Craw and Wamadeva Balachandran. Isothermal nucleic acid amplification technologies for point-of-care diagnostics: a critical review. *Lab on a Chip*, 12:2469–86, 2012.

[131] S. Cheng, C. Fockler, W. M. Barnes, and R. Higuchi. Effective amplification of long targets from cloned inserts and human genomic dna. *Proceedings of the National Academy of Sciences of the United States of America*, 91(12):5695–9, 1994.

[132] Society for Mucosal Immunology. Pcr: The polymerase chain reaction, 2014.

[133] A. Chien, D. B. Edgar, and J. M. Trela. Deoxyribonucleic acid polymerase from the extreme thermophile thermus aquaticus. *Journal of bacteriology*, 127(3):1550–7, 1976.

[134] F. C. Lawyer, S. Stoffel, R. K. Saiki, S. Y. Chang, P. A. Landre, R. D. Abramson, and D. H. Gelfand. High-level expression, purification, and enzymatic characterization of full-length thermus aquaticus dna polymerase and a truncated form deficient in 5' to 3' exonuclease activity. *PCR Methods Appl*, 2(4):275–87, 1993.

[135] Stephen A. Bustin. How to speed up the polymerase chain reaction. *Biomolecular Detection and Quantification*, 12:10–14, 2017.

[136] Savita Kulkarni, P. Singh, Aafreen Memon, Gita Nataraj, Swapna Kanade, Rohini Kelkar, and M. G. R. Rajan. An in-house multiplex pcr test for the detection of mycobacterium tuberculosis, its validation & comparison with a single target tb-pcr kit. *The Indian journal of medical research*, 135(5):788–94, 2012.

[137] T. Iwamoto, T. Sonobe, and K. Hayashi. Loop-mediated isothermal amplification for direct detection of mycobacterium tuberculosis complex, m. avium, and m. intracellulare in sputum samples. *J Clin Microbiol*, 41(6):2616–22, 2003.

[138] X. Ou, Q. Li, H. Xia, Y. Pang, S. Wang, B. Zhao, Y. Song, Y. Zhou, Y. Zheng, Z. Zhang, Z. Zhang, J. Li, H. Dong, J. Zhang, K. M. Kam, J. Chi, S. Huan, D. P. Chin, and Y. Zhao. Diagnostic accuracy of the pure-lamp test for pulmonary tuberculosis at the county-level laboratory in china. *PLoS One*, 5(2):e94544, 2014.

[139] S. Shenai, D. T. Armstrong, E. Valli, D. L. Dolinger, L. Nakiyingi, R. Dietze, M. P. Dalcolmo, M. P. Nicol, W. Zemanay, Y. Manabe, D. J. Hadad, P. Marques-Rodrigues, M. Palaci, R. L. Peres, M. Gaeddert, S. Armakovitch, B. A. Nonyane, C. M. Denkinger, P. Banada, M. L. Joloba, J. Ellner, C. Boehme, D. Alland, and S. E. Dorman. Analytical and clinical evaluation of the epistem genedrive assay for detection of mycobacterium tuberculosis. *J Clin Microbiol*, 54(4):1051–7, 2016.

[140] B. D. Pandey, A. Poudel, T. Yoda, A. Tamaru, N. Oda, Y. Fukushima, B. Lekhak, B. Risal, B. Acharya, B. Sapkota, C. Nakajima, T. Taniguchi, B. Phetsuksiri, and Y. Suzuki. Development of an in-house loop-mediated isothermal amplification (lamp) assay for detection of mycobacterium tuberculosis and evaluation in sputum samples of nepalese patients. *J Med Microbiol*, 57(Pt 4):439–443, 2008.

[141] C. C. Boehme, P. Nabeta, D. Hillemann, M. P. Nicol, S. Shenai, F. Krapp, J. Allen, R. Tahirli, R. Blakemore, R. Rustomjee, A. Milovic, M. Jones, S. M. O'Brien, D. H. Persing, S. Ruesch-Gerdes, E. Gotuzzo, C. Rodrigues, D. Alland, and M. D. Perkins. Rapid molecular detection of tuberculosis and rifampin resistance. *N Engl J Med*, 363(11):1005–15, 2010.

[142] G. Theron, L. Zijenah, D. Chanda, P. Clowes, A. Rachow, M. Lesosky, W. Bara, S. Mungofa, M. Pai, M. Hoelscher, D. Dowdy, A. Pym, P. Mwaba, P. Mason, J. Peter, and K. Dheda. Feasibility, accuracy, and clinical effect of point-of-care xpert mtb/rif testing for tuberculosis in primary-care settings in africa: a multicentre, randomised, controlled trial. *Lancet*, 2014.

[143] Catharina C. Boehme, Pamela Nabeta, Doris Hillemann, Mark P. Nicol, Shubhada Shenai, Fiorella Krapp, Jenny Allen, Rasim Tahirli, Robert Blakemore, Roxana Rustomjee, Ana Milovic, Martin Jones, Sean M. O'Brien, David H. Persing, Sabine Ruesch-Gerdes, Eduardo Gotuzzo, Camilla Rodrigues, David Alland, and Mark D. Perkins. Rapid molecular detection of tuberculosis and rifampin resistance. *New England Journal of Medicine*, 2010.

[144] Anna Engström, Nora Morcillo, Belen Imperiale, Sven E. Hoffner, and Pontus Juréen. Detection of first- and second-line drug resistance in clinical isolates by pyrosequencing. *Journal of Clinical Microbiology*, 50(6):2026–33, 2012.

[145] M. Barnard, H. Albert, G. Coetzee, R. O'Brien, and M. E. Bosman. Rapid molecular screening for multidrug-resistant tuberculosis in a high-volume public health laboratory in south africa. *Am J Respir Crit Care Med*, 177(7):787–92, 2008.

[146] K. R. Jacobson, D. Theron, E. A. Kendall, M. F. Franke, M. Barnard, P. D. van Helden, T. C. Victor, E. M. Streicher, M. B. Murray, and R. M. Warren. Implementation of genotype mtbdrplus reduces time to multidrug-resistant tuberculosis therapy initiation in south africa. *Clin Infect Dis*, 56(4):503–8, 2013.

[147] M. Kipiani, V. Mirtskhulava, N. Tukvadze, M. Magee, H. M. Blumberg, and R. R. Kempker. Significant clinical impact of a rapid molecular diagnostic test (genotype mtbdrplus assay) to detect multidrug-resistant tuberculosis. *Clin Infect Dis*, 59(11):1559–66, 2014.

[148] G. Theron, J. Peter, M. Richardson, M. Barnard, S. Donegan, R. Warren, K. R. Steingart, and K. Dheda. The diagnostic accuracy of the genotype(®) mtbdrsl assay for the detection of resistance to second-line anti-tuberculosis drugs. *Cochrane Database Syst Rev*, (10):Cd010705, 2014.

[149] M. J. Heller, R. A. Robinson, L. J. Burgart, C. J. TenEyck, and W. W. Wilke. Dna extraction by sonication: a comparison of fresh, frozen, and paraffin-embedded tissues extracted for use in polymerase chain reaction assays. *Mod Pathol*, 5(2):203–6, 1992.

[150] QIAGEN. Dneasy blood & tissue kits, 2022.

[151] LifeTechnologies. Dnazol® reagent, 2001.

[152] D. N. Miller, J. E. Bryant, E. L. Madsen, and W. C. Ghiorse. Evaluation and optimization of dna extraction and purification procedures for soil and sediment samples. *Applied and Environmental Microbiology*, 65(11):4715–24, 1999.

[153] Richard de Boer, Remco Peters, Sonja Gierveld, Tim Schuurman, Mirjam Kooistra-Smid, and Paul Savelkoul. Improved detection of microbial dna after bead-beating before dna isolation. *Journal of Microbiological Methods*, 80(2):209–11, 2010.

[154] Spencer. Method of treating foodstuffs (patent), 1950.

[155] The Physics Classroom. Standing waves, 2018.

[156] TESNIT. Tesnit® ba-203, technical data sheet, 2003.

[157] TOPAS Advanced Polymers. Topas® 6017s-04 technical data sheet. *1*, 1(6017S-04), 2019.

[158] N Clark. *Microwave Methods for Additive Layer Manufacturing*. PhD thesis, School of Engineering, 2017.

[159] D. Pozar. *Microwave Engineering*. John Wiley & Sons, 2004.

[160] Invitrogen. *Qubit™ ssDNA Assay Kit*.

[161] Dmitry Malyshev, Catrin F. Williams, Jonathan Lees, Les Baillie, and Adrian Porch. Model of microwave effects on bacterial spores. *Journal of Applied Physics*, 125(12):124701, 2019.

[162] EM. Marlowe, SM. Novak-Weekley, J. Cumpio, SE. Sharp, MA. Momeny, A. Babst, M. Carlson, JS.and Kawamura, and M. Pandori. Evaluation of the cepheid xpert mtb/rif assay for direct detection of mycobacterium tuberculosis complex in respiratory specimens. *Journal of Clinical Microbiology*, 49(4):1621–3, 2011.

[163] Corinne Hofer, Vladimir Zlateski, Philipp Stoessel, Daniela Paunescu, Elia Schneider, Robert Grass, Martin Zeltner, and Wendelin Stark. Stable dispersions of azide functionalized ferromagnetic metal nanoparticles. *Chem. Commun.*, 51(10):1826 – 1829, 2014.

[164] Ariumlab. Magnetic rack, 2023.

[165] ELECTRICAL TECHNOLOGY. Coulomb's laws of magnetic force, 2020.

[166] First4Magnets. How is the strength of a magnet measured? 2023.

[167] L.M. Martinez. Why do different batch volumes require different magnetic fields?, 2013.

[168] SepMag. Sepmag q, for homogeneous and large volume separations, 2023.

[169] First4Magnets. 40mm dia x 20mm thick electromagnet with m5 mounting hole - 25kg pull (24v / 8w), 2023.

[170] Bunting Magnetics. Rectangular electromagnets 12 volt. 2023.